A&A 645, A117 (2021)
https://doi.org/10.1051/0004-6361/202039202

Astronomy & Astrophysics

Pulsating hydrogen-deficient white dwarfs and pre-white dwarfs observed with TESS

I. Asteroseismology of the GW Vir stars RX J2117+3412, HS 2324+3944, NGC 6905, NGC 1501, NGC 2371, and K 1−16

A. H. Córsico[1,2], M. Uzundag[3,4], S. O. Kepler[5], L. G. Althaus[1,2], R. Silvotti[6], A. S. Baran[7,8,9], M. Vučković[3], K. Werner[10], K. J. Bell[11,⋆], and M. Higgins[12]

[1] Grupo de Evolución Estelar y Pulsaciones. Facultad de Ciencias Astronómicas y Geofísicas, Universidad Nacional de La Plata, Paseo del Bosque s/n, 1900 La Plata, Argentina
e-mail: acorsico@fcaglp.unlp.edu.ar
[2] IALP – CONICET, La Plata, Argentina
[3] Instituto de Física y Astronomía, Universidad de Valparaíso, Gran Bretaña 1111, Playa Ancha, Valparaíso 2360102, Chile
[4] European Southern Observatory, Alonso de Cordova 3107, Santiago, Chile
[5] Instituto de Física, Universidade Federal do Rio Grande do Sul, 91501-970 Porto-Alegre, RS, Brazil
[6] INAF-Osservatorio Astrofisico di Torino, strada dell'Osservatorio 20, 10025 Pino Torinese, Italy
[7] Uniwersytet Pedagogiczny, Obserwatorium na Suhorze, ul. Podchorążych 2, 30-084 Kraków, Polska
[8] Embry-Riddle Aeronautical University, Department of Physical Science, Daytona Beach, FL 32114, USA
[9] Department of Physics, Astronomy, and Materials Science, Missouri State University, Springfield, MO 5897, USA
[10] Institute for Astronomy and Astrophysics, Kepler Center for Astro and Particle Physics, Eberhard Karls University, Sand 1, 72076 Tübingen, Germany
[11] DIRAC Institute, Department of Astronomy, University of Washington, Seattle, WA 98195, USA
[12] Department of Physics, Duke University, Durham, NC 27708, USA

Received 18 August 2020 / Accepted 6 November 2020

ABSTRACT

Context. The recent arrival of continuous photometric observations of unprecedented quality from space missions has strongly promoted the study of pulsating stars and caused great interest in the stellar astrophysics community. In the particular case of pulsating white dwarfs, the TESS mission is taking asteroseismology of these compact stars to a higher level, emulating or even surpassing the performance of its predecessor, the *Kepler* mission.
Aims. We present a detailed asteroseismological analysis of six GW Vir stars that includes the observations collected by the TESS mission.
Methods. We processed and analyzed TESS observations of RX J2117+3412 (TIC 117070953), HS 2324+3944 (TIC 352444061), NGC 6905 (TIC 402913811), NGC 1501 (TIC 084306468), NGC 2371 (TIC 446005482), and K 1−16 (TIC 233689607). We carried out a detailed asteroseismological analysis of these stars on the basis of PG 1159 evolutionary models that take into account the complete evolution of the progenitor stars. We constrained the stellar mass of these stars by comparing the observed period spacing with the average of the computed period spacings, and we employed the individual observed periods to search for a representative seismological model when possible.
Results. In total, we extracted 58 periodicities from the TESS light curves of these GW Vir stars using a standard prewhitening procedure to derive the potential pulsation frequencies. All the oscillation frequencies that we found are associated with g-mode pulsations, with periods spanning from ∼817 s to ∼2682 s. We find constant period spacings for all but one star (K 1−16), which allowed us to infer their stellar masses and constrain the harmonic degree ℓ of the modes. Based on rotational frequency splittings, we derive the rotation period of RX J2117+3412, obtaining a value in agreement with previous determinations. We performed period-to-period fit analyses on five of the six analyzed stars. For four stars (RX J2117+3412, HS 2324+3944, NGC 1501, and NGC 2371), we were able to find an asteroseismological model with masses that agree with the stellar mass values inferred from the period spacings and are generally compatible with the spectroscopic masses. Obtaining seismological models allowed us to estimate the seismological distance and compare it with the precise astrometric distance measured with *Gaia*. Finally, we find that the period spectrum of K 1−16 exhibits dramatic changes in frequency and amplitude that together with the scarcity of modes prevented us from meaningful seismological modeling of this star.
Conclusions. The high-quality data collected by the TESS space mission, considered simultaneously with ground-based observations, provide very valuable input to the asteroseismology of GW Vir stars, similar to the case of other classes of pulsating white dwarf stars. The TESS mission, in conjunction with future space missions and upcoming surveys, will make impressive progress in white dwarf asteroseismology.

Key words. asteroseismology – stars: oscillations – stars: interiors – stars: evolution – white dwarfs

⋆ NSF Astronomy and Astrophysics Postdoctoral Fellow.

1. Introduction

Pulsating white dwarfs (WD) and pre-WDs constitute a well-established class of variable stars that exhibit pulsation periods in the range 100−7000 s, associated with low-order ($\ell \leq 3$) nonradial g (gravity) modes. At present, about 350 pulsating WDs are known. They are spread among several subclasses such as ZZ Ceti stars or DAVs (pulsating hydrogen-rich WDs), V777 Her stars or DBVs (pulsating helium-rich WDs), and GW Vir stars or pulsating PG 1159 stars (see the reviews by Winget & Kepler 2008; Fontaine & Brassard 2008; Althaus et al. 2010; Córsico et al. 2019). White dwarf asteroseismology has undergone substantial progress based on ground-based observations, mainly with the time-series photometric observations of the Whole Earth Telescope (WET; Nather et al. 1990), followed by the spectral observations of the Sloan Digital Sky Survey (SDSS, York et al. 2000), and in recent years by the availability of space missions that provide unprecedented high-quality data. The *Kepler* satellite, both the main mission (Borucki et al. 2010) and the K2 mode (Howell et al. 2014), allowed the study of 32 ZZ Ceti stars and two V777 Her stars (Østensen et al. 2011; Hermes et al. 2017a,b; Bell et al. 2017; Bell 2017; Córsico 2020), until the satellite went out of operation in October 2018. The successor of *Kepler* is the Transiting Exoplanet Survey Satellite (TESS, Ricker et al. 2015). TESS has provided extensive photometric observations of the 200 000 brightest stars in 85% of the sky in the first part of the mission. Each observation has a time base of about 27 days per observed sector.

GW Vir stars are pulsating PG 1159 stars, that is, pulsating hot H-deficient, C-, O-, and He-rich pre-WD stars. They include PNNV stars, which are still surrounded by a nebula, and DOV stars, which lack a nebula (Winget et al. 1991). The classification of GW Vir stars also includes the pulsating Wolf-Rayet central stars of planetary nebula (WC) and early-WC (WCE) stars because they share the pulsation properties of pulsating PG 1159 stars (Quirion et al. 2007). GW Vir stars exhibit multiperiodic luminosity variations with periods in the range 300–6000 s, induced by nonradial g-mode pulsations driven by the κ mechanism due to partial ionization of C and O in the outer layers (Starrfield et al. 1983, 1984; Stanghellini et al. 1991; Gautschy et al. 2005; Córsico et al. 2006; Quirion et al. 2007). PG 1159 stars represent the evolutionary connection between post-asymptotic giant branch (AGB) stars and most of the H-deficient WDs, including DO and DB WDs (Werner & Herwig 2006). These stars likely have their origin in a born-again episode induced by a post-AGB He thermal pulse (see Herwig 2001; Blöcker 2001; Althaus et al. 2005; Miller Bertolami et al. 2006, for references).

In this work, we determine the internal structure and evolutionary status of the pulsating pre-WD stars RX J2117.1+3412, HS 2324+3944, NGC 6905, NGC 1501, NGC 2371, and K 1−16 on the basis of the full PG 1159 evolutionary models of Althaus et al. (2005) and Miller Bertolami & Althaus (2006). These models were derived from the complete evolution of progenitor stars through the thermally pulsing AGB phase and born-again episode. We compute adiabatic g-mode pulsation periods on PG 1159 evolutionary models with stellar masses ranging from 0.530 to 0.741 $M_{\odot}$.

The paper is organized as follows. In Sect. 2 we provide an account of the main characteristics of the studied GW Vir stars. Sect. 3 is focused on describing the methods we apply to obtain the pulsation periods of each target star. Section 4 is devoted to search for a constant period spacing in the list of periods of each star by applying three significance tests. A brief summary of the stellar models of PG 1159 stars employed for the asteroseismological analysis of these stars is provided in Sect. 5. In Sect. 6 we derive the spectroscopic masses of the target stars on the basis of their published values of $T_{\rm eff}$ and $\log g$. In Sect. 7 we carry out a detailed asteroseismological analysis for each star by assessing the stellar mass of each object through the use of the period spacing when possible, and by performing period-to-period fits with the aim of finding an asteroseismological model for each pulsating PG 1159 star. Finally, in Sect. 8 we summarize our main results and make some concluding remarks.

2. Targets

Unlike the *Kepler* space telescope, which was characterized by a restricted sky coverage, the TESS mission is providing unprecedented photometric observations of GW Vir stars through its expansive sky coverage. In this work, we report on new TESS observations of the already known pulsating pre-WD stars RX J2117.1+3412, HS 2324+3944, NGC 6905, NGC 1501, NGC 2371, and K 1−16. We note that NGC 6905 and NGC 1501 are not formally spectroscopic PG 1159 stars but WCE stars, and NGC 2371 is classified as a WC-PG 1159 transition object. The essential difference between the PG 1159, WC and WCE spectroscopic classes is the presence of much stronger winds and mass losses in the WC and WCE objects, leading to emission line spectra (Werner & Herwig 2006). Following Quirion et al. (2007), we include the stars NGC 6905, NGC 1501, and NGC 2371 in the category of GW Vir variable stars. The location of the six stars in the $\log T_{\rm eff}$ versus $\log g$ diagram is displayed in Fig. 1. According to the surface gravity of each star and the evolutionary tracks of Miller Bertolami & Althaus (2006), all the stars we analyze are evolving at stages prior to their maximum possible temperatures before they enter the cooling branch of WDs. It is therefore expected that all these stars are heating and contracting, with the consequent secular shortening of the pulsation periods of their g modes (see Sect. 7). We describe the basic characteristics of these stars below and summarize their stellar properties in Table 1.

RX J2117.1+3412 (hereafter RX J2117 and TIC 117070953) is a PNNV star characterized by an effective temperature of $T_{\rm eff} = 170\,000 \pm 10\,000$ K, a surface gravity of $\log g = 6.00 \pm 0.3$, and a surface composition of $(X_{\rm He}, X_{\rm C}, X_{\rm O}) = (0.39, 0.55, 0.06)$ (Werner & Herwig 2006). This is one of the PG 1159 stars in which iron has been detected (Werner et al. 2010). At this effective temperature, the star is the hottest known GW Vir star. The location of this star in the $\log T_{\rm eff} - \log g$ diagram is displayed in Fig. 1. The *Gaia* DR2 parallax and corresponding distance for this star are $\pi = 1.991 \pm 0.050$ mas and $d = 502 \pm 12$ pc. The variability of this star was independently discovered by Watson & Werner (1992) and Vauclair et al. (1993). Vauclair et al. (2002) analyzed the star in depth and published many results from a multisite photometric campaign with the WET (Nather et al. 1990). A search for p (pressure) modes in this star was carried out by Chang et al. (2013), with negative results. RX J2117 has been the focus of detailed asteroseismological modeling by Córsico et al. (2007a), yielding a variety of constraints; among them, a value of the asteroseismic stellar mass that is considerably lower than suggested by spectroscopy coupled to evolutionary tracks.

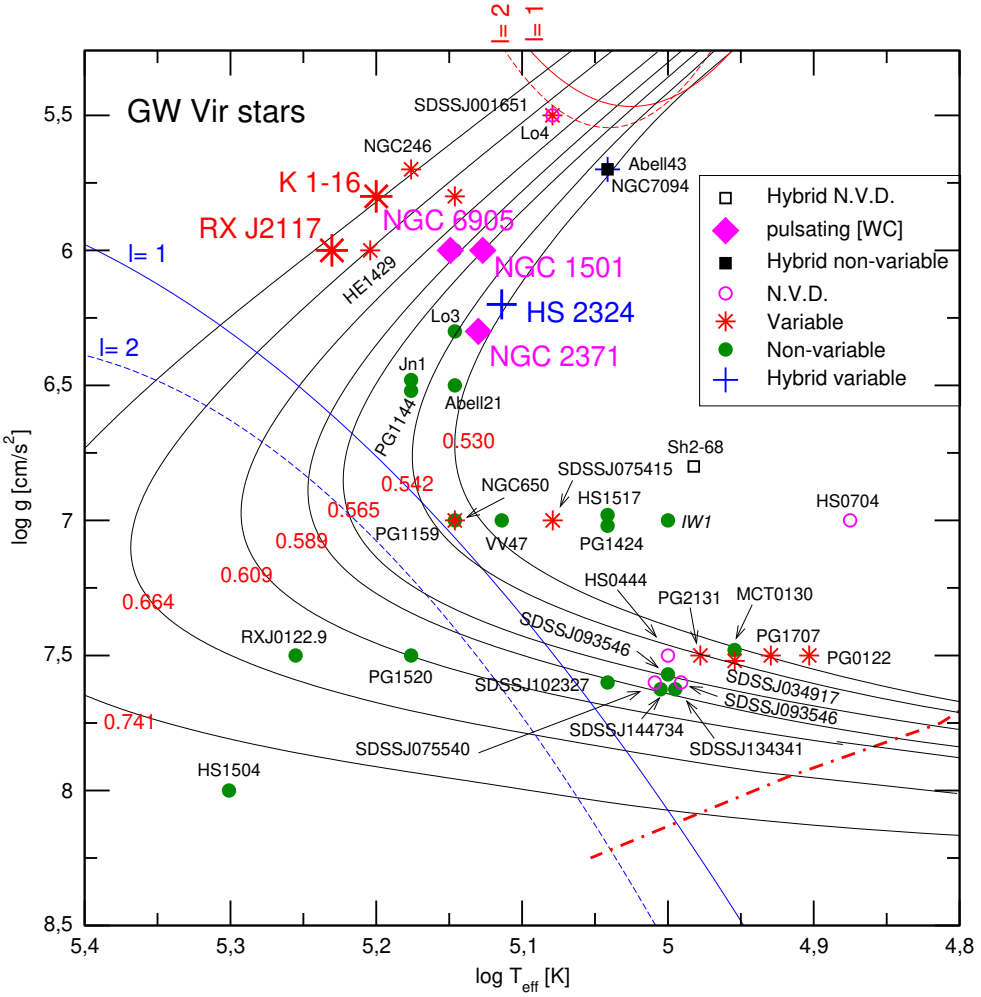

Fig. 1. Location of the spectroscopically calibrated variable and nonvariable PG 1159 stars and variable [WCE] stars in the $\log T_{\rm eff}$ – $\log g$ plane. PG 1159 stars with no variability data (N. V. D.) are depicted with hollow circles. Thin solid curves show the evolutionary tracks from Miller Bertolami & Althaus (2006) for stellar masses 0.530, 0.542, 0.565, 0.589, 0.609, 0.664, and 0.741 $M_{\odot}$. Parameterizations of the theoretical pulsational dipole (solid curves) and quadrupole (dashed curves) red and blue edges of the instability domain according to Córsico et al. (2006) are also displayed. The location of the GW Vir stars RX J2117 (red star), K 1−16 (red star), HS 2324 (blue plus), NGC 6905, NGC 1501, and NGC 2371 (magenta diamonds) are emphasized with large symbols.

Table 1. Six pulsating pre-WD stars.

TIC	Name	$T_{\rm eff}$ [K]	$\log g$ [cgs]	GW Vir class	Spectral type	π [mas]	d [pc]
117070953	RX J2117.1+3412	170 000 ± 10 000	6.00 ± 0.03	PNNV	PG 1159	1.991 ± 0.050	502 ± 12
352444061	HS 2324+3944	130 000 ± 10 000	6.20 ± 0.20	DOV	PG 1159 (hybrid)	0.691 ± 0.050	1448 ± 105
402913811	NGC 6905	141 000 ± 10 000	6.00 ± 0.20	PNNV	[WCE]	0.612 ± 0.059	1634 ± 158
084306468	NGC 1501/[WO4]	134 000 ± 10 000	6.00 ± 0.20	PNNV	[WCE]	0.567 ± 0.025	1763 ± 79
446005482	NGC 2371	135 000 ± 10 000	6.30 ± 0.20	PNNV	[WC]-PG 1159	0.532 ± 0.066	1879 ± 232
233689607	K 1−16	160 000 ± 16 000	5.80 ± 0.30	PNNV	PG 1159	0.466 ± 0.053	2146 ± 244

Notes. Columns 1–8 correspond to the TESS input catalog number, name of the object, effective temperature, surface gravity, GW Vir class, spectral classification, parallax, and distance, respectively. For details, see the text.

HS 2324+3944 (hereafter HS 2324 and TIC 352444061) is one out of four peculiar members of the PG 1159 spectral class that exhibit H at the surface, called "hybrid PG 1159 stars" (Napiwotzki & Schoenberner 1991). The star exhibits a surface chemical composition of $(X_{\rm H}, X_{\rm He}, X_{\rm C}, X_{\rm O}) = (0.17, 0.35, 0.42, 0.06)$ (Werner & Herwig 2006). This object is characterized by an effective temperature $T_{\rm eff} = 130\,000 \pm 10\,000$ K and a surface gravity $\log g = 6.2 \pm 0.2$ (see Fig. 1). The *Gaia* DR2 parallax and corresponding distance for this star are $\pi = 0.691 \pm 0.0502$ mas and $d = 1448 \pm 105$ pc. HS 2324 was discovered to be pulsating by Silvotti (1996) (see also Handler et al. 1997a), and it was the target of a multisite photometric campaign carried out by Silvotti et al. (1999). This object has not been the subject of published asteroseismological modeling.

NGC 6905 (also TIC 402913811) is a [WCE]-type star discovered by Ciardullo & Bond (1996), characterized by $T_{\rm eff} = 141\,000$ K and $\log g = 6$ (see Fig. 1), and pulsation periods in the range 710−912 s. Ciardullo & Bond (1996) found that while the principal pulsation modes lie within a fairly restricted frequency range, the individual modes that are actually observed completely change on a timescale of a few months (or less). The surface chemical composition of NGC 6905 is $(X_{\rm He}, X_{\rm C}, X_{\rm O}) = (0.60, 0.25, 0.15)$ (Koesterke 2001). The *Gaia* DR2 parallax and corresponding distance for this object are

$\pi = 0.612 \pm 0.059$ mas and $d = 1634 \pm 158$ pc. This star has not been asteroseismologically modeled before.

NGC 1501 (also TIC 084306468) is classified as a [WCE]-type star. The effective temperature and gravity of this star are $T_{\rm eff} = 134\,000$ K and $\log g = 6.0$ (Fig. 1), and its surface chemical composition is $(X_{\rm He}, X_{\rm C}, X_{\rm O}) = (0.50, 0.35, 0.15)$ (Koesterke & Hamann 1997; Werner & Herwig 2006). The parallax and corresponding distance for this star extracted from *Gaia* DR2 are $\pi = 0.567 \pm 0.025$ mas and $d = 1763 \pm 79$ pc. The variability of NGC 1501 was detected by Ciardullo & Bond (1996), who measured ten periodicities ranging from 5200 s down to 1154 s, with the largest-amplitude pulsations occurring between 1154 s and 2000 s. As for NGC 6905, in the case of NGC 1501 the observed pulsation spectrum varies on timescales of months according to Ciardullo & Bond (1996). Based on period-spacing data, Bond et al. (1996) inferred a stellar mass of $0.53 \pm 0.03\,M_{\odot}$ for NGC 1501. The star was a target of a detailed asteroseismological analysis by Córsico et al. (2009a), who derived a stellar mass of $\sim$0.57 $M_{\odot}$ based on the period-spacing data. However, they were unable to find an unambiguous best-fit model with a period-fit procedure.

NGC 2371 (also TIC 446005482) is a GW Vir variable classified as a [WC]-PG 1159 transition object. It was discovered to be pulsating by Ciardullo & Bond (1996). The star shows periodicities in the range 923 − 1825 s and has atmospheric parameters $T_{\rm eff} = 135\,000$ K and $\log g = 6.3$ (see Fig. 1), and $(X_{\rm He}, X_{\rm C}, X_{\rm O}) = (0.54, 0.37, 0.08)$ (Herald & Bianchi 2004). Like NGC 6905 and NGC 1501, NGC 2371 exhibits variations of the characteristics of the frequency spectrum on timescales of months or shorter (Ciardullo & Bond 1996). From *Gaia* DR2, we know that the parallax and distance of this object are $\pi = 0.532 \pm 0.066$ mas and $d = 1879 \pm 232$ pc, respectively. This star has not been the focus of any detailed asteroseismological analysis.

K 1−16 (also Kohoutek 1−16 and TIC 233689607) is a PNNV star characterized by an effective temperature of $T_{\rm eff} = 140\,000 \pm 10\,000$ K, a surface gravity of $\log g = 6.40 \pm 0.3$, and a surface composition of $(X_{\rm He}, X_{\rm C}, X_{\rm O}) = (0.33, 0.50, 0.17)$ (Werner & Herwig 2006). Werner et al. (2007, 2010) discovered high-ionization lines of neon (Ne VIII) and iron (Fe X) in K 1−16, and redetermined its effective temperature and gravity as $T_{\rm eff} = 160\,000 \pm 16\,000$ K and $\log g = 5.8 \pm 0.3$ (see Fig. 1). The chemical composition was also redetermined: $(X_{\rm He}, X_{\rm C}, X_{\rm O}) = (0.58, 0.34, 0.06)$ (Werner et al. 2010). K 1−16 was the first PNNV star to be discovered (Grauer & Bond 1984). Grauer & Bond (1984) detected periodicities with a dominant period of ∼1700 s and a semi-amplitude of about 0.01 mag. These authors found that several additional periods sometimes appear in power spectra derived from light curves, and on two occasions a rapid drop into or emergence from a state in which no detectable variations were present. Feibelman et al. (1995) claimed spectral variability and speculated about a connection of this phenomenon to the changes in the pulsating nature of this star. From *Gaia* DR2, the parallax and distance of K 1−16 are $\pi = 0.466 \pm 0.053$ mas and $d = 2146 \pm 244$ pc, respectively. The asteroseismological potential of this interesting object has not been thoroughly studied so far.

3. Observations and data reduction

The primary mission of TESS is to search for exoplanets around bright target stars. The spacecraft was launched successfully on 18 April 2018 (Ricker et al. 2014). The mission-data products of TESS also allow us to study stellar variability, including pulsations. Through nearly continuous stable photometry, as well as its expansive sky coverage, TESS has made a significant contribution to the study of stellar pulsations in evolved compact objects (Bell et al. 2019; Wang et al. 2020; Althaus et al. 2020; Bognár et al. 2020).

We study six known pulsating pre-WD stars by investigating their pulsational characteristics with the high-precision photometry of TESS (see Table 2). The transformations between the photometric systems from the visual magnitude ($V_{\rm mag}$) to TESS $T_{\rm mag}$ magnitudes were calculated using the publicly available code `ticgen`[1]. The stars were observed in the two-minute short-cadence mode of TESS, corresponding to a Nyquist frequency of 4200 μHz. We downloaded the light curves from The Mikulski Archive for Space Telescopes, which is hosted by the Space Telescope Science Institute (STScI)[2] in FITS format. The data contained in the FITS files were processed based on the Pre-Search Data Conditioning pipeline (Jenkins et al. 2016). We extracted times and fluxes (PDCSAP FLUX) from the FITS files. The times are given in barycentric corrected dynamical Julian days (BJD − 2457000, corrected for leap seconds, see Eastman et al. 2010). The fluxes were converted into fractional variations from the mean, that is, differential intensity $\Delta I/I$, and transformed into amplitudes in parts-per-thousand (ppt). The ppt unit corresponds to the milli-modulation amplitude (mma) unit[3] used in the past. We sigma-clipped the data at 5σ to remove the outliers that appear above five times the median of intensities, that is, that depart from the (local) mean by 5σ.

The final light curves of the target stars are shown in Fig. 2. After detrending the light curves, we calculated their Fourier transforms (FTs) and examined them for pulsations and binary signatures. For pre-whitening, we employed our customized tool, in which, using a nonlinear least-squares (NLLS) method, we simultaneously fit each pulsation frequency in a waveform $A_i \sin(\omega_i t + \phi_i)$, with $\omega = 2\pi/P$, and P the period. This iterative process was run starting with the highest peak until no peak appeared above the 0.1% false-alarm probability (FAP) significance threshold. We analyzed the concatenated light curve from different sectors, if observed. The FAP was calculated by randomizing the timings, that is, shuffling the observations one thousand times and recalculating the FTs. We calculated the amplitude at which there was a 0.1%= 1/1000 probability of any peak being due to noise (e.g., Kepler 1993).

Before describing the observations of each individual target star, we emphasize that most pulsating WDs and pre-WDs, including GW Vir stars, show amplitude and frequency variations. A similar phenomenon is observed in pulsating sdB stars. An example of this phenomenon is documented here for K 1−16 (see Sect. 3.6 below). In general terms, some modulations might probably be due to simple photon-count noise caused by contamination of the background light in the aperture. Other modulations could come from the rotation-to-pulsation energy interchange: the amplitude of the components of the multiplets change with time, as was detected over the years. In the case of GW Vir stars, however, considering that the theoretical e-folding times are much longer than the observations, we do not expect real mode energy interchanges as they are observed for the DBV star GD 358 (e.g., Provencal et al. 2009).

[1] https://github.com/tessgi/ticgen
[2] http://archive.stsci.edu/
[3] 1 mma = 1/1.086 mmag = 0.1% = 1 ppt; see, e.g., Bognar & Sodor (2016).

Table 2. Six GW Vir stars reported from TESS observations, including the name of the targets, TESS magnitude, observed sectors, date, CROWDSAP keyword, and length of the runs (Cols. 1–6, respectively).

Name	$T_{\rm mag}$	Obs. sector	Start time (BJD-2 457 000)	CROWDSAP	Length [d]	Resolution μHz	Average noise level [ppt]	0.1% FAP [ppt]
RX J2117.1+3412	11.73	15	1711.3688	0.519	22.76	0.76	0.26	1.18
HS 2324+3944	14.81	16–17	1738.6566	0.571	49.14	0.35	0.44	2.07
NGC 6905	13.90	14	1683.3582	0.087	26.85	0.43	0.73	3.35
NGC 1501/[WO4]	12.40	19	1816.0888	0.556	25.06	0.46	0.11	0.53
NGC 2371	12.90	20	1842.5093	0.356	26.31	0.44	0.20	0.90
K 1−16	14.36	14–17 19–20 22–26	1683.3542	0.570	298.93	0.038	0.21	0.86

Notes. From the Fourier transform of the original and shuffled data, three different set of parameters (resolution, average noise level of amplitude spectra, and detection threshold, which we define as the amplitude at 0.1% FAP) are presented in Cols. 7–9, respectively. The CROWDSAP keyword shows the ratio of target flux to total flux in the optimal TESS light-curve aperture.

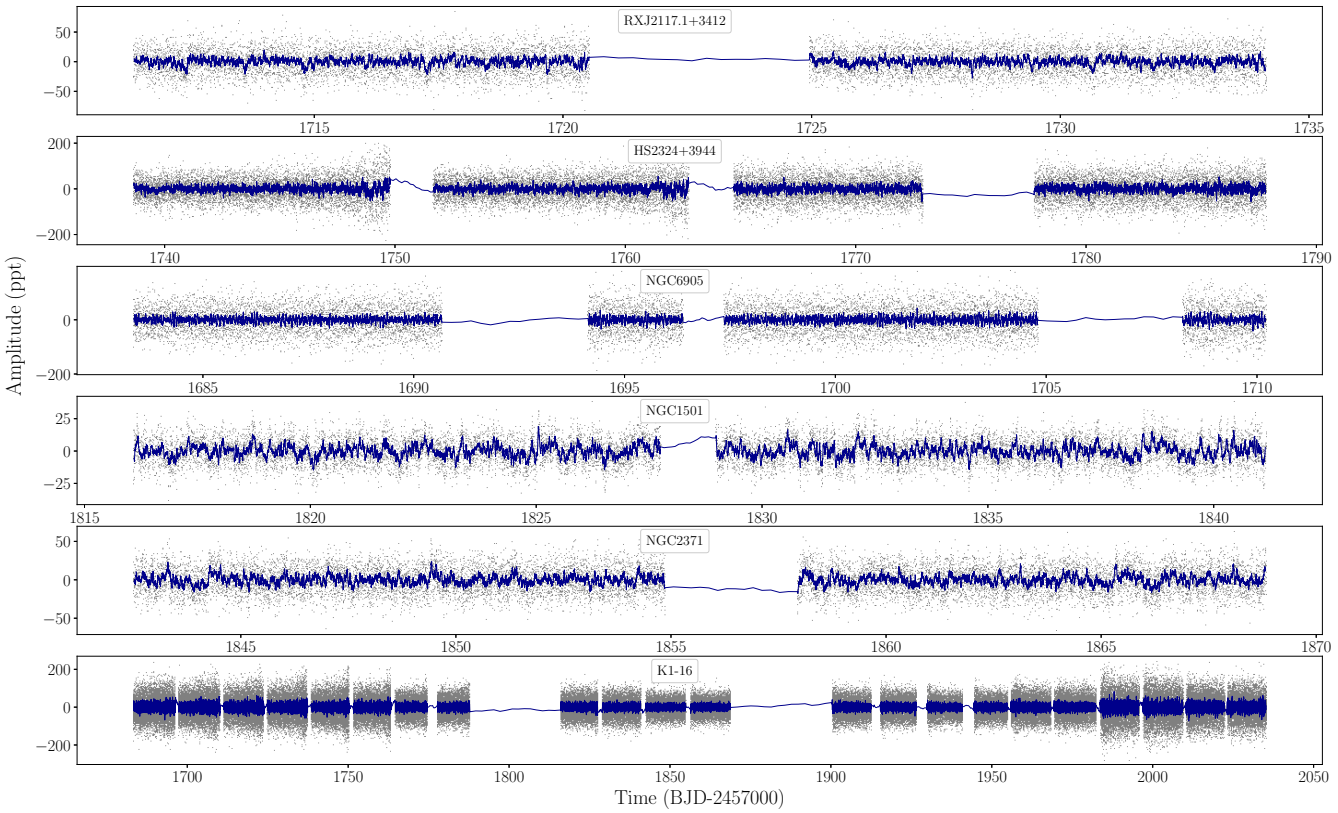

Fig. 2. Reduced TESS light curves of the pulsating pre-WD stars. The black dots are the TESS data sampled every two minutes. The blue lines are binned light curves that are calculated by a running mean every 20 points (corresponding to 38 minutes). K 1−16 was observed in eleven sectors (14, 15, 16, 17, 19, 20, 22, 23, 24, 25 and 26), HS 2324 was observed in two consecutive sectors (16 and 17), and the other stars were observed in a single sector each.

3.1. RX J2117

RX J2117 (TIC 117070953, $T_{\rm mag}$ = 11.73, $m_{\rm V}$ = 12.33) was observed by TESS in Sector 15 between 2019 August 15 and 2019 September 11. The temporal resolution is $1.5/T$ = 0.76 μHz (T is the data span of 22.8 days). The average noise level of the amplitude spectra is 0.29 ppt. The upper panel of Fig. 2 depicts the light curve, and the upper panel of Fig. 3 shows the FT corresponding to RX J2117. In Table 3 we show the list of periods of RX J2117 detected with TESS. The period at 1038 s corresponds to a peak with a signal-to-noise ratio (S/N) lower than 4. However, we included it because it corresponds to the central component of a triplet and has been observed in ground-based data (Vauclair et al. 2002).

The frequencies emphasized with boldface in Table 3 can be interpreted as components of rotational triplets (ℓ = 1), with an average frequency separation of $\delta\nu \sim 5.57\,\mu$Hz. This frequency separation agrees with the value found by Vauclair et al. (2002). The rotational multiplets are depicted in Fig. 4. We briefly describe the rotation effect on the pulsation frequencies of a star. In the presence of stellar rotation, nonradial modes of degree ℓ split into $2\ell + 1$ components that differ in azimuthal

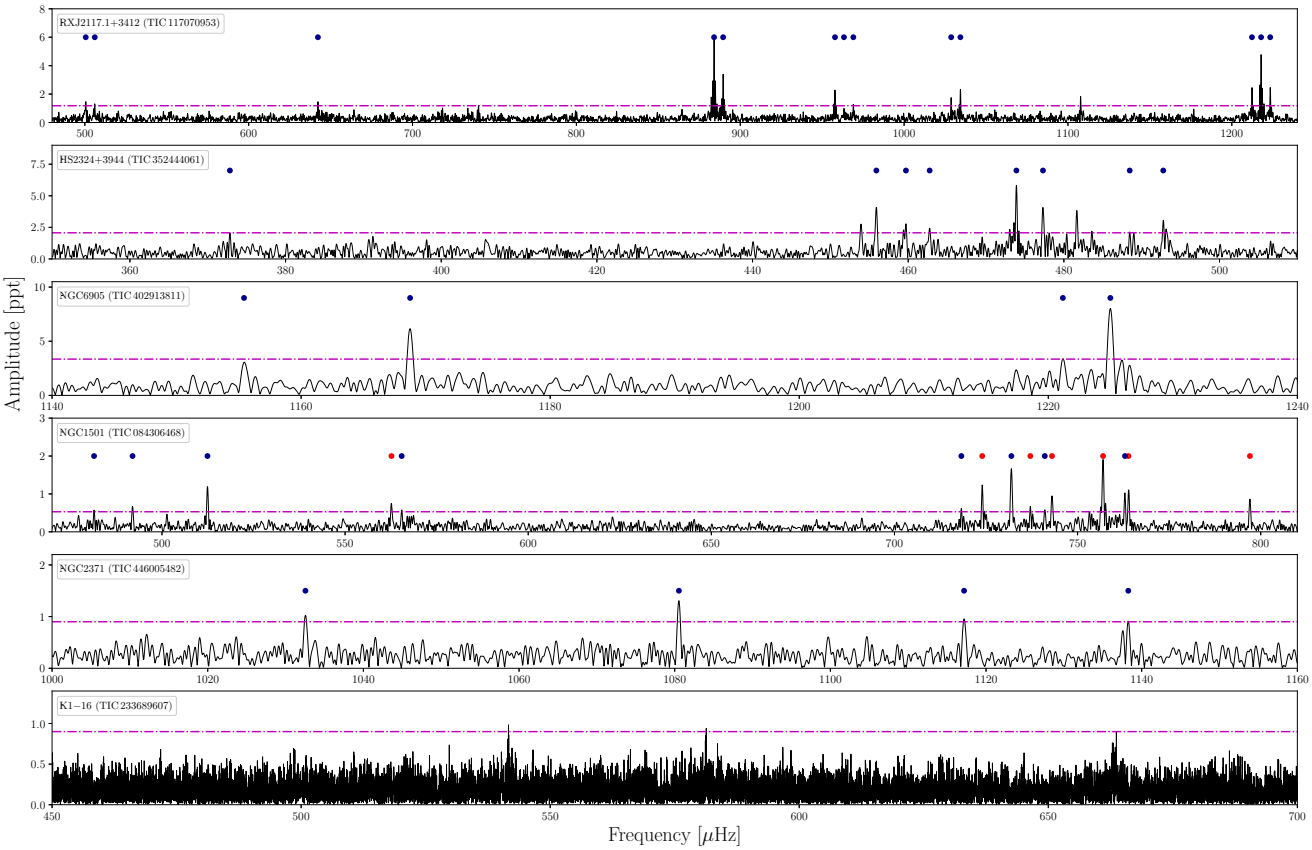

Fig. 3. Fourier transforms of the GW Vir stars, showing identified dipole ($\ell = 1$, blue dots) and quadrupole ($\ell = 2$, red dots) modes. The horizontal dashed magenta line shows the detection threshold, which is defined as 0.1% FAP.

Table 3. Independent frequencies, periods, and amplitudes, their uncertainties, and the S/N in the data of RX J2117.

Peak	ν (μHz)	Π (s)	A (ppt)	S/N
f_1	**500.559(39)**	1997.760(16)	1.45(23)	5.5
f_2	**506.057(43)**	1976.060(17)	1.33(23)	5.1
f_3	642.255(40)	1557.010(10)	1.44(23)	5.5
f_4	740.266(49)	1350.870(9)	1.17(23)	4.5
f_5	**884.017(9)**	1131.200(12)	6.15(23)	23.6
f_6	**889.556(17)**	1124.156(21)	3.37(23)	12.9
f_7	**957.817(25)**	1044.041(27)	2.30(23)	8.8
f_8	**963.28(6)**	1038.120(6)	1.03(23)	3.9
f_9	**969.013(44)**	1031.978(47)	1.29(23)	4.9
f_{10}	**1028.729(33)**	972.073(31)	1.72(23)	6.6
f_{11}	**1034.356(25)**	966.785(23)	2.31(23)	8.8
f_{12}	1107.713(31)	902.761(25)	1.84(23)	7.0
f_{13}	**1212.297(23)**	824.880(16)	2.48(23)	9.5
f_{14}	**1217.872(12)**	821.105(8)	4.78(23)	18.3
f_{15}	**1223.429(24)**	817.375(16)	2.41(23)	9.2

Notes. Frequencies in boldface correspond to components of rotational triplets (see Fig. 4). Errors are given in parenthesis to two significant digits.

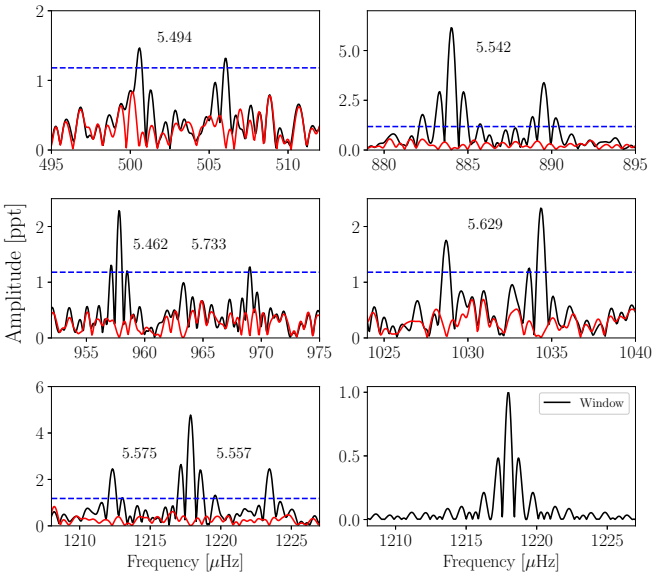

Fig. 4. Amplitude spectra of RX J2117 showing rotational multiplets. The panels present rotational splittings in different regions in the amplitude spectra with an average splitting $\delta\nu = 5.570\,\mu$Hz. The *last panel* (bottom right) presents the window function of RX J2117 for the frequency $1217.872\,\mu$Hz. The horizontal dashed blue line shows the confidence level of 0.1% FAP. The red lines are residuals after extraction of the signals.

(m) number. In the case of slow and solid rotation, the frequency splitting can be obtained as $\delta\nu_{\ell,k,m} = m(1 - C_{\ell,k})\Omega_{\rm R}$, $\Omega_{\rm R}$ being the angular rotational frequency of the pulsating star, and $m = 0, \pm1, \pm2, \cdots, \pm\ell$. The condition of slow rotation translates into $\Omega_{\rm R} \ll \nu_{\ell,k}$. The coefficients $C_{\ell,k}$, called Ledoux coefficients (Ledoux & Walraven 1958), adopt a simple form in the asymptotic limit of high radial-order g modes ($k \gg \ell$):

Table 4. Independent frequencies, periods, and amplitudes (and their uncertainties) and the S/N in the data of HS 2324.

Peak	ν (μHz)	Π (s)	A (ppt)	S/N
f_1	372.849(23)	2682.05(17)	2.04(38)	4.6
f_2	453.928(19)	2202.99(9)	2.52(38)	5.7
f_3	455.909(12)	2193.42(6)	4.00(38)	9.0
f_4	459.709(16)	2175.29(8)	2.96(38)	6.7
f_5	462.755(19)	2160.97(9)	2.50(38)	5.6
f_6	473.900(8)	2110.152(35)	6.01(38)	13.6
f_7	477.316(11)	2095.046(49)	4.26(38)	9.6
f_8	481.670(13)	2076.11(5)	3.73(38)	8.4
f_9	488.458(22) (*)	2047.26(9)	2.10(38)	4.7
f_{10}	492.769(16)	2029.35(7)	3.12(39)	7.0
f_{11}	493.215(22)	2027.52(9)	2.32(39)	5.2
f_{12}	952.492(22)	1049.877(24)	2.16(38)	4.9

Notes. (*)Alternatively, it could be 488.984 μHz. The two close peaks have similar amplitude, and when one of the two is selected, the other decreases below the detection threshold.

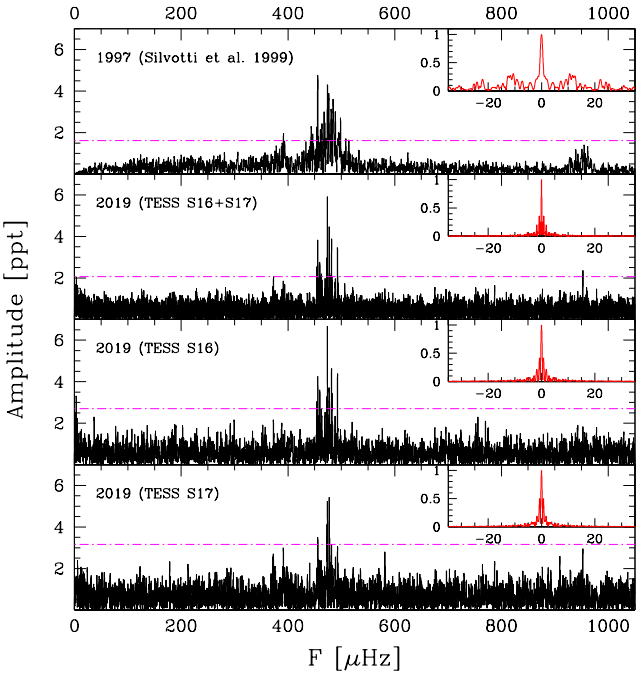

Fig. 5. Comparison between the amplitude spectrum of HS 2324 in 1997 (Silvotti et al. 1999) and 2019 (TESS data). The detection threshold (dash-dotted magenta line) in 2019 is slightly higher (2.07 ppt with sector 16 and 17 together vs. 1.62 ppt in 1997), but the spectral window (red, *upper right panels*) is much cleaner. This partially explains the higher density of the peaks in 1997. The low level of noise below ~100 μHz in 1997 is due to artificial filtering.

$C_{\ell,k} \sim [\ell(\ell+1)]^{-1}$. For dipole ($\ell = 1$) and quadrupole ($\ell = 2$) modes, we have $C_{1,k} \sim 0.5$ and $C_{2,k} \sim 0.17$, respectively. Multiplets in the frequency spectrum of a pulsating WD can be very useful to identify the harmonic degree of the pulsations. This inference of the rotation period has been successfully applied to several pulsating WD stars (see Hermes et al. 2017a, for the case of ZZ Ceti stars observed during the *Kepler* and K2 missions). Because the multiplets exhibited by the star are triplets (two complete triplets and three triplets with one undetected component each), this means in the case of RX J2117 that $\ell = 1$, and therefore $C_{\ell,k} \sim 0.5$. We assume that the central peak of the multiplets ($m = 0$ components) are 1997.75, 1124.15, 1038.12, 972.07, and 889.557 μHz. Therefore we can obtain an estimate of the rotational period of RX J2117 of $P_{\rm rot} = 1/\Omega_{\rm R} \sim 1.04$ days.

An interesting feature of the FT of RX J2117 is a series of at least seven low-frequency harmonics of a 9.509 ± 0.004 μHz signal. These are suggestive of variability from a photometric binary with an orbital period of 1.2172 ± 0.0005 days. Extracting and analyzing light curves from every individual pixel in the TESS target pixel file for TIC 117070953 reveals a clear binary eclipse signature. This is strongest outside the aperture used by the TESS pipeline to extract the light curve for RX J2117, but near enough to contribute some light to the aperture. We conclude that the eclipses do not originate in the PNNV target. A public software tool to aid the identification of contaminating variable stars in the large 21″ TESS pixels is under development (Higgins & Bell, in prep.).

3.2. HS 2324

HS 2324 (TIC 352444061, $T_{\rm mag} = 14.81$, $m_{\rm V} = 15.41$) was observed for 49.15 days in Sectors 16 and 17 with a duty cycle of 91.02%. The light curve is shown in Fig. 2. In Fig. 3 we show the FT. In Table 4 we list the periods above 0.1% FAP level of 2.07 ppt (corresponding to an S/N of 3.23) detected in the TESS light curve. While 11 frequencies populate a small region of the power spectrum between ~450 μHz and ~500 μHz, one frequency is located in the low-frequency region (~372.8 μHz), and a peak is found in the high-frequency region (~952.5 μHz). The signal with 952.5 μHz is close to twice the main frequency group, and thus we cannot exclude that it is a linear combination of the main peaks. However, it does not exactly correspond to any combination, the closest combination being at 951.2 (=473.9 + 477.3) μHz. A direct comparison between the amplitude spectrum in 1997 (Silvotti et al. 1999) and the TESS amplitude spectrum of 2019 is shown in Fig. 5.

Silvotti et al. (1999) suggested a possible rotation period of ~2.3 days for HS 2324 based on a frequency resolution of 1.4 μHz. They also proposed that the detected peaks are part of dipole and quadrupole asymptotic sequences, elaborating on period spacings of 18.8 s and 10.4 s for $\ell = 1$ and $\ell = 2$, respectively. Here, we find that all the periodicities detected in TESS data can be associated with dipole sequences (see Fig. 3 and Sect. 4.2). With a frequency resolution of 0.35 μHz, we find no clear indications of rotational multiplets, suggesting that the star may have a rotation period longer than ~49 days (the duration of the run) and/or that the star is seen pole-on, or also that the modes with $m = \pm 1$ are not excited during the observations (see, e.g., Baran et al. 2015; Winget et al. 1991).

Notwithstanding the above, we also examined the possibility that the two frequency pairs at (481.67−477.316) μHz and (492.769−488.458) μHz are two ($\ell = 1$) incomplete rotational triplets with frequency separations of 4.354 μHz and 4.310 μHz, respectively. A rotational splitting of ~4.3 μHz cannot be totally excluded, and it is very close to the ~4.2 μHz splitting found by Silvotti et al. (1999). If these two frequency pairs were part of two rotational triplets, then only one component of each pair should be used in the assessment of the dipole period spacing in Sect. 4.2. As we show in that section, the assessment of the period-spacing of HS 2324 remains almost unaltered even when we remove two frequencies from the analysis.

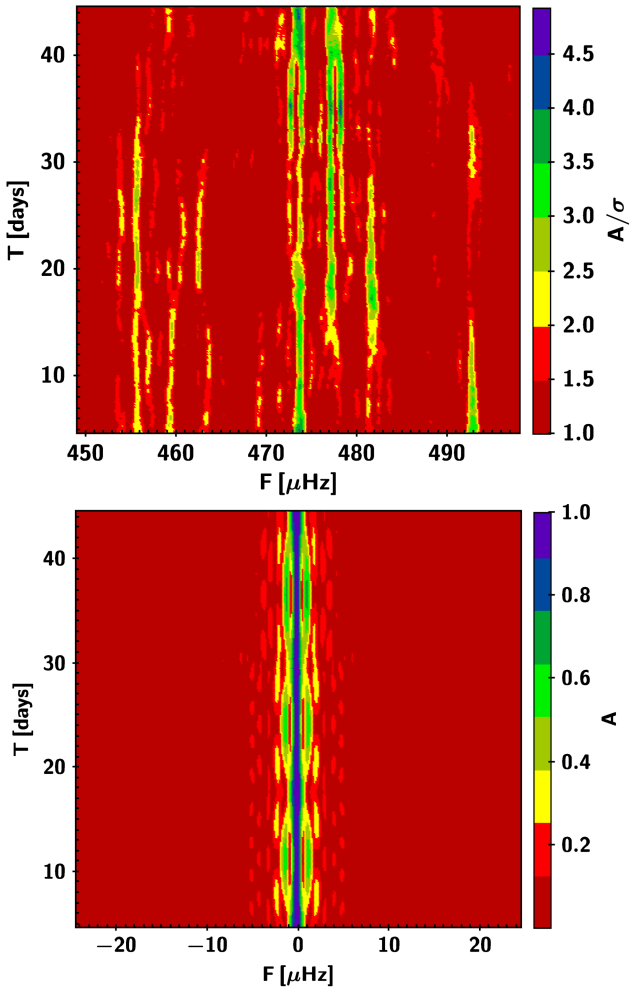

Fig. 6. *Top*: sliding FT (sFT) of HS 2324 in the region between 449 and 498 μHz. The color-coded amplitude is given in σ units, i.e., amplitude divided by the mean noise of each FT. Because each FT is computed in a short subrun of 9.3 days, the FT mean noise is high and the color-coded S/N appears much lower than in Table 4. *Bottom*: sliding WF (sWF) obtained using a single sinusoid of constant frequency and constant amplitude of one, without any noise. The frequency scale is the same in both panels. See text for more details on sFT and sWF computations.

In Fig. 6 we show the sliding FT (sFT) of HS 2324 in the main region of the spectrum (top panel), which can be compared with the sliding window function (sWF, bottom panel). Most frequencies are relatively stable, with some variations in amplitude. This figure clearly excludes the damping oscillator hypothesis that was considered by Silvotti et al. (1999). Some additional details on sFT and sWF computations are given at the end of Sect. 3.6. For HS 2324, each data subset includes 6715 data points (corresponding to ~9.3 days for continuous data), and the step between one subset and the next corresponds to 51 data points (0.07 days for continuous data). To continue, a photometric monitoring of this star would be useful in order to detect new pulsation frequencies, verify the presence of rotational multiplets, and confirm the identification of some $\ell = 2$ pulsation modes (see Sect. 7.2 and Table 16).

3.3. NGC 6905

NGC 6905 (TIC 402913811, $T_{\rm mag} = 13.90$, $G = 14.5545 \pm 0.0027$) was observed for 26.85 days in Sector 14. TESS observations of NGC 6905 started on 18 July 2019 and lasted until 15 August 2019. These observations yield 13 615 data points after the outliers were removed. The final light curve after detrending is shown in Fig. 2. NGC 6905 is a good illustration of cross contamination in TESS photometry. Each TESS pixel comprises 21 arcsec. The planetary nebula of NGC 6905 extends to 32 arcsec, and an additional target (*Gaia* magnitude of 14.5) lies a mere 10 arcsec away from NGC 6905. This contamination is reflectedf as additional noise in the FT of NGC 6905. The star has the highest average noise level (0.73 ppt) in our sample. All the oscillation amplitudes that are extracted from the light curve are reduced due to this contamination from the nearby stars and nebula. The FT of NGC 6905 showed a few signals within an S/N of 4.6. We calculated the threshold at 0.1% FAP as 3.35 ppt, corresponding to an S/N of 4.6. The average noise level for NGC6905 is 0.73 ppt. The peaks that are extracted from the light curve appear at 4.14, 8.14, 4.67, and 10.68σ (σ is the median of noise level of amplitude). We included the peak of 1155.415 μHz as a possible oscillation. Additionally, we extracted three more periodicities from the light curve. These three frequencies, 1168.752, 1221.170, and 1224.984 μHz, are robust detections with S/Ns of 8.4, 4.8, and 11.1, respectively. After we extracted these three peaks from the light curve, we calculated the average noise level of amplitude spectra and defined the new detection threshold. The average noise level of the FT excluding these three modes remained almost the same as 0.73 ppt (the difference is negligible with 0.001 ppt). The 0.1% FAP was also not affected drastically and is 3.34 ppt (including all the peaks 0.1% FAP = 3.35). When we consider the detection threshold 4σ of 3 ppt, then 1155.415 μHz (f_1) can conveniently be evaluated as the true pulsational peak. These four extracted peaks are shown in Fig. 3 and are listed in Table 5.

Table 5. Independent frequencies, periods, and amplitudes (and their uncertainties) and the S/N in the data of NGC 6905.

Peak	ν (μHz)	Π (s)	A (ppt)	S/N
f_1	1155.415(43)	865.490(32)	3.1(6)	4.2
f_2	1168.752(22)	855.613(16)	6.1(6)	8.4
f_3	1221.170(38)	818.887(26)	3.5(6)	4.8
f_4	1224.984(17)	816.337(11)	8.0(6)	11.1

3.4. NGC 1501

NGC 1501 (TIC 084306468, $T_{\rm mag} = 12.40$, $m_{\rm V} = 13.0$) was observed in Sector 19, which spanned about 25 days from 27 November 2019 to 24 December 2019. We performed the FT from the light curve shown in Fig. 2, consisting of 16 893 measurements with a duty cycle of 92.8%. The frequency spectra show a rich content of peaks with 16 pulsational signals above the detection limit of 0.1% FAP = 0.53 ppt. In Table 6 we show the list of periods of NGC 1501. The period spectrum detected with TESS is markedly different from that found by Bond et al. (1996). The 11 periods derived by Bond et al. (1996) are more evenly distributed over a wider range of periods. A graphic comparison between the ground- and space-based period spectra of NGC 1501 is made in Sect. 4.4.

In Fig. 3 we display the FT of NGC 1501 from TESS. The pulsation power concentrates in a frequency (period) interval

Table 6. Independent frequencies, periods, and amplitudes (and their uncertainties) and the S/N in the data of NGC 1501.

Peak	ν (μHz)	Π (s)	A (ppt)	S/N
f_1	67.617(13)	14789.2(2.9)	1.77(9)	15.4
f_2	481.465(43)	2077.00(19)	0.55(9)	4.7
f_3	491.971(34)	2032.64(14)	0.69(9)	6.0
f_4	512.428(20)	1951.49(8)	1.18(9)	10.2
f_5	562.655(31)	1777.29(10)	0.77(9)	6.7
f_6	565.448(39)	1768.51(12)	0.60(9)	5.2
f_7	718.266(35)	1392.24(7)	0.67(9)	5.8
f_8	723.958(19)	1381.295(36)	1.23(9)	10.7
f_9	731.915(14)	1366.279(27)	1.65(9)	14.3
f_{10}	737.094(34)	1356.68(6)	0.69(9)	6.0
f_{11}	741.039(42)	1349.46(8)	0.57(9)	4.9
f_{12}	743.012(25)	1345.872(44)	0.96(9)	8.3
f_{13}	756.948(13)	1321.095(23)	1.93(9)	16.8
f_{14}	762.954(23)	1310.696(40)	1.07(10)	9.3
f_{15}	763.892(22)	1309.086(37)	1.14(10)	9.9
f_{16}	797.047(27)	1254.632(43)	0.87(9)	7.5

from 481 μHz (2077 s) to 797 μHz (1254.6 s). The highest-amplitude (A = 1.938 ppt) peak is located at a frequency of 756.954 μHz in the high-frequency region of the spectrum. The other bunch of peaks lies in the high-frequency region between 718 μHz and 797 μHz. The peak at ∼68 μHz is probably due to contamination because it is not the result of a difference of other frequencies. Moreover, the corresponding period at ∼14 800 s is too long for GW Vir stars, so that it cannot represent an eigenmode of the star. Because this mode is not included in the seismic analysis of this study, we did not consider it further

3.5. NGC 2371

NGC 2371 (TIC 446005482, $T_{\rm mag}$ = 12.90, $m_{\rm V}$ = 13.5) was observed in Sector 20 of TESS (Table 2, Fig. 2). We extracted four frequencies above the detection threshold of 0.9 ppt, corresponding to a 0.1% FAP (Table 7). The periodicities that we extracted from the light curve populate a small region of the power spectrum with periods (frequencies) between 878.524 s (1138.272 μHz) and 1032.558 s (968.467 μHz). In Fig. 3 we show the FT of NGC 2371. The peak at ∼106 μHz is probably due to contamination. This mode is not included in the seismic analysis and is not considered further.

Given the frequency resolution of 0.44 μHz and the average noise level of 0.22 ppt, we did not detect any rotational multiplets in the frequency spectra. However, a possible constant period-spacing pattern is indicated (see Sect. 3).

3.6. K 1−16

K 1−16 (TIC 233689607, $T_{\rm mag}$ = 14.36, $m_{\rm V}$ = 14.96) was observed in sectors 14−17, 19−20, and 22−26 of TESS between 18 July 2019 and 4 July 2020. The light curve of K 1−16 is presented in Fig. 2. The pulsations come and go in individual sectors, which means that the amplitudes and frequencies change significantly. When all data are combined, we obtain a threshold of 0.93 ppt, which implies that only two peaks should be considered to be real. However, given that amplitudes (and frequencies) vary significantly on timescales of weeks or months, like in other

Table 7. Independent frequencies, periods, and amplitudes (and their uncertainties) and the S/N in the data of NGC 2371.

Peak	ν (μHz)	Π (s)	A (ppt)	S/N
f_1	105.657(25)	9464.6(2.2)	1.60(17)	8.0
f_2	1032.553(38)	968.474(36)	1.03(17)	5.1
f_3	1080.538(30)	925.465(26)	1.31(17)	6.5
f_4	1117.180(42)	895.111(34)	0.93(17)	4.6
f_5	1138.274(43)	878.523(33)	0.91(17)	4.5

Table 8. Independent frequencies, periods, and amplitudes and the S/N in the data of K 1−16.

Peak	ν (μHz)	Π (s)	A (ppt)	S/N	$A_{\rm max}$ (ppt)	S/N
(f_1	229.75	4352.6	1.70 [a]	4.2	2.43 [c]	4.2)
f_2	471.74	2119.8	1.78 [a]	4.4	2.30 [d]	4.0
f_3	498.73	2005.1	0.69 [b]	3.3	4.09 [c]	7.1
f_4	541.63 [f]	1846.3	1.08 [b]	5.1	5.50 [c]	9.5
f_5	568.97	1757.6	2.00 [a]	4.9	2.93 [c]	5.1
f_4	581.33 [f]	1720.2	0.90 [b]	4.3	3.00 [e]	4.6
f_6	663.04 [g]	1508.2	0.80 [b]	3.8	3.27 [c]	5.7

Notes. [a]Frequency and amplitude from Sectors 22+23. [b]Frequency and amplitude from all sectors. [c]Maximum amplitude in Sector 23. [d]Maximum amplitude in Sector 22. [e]Maximum amplitude in Sector 17. [f]Could be aliases of super-Nyquist counterparts at 7791.7 and 7752.0 μHz, respectively (cf. text). [g]A close peak at 663.67 μHz could be either an independent frequency or the product of frequency variations (cf. Fig. 7).

PG 1159 stars, a few more peaks have amplitudes well above the threshold in single sectors. When these peaks are added as well, we obtain a list of five frequencies at S/N higher than 4.5 (Table 8). Two more frequencies at 229.75 and 471.74 μHz are included in Table 8 because they reach an S/N of 4.4 and 4.5, respectively, when we consider only a section of the light curve in which they reach the maximum amplitude, from BJD 2458904.35 to 2458954.87 and from 2458900.38 to 2458940.35, respectively (or days 221–271.5 and 217–257 in Fig. 7). Moreover, we investigated the possibility that some of the frequencies in Table 8 may be aliases of super-Nyquist peaks. The possibility of detecting super-Nyquist pulsation frequencies is well described by Murphy (2015), who showed that introducing a time-offset between one sector and the next may greatly help. Even though (unfortunately) this suggestion was not applied to the TESS observing strategy, by chance, a small offset of ∼24 s, that is, 20% of the two-minute sampling time exists between Sectors 17 and 19. In another two cases, between Sectors 19–20 and 20–22, the time is different by ∼4% of the sampling time. This allows us to compare the amplitude of each peak with its super-Nyquist counterpart. Without offsets, for instance, when only Sectors 22+23 are used, in which the star shows the highest number of significant peaks, these amplitudes are almost identical. When we add the sectors with the time offsets, however, the amplitudes differ and the amplitude for the peak at 7752.0 μHz (or 129.0 s) is higher than its sub-Nyquist counterpart at 581.3 μHz. The behavior for the peak at 541.6 μHz and its super-Nyquist counterpart at 7791.7 μHz (or 128.3 s) is also similar, although in this case the effect is less pronounced.

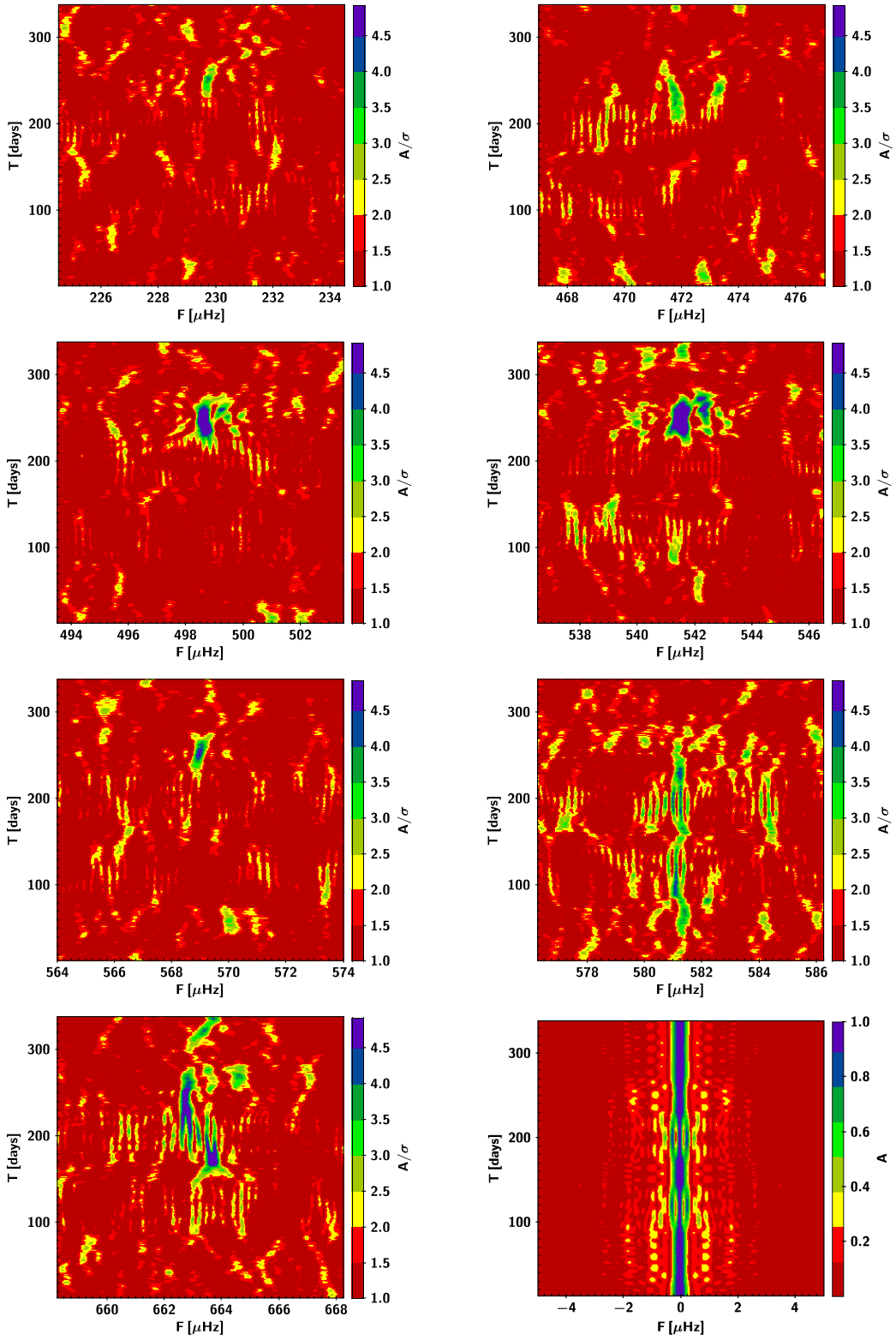

Fig. 7. *Panels 1–7*: sliding FT of K 1−16 centered on the peaks at ~229.7, ~471.7, ~498.7, ~541.6, ~569.0, ~581.3, and ~663.0 μHz. The color-coded amplitudes are given in σ units, i.e., amplitude divided by the mean noise of each FT. The oscillations are not stable over the course of the TESS observations, and in the first ≈200 days (up to Sector 22) some of the modes are absent. *Panel 8*: sliding WF obtained using a single sinusoid of constant frequency and constant amplitude of one, without any noise. The frequency scale is the same in all panels. See text for more details on sFT and sWF computations.

Therefore we cannot totally exclude that the peak at 581.3 μHz is the alias of a super-Nyquist counterpart at 7752.0 μHz (and to a lesser extent, the same might be true for the sub/super-Nyquist pair at 541.63/7791.7 μHz). However, we decided to favor the sub-Nyquist solution based on the findings of Grauer & Bond (1984). Despite their poor frequency resolution that did not

really resolve the region between ≈530 and ≈620 μHz (cf. their Fig. 2b), the main peak they found was at ∼590 μHz, which is quite close to the 581.3 μHz frequency detected by TESS. Moreover, their 50 s binned integration (and sampling) time, with original integrations of 5 s, should have allowed them to detect periods near 130 s. We finally note that the peak at 7752.0 μHz, if true, would have a much larger amplitude due to smearing (see, e.g., Bell et al. 2017), an order of magnitude larger than the amplitude detected in the TESS light curve of 1.35 ppt (and up to 2.54 ppt in Sector 22).

Because the profiles of the peaks associated with unstable modes in the amplitude spectrum may be complex and a prewhitening process gives only rough results, we do not report frequency and amplitude uncertainties in Table 8. Frequencies and amplitudes are those obtained from the complete dataset or from individual sectors if the peak is detected only in some sectors. Moreover, we report in Table 8 also the maximum amplitude registered in a single sector. The long photometric measurements of K 1−16 allow us to construct sFTs to examine the temporal evolution of the pulsation modes over the course of the TESS observations and highlight the dramatic changes in frequency and amplitude of this star. First we divided the TESS light curve into 500 subsets of 17943 data each (corresponding to ∼24.9 days for continuous data) and stepped them by 324 data (0.45 d for continuous data). Afterward, we calculated the FT of each subset and stacked them on top of each other. The sFTs of the seven detected frequencies are shown in Fig. 7 and can be compared with the sliding Window Function (sWF) in the last panel of Fig. 7. The color-coded amplitudes of the sFTs are given in σ units, that is, amplitude divided by the mean noise of each FT. In most cases the frequencies are completely absent (no pulsation) in the first TESS observation sectors and only acquire measurable amplitudes in Sectors 22 and 23. This is particularly evident for the peaks near 498.7, 541.6, and 569.0 μHz.

4. Period spacing

The g modes responsible for the brightness variations of WDs and pre-WDs can be excited in a sequence of consecutive radial orders, k, for each value of ℓ. In the asymptotic limit ($k \gg \ell$), g modes of consecutive radial overtones are approximately uniformly spaced in period (Tassoul et al. 1990). The period spacing is given by

$$\Delta\Pi_\ell^{\rm a} = \frac{\Pi_0}{\sqrt{\ell(\ell+1)}}, \tag{1}$$

where $\Delta\Pi_\ell^{\rm a}$ is the asymptotic period spacing, and Π_0 is a constant defined as

$$\Pi_0 = \frac{2\pi^2}{\left[\int_{r_1}^{r_2} \frac{N}{r} dr\right]}, \tag{2}$$

where N is the Brunt-Väisälä frequency.

While for chemically homogeneous stellar models the asymptotic formula (1) constitutes a very precise description of their pulsational properties, the g-mode period spacings in chemically stratified PG 1159 stars show appreciable departures from uniformity caused by the mechanical resonance called "mode trapping". The presence of one or more narrow regions in which the abundances of nuclear species vary rapidly strongly modifies the character of the resonant cavity in which modes should propagate as standing waves. Specifically, chemical interfaces act like reflecting walls that partially trap certain modes, forcing them to oscillate with larger amplitudes in specific regions

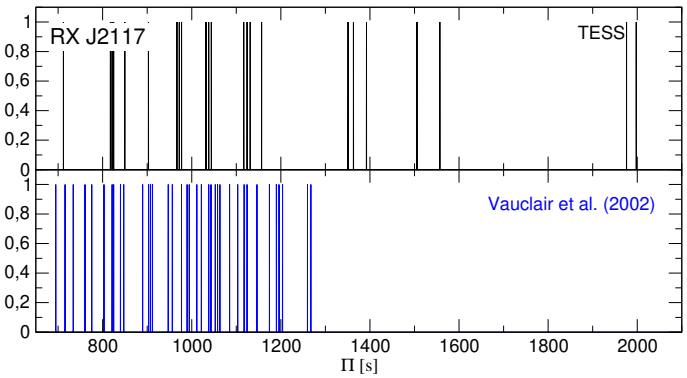

Fig. 8. Schematic distribution of the pulsation periods of RX J2117 according to TESS (15 periods, black lines, *upper panel*), and according to Vauclair et al. (2002; 37 periods, blue lines, *lower panel*). The amplitudes have been arbitrarily set to one for clarity.

that are bounded either by two interfaces or by one interface and the stellar center or surface, and with smaller amplitudes outside of these regions. The requirement for a mode to be trapped is that the wavelength of its radial eigenfunction matches the spatial separation between two interfaces or between one interface and the stellar center or surface. Mode trapping has been the subject of intense study in the context of stratified DA and DB WD pulsations (see, e.g., Brassard et al. 1992; Bradley et al. 1993; Córsico et al. 2002). In the case of PG 1159 stars, mode trapping has been extensively explored by Kawaler & Bradley (1994) and Córsico & Althaus (2006); we refer to these works for details.

4.1. Period spectrum of RX J2117

When we compare the pulsation spectrum of RX J2117 detected by TESS and that observed through the ground-based monitoring by Vauclair et al. (2002), we realize that the pulsation spectra are quite different. To begin with, the number of pulsation periods detected by TESS and reported here (15 periods; see Table 3) is substantially smaller than the number of periods measured by Vauclair et al. (2002), who identified 37 periods (see their Table 9). The differences are not limited only to the number of detected periods, however, which can be mainly attributed to the small size of the TESS telescope, but the distribution of the periods is also completely different. In order to envisage this, in Fig. 8 we schematically plot the periods detected with TESS (upper panel) and the periods detected by Vauclair et al. (2002; lower panel), with arbitrary amplitudes set to one to facilitate visualization. Clearly, the periods of the star detected by TESS are distributed over a much wider range of periods than the periods measured by Vauclair et al. (2002). Only six periods, around 821, 825, 903, 1038, 1044, and 1124 s, are almost identical between the two datasets. The reason for the discrepancy between ground-based and space-based observations is that the TESS mission can only detect large-amplitude modes, both because its telescope is small (15 cm diameter), and because it only observes redder than 6000 Å, where the pulsation amplitudes are small. The WET ground-based telescopes on which the data of Vauclair et al. (2002) are based are much larger.

In order to extract as much information as possible with the tools of asteroseismology, it is crucial to exploit all available pulsation data, which should represent eigenvalues for the star. To identify the pulsation modes and determine the period spacing of RX J2117, which is essential for estimating the stellar mass

Table 9. Enlarged list of periods of RX J2117.

$\Pi_i^{\rm O}$ (s) VEA02	$\Pi_i^{\rm O}$ (s) TESS	$\Pi_{\rm fit}$ (s)	$\delta\Pi$ (s)	$\ell^{\rm O}$
692.267 (*)		691.298	0.969	1
712.975 (*)		712.967	0.008	1
733.948 (*)		734.636	−0.688	1
757.354 (*)		756.305	1.049	1
778.921 (*)		777.974	0.947	1
799.495 (*)		799.643	−0.148	1
	817.375			1
821.145	821.105 (*)	821.312	−0.207	1
	824.880			1
843.692 (*)		842.981	0.711	1
885.736 (*)		886.319	−0.583	1
	902.761			?
907.489 (*)		907.988	−0.499	1
951.750 (*)		951.326	0.424	1
	966.785			1
972.247	972.073 (*)	972.995	−0.922	1
994.387 (*)		994.664	−0.277	1
1016.467 (*)		1016.333	0.134	1
	1031.978			1
1038.118	1038.120 (*)	1038.002	0.118	1
	1044.041			1
1058.026 (*)		1059.671	−1.645	1
1103.292 (*)		1103.009	0.283	1
1124.117	1124.156 (*)	1124.678	−0.522	1
	1131.200			1
1146.346 (*)		1146.347	−0.001	1
1189.956 (*)		1189.685	0.271	1
	1350.870			?
	1557.010	1558.058	−1.048	1
	1976.060			?
	1997.760			?

Notes. Column 1 corresponds to 20 $\ell = 1$ $m = 0$ periods measured by Vauclair et al. (2002; VEA02), and Col. 2 corresponds to the 15 periods detected by TESS (Table 3). The periods with an asterisk were used in the linear least-squares fit (Fig. 10).

(see Sect. 7.1), we therefore decided to expand the list of periods by adding the 20 dipole $m = 0$ periods found by Vauclair et al. (2002) to the list of periods collected by TESS (Table 3). Only half of these 20 $m = 0$ periods were directly detected, the others were deduced through a detailed analysis from the presence of the $m = -1$ and/or $m = +1$ components of each $\ell = 1$ triplet. For the periods close to 821 s, 972 s, 1038 s, and 1124 s that were detected (or inferred) in both datasets, we adopted the periods measured by TESS because they are more accurate in general due to the continuous long dataset. The extended list of periods to be used in our analysis contains 31 periods and is shown in Table 9.

We searched for a constant period spacing in the data of RX J2117 using the Kolmogorov-Smirnov (K-S; Kawaler 1988), the inverse variance (I-V; O'Donoghue 1994), and the Fourier transform (F-T; Handler et al. 1997b) significance tests. In the K-S test, the quantity Q is defined as the probability that the observed periods are randomly distributed. Thus, any uniform or at least systematically non-random period spacing in the period spectrum of the star will appear as a minimum in Q. In the I-V test, a maximum of the inverse variance will indicate a constant

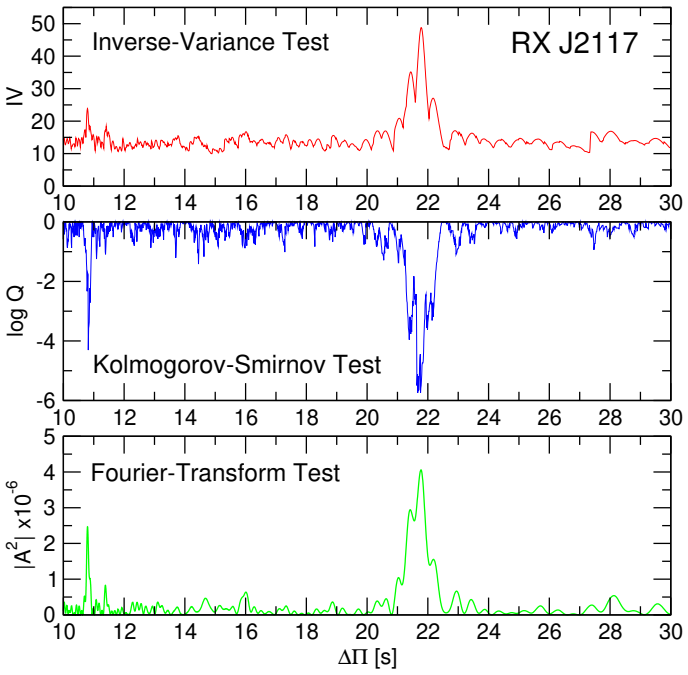

Fig. 9. I-V (*upper panel*), K-S (*middle panel*), and F-T (*bottom panel*) significance tests to search for a constant period spacing in RX J2117. The tests are applied to the set of 31 pulsation periods of Table 9. A clear signal of a constant period spacing at ∼21.8 s is evident. See text for details.

period spacing. Finally, in the F-T test, we calculate the FT of a Dirac comb function (created from a set of observed periods), and then we plot the square of the amplitude of the resulting function in terms of the inverse of the frequency. A maximum in the square of the amplitude indicates a constant period spacing.

Figure 9 displays the results of applying the K-S, I-V, and F-T significance tests to the set of 31 periods of Table 9. The three tests indicate a pattern of $\ell = 1$ constant period spacing of $\Delta\Pi \sim 22$ s. Another peak lies at ∼11 s. This is the subharmonic of this $\ell = 1$ period spacing ($\Delta\Pi/2$). To derive a refined value of the period spacing, we carried out a linear least-squares fit to the 20 periods marked with an asterisk in Table 9, excluding those with $m \neq 0$ and those for which mode identification is uncertain. We obtain a period spacing of $\Delta\Pi = 21.669 \pm 0.030$ s (see the upper panel of Fig. 10). This value is very close to the period spacing derived by Vauclair et al. (2002) on the basis of ground-based observations alone ($\Delta\Pi = 21.618 \pm 0.008$ s). With the derived value of the mean period spacing we determined one more period compatible with the $\ell = 1$ string, at about 1557 s. The remaining periods can be associated with $\ell = 1$ modes (which, due to mode trapping effects, deviate from the derived sequence of almost equally spaced periods) or with modes with $\ell = 2$ (or possibly higher). The relevance of finding a constant period spacing is twofold: on the one hand, it allows the identification of the harmonic degree of the modes (i.e., the assignment of the harmonic degree ℓ; see Table 9), and on the other hand, it enables us to estimate the stellar mass. This is addressed for RX J2117 in Sect. 7.1.

In the lower panel of Fig. 10 we show the residuals ($\delta\Pi$) between the observed periods ($\Pi_i^{\rm O}$) and the periods derived from the mean period spacing ($\Pi_{\rm fit}$). The presence of several minima in the distribution of residuals strongly suggests the mode-trapping effects caused by internal chemical transition regions.

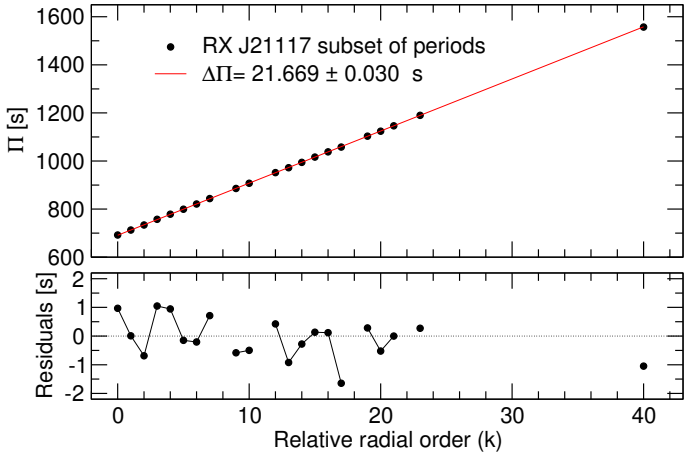

Fig. 10. *Upper panel*: linear least-squares fit to the 20 periods of RX J2117 marked with asterisks in Table 9. The derived period spacing from this fit is $\Delta\Pi = 21.669 \pm 0.030$ s. *Lower panel*: residuals of the period distribution relative to the mean period spacing, revealing signals of mode trapping in the period spectrum of RX J2117. Modes with consecutive radial order are connected with a thin black line.

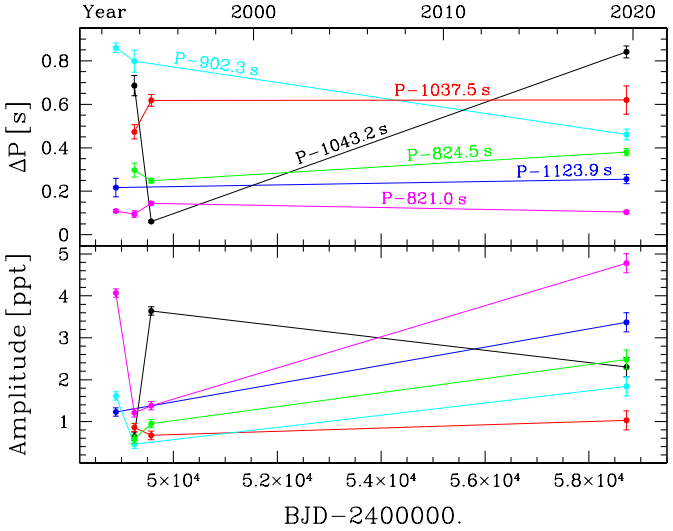

Fig. 11. Period variations (*upper panels*) and amplitudes (*lower panels*) of the six periods of RX J2117 that are common to the Vauclair et al. (2002) and TESS datasets. In the *upper panel* we have subtracted a constant value from each period in order to fit all periods within a narrow range.

Because six periods of RXJ 2117 that are common to both Vauclair et al. (2002) and TESS datasets were measured at different epochs spanning 26 or 27 years, it is interesting to test their stability in time. However, with only a few measurements and a ∼25-year gap, we cannot know if the periods that seem relatively stable in the upper panel of Fig. 11 are really stable. On the other hand, at least two periods, those near 902 and 1043 s, show significant period variations. In particular, the period at ∼1043 s shows strong variations that are clearly anticorrelated with amplitude variations (lower panel of Fig. 11), and we know that correlated or anticorrelated variations of period and amplitude are typical of nonlinear interactions between different pulsation modes (see, e.g., Zong et al. 2018). The lower panel of Fig. 11 shows that except for the period at ∼1037 s, all the others vary in amplitude. In addition to the period at ∼1043 s, which we have already mentioned, another period at 821.1 s, rather stable over the period, shows strong variations in amplitude, up to a factor ∼4 in about one year.

4.2. Period spectrum of HS 2324

At variance with the case of RX J2117, for HS 2324 we find a TESS pulsation spectrum quite similar to that resulting from the ground-based observations. In Fig. 12 we schematically show the 12 periods detected with TESS (upper panel), and the 19 periods detected by Silvotti et al. (1999) (lower panel). Only two periods, around 2110 s and 2194 s, are nearly identical in the two datasets. In order to find a period spacing in HS 2324, we enlarged the list of periods by adding some of the 19 periods observed by Silvotti et al. (1999).

In that article, the authors noted that the solution reported in their Table 2 was not univocal, probably because of insufficient frequency resolution and/or amplitude variations with time. We reanalyzed those data with different criteria for the pre-whitening procedure, in order to verify which frequencies are found in different solutions, and we selected 11 periods that were added to the list of periods collected by TESS (Table 4). The periods are slightly different from those in Table 2 of Silvotti et al. (1999) because we used the mean values of the different solutions. For the two periods found in both datasets

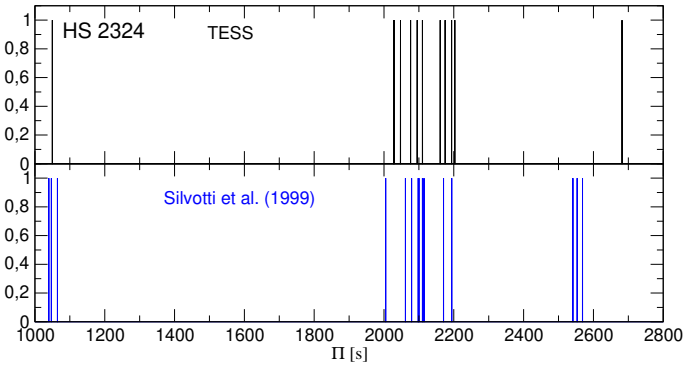

Fig. 12. Schematic distribution of the pulsation periods of HS 2324 according to TESS data (12 periods, black lines, *upper panel*), and according to Silvotti et al. (1999; 19 periods, blue lines, *lower panel*). The amplitudes have been arbitrarily set to one for clarity.

at ∼2110 s and ∼2194 s, we adopted the periods measured by TESS because they have smaller uncertainties. The extended list of periods to be used in our analysis contains 21 periods and is presented in Table 10.

In Fig. 13 we show the results of applying the statistical tests to the set of 21 periods of Table 10. The three tests support the existence of a mean period spacing of about 16 s, which corresponds to our expectations for a dipole ($\ell = 1$) sequence. We can safely rule out that this peak corresponds to $\ell = 2$ modes because in that case, we should find a peak at $16\,\mathrm{s} \times \sqrt{3} \sim 28$ s associated with $\ell = 1$ modes, according to Eq. (1). This is not observed. When we assume that the peak at ∼16 s is associated with $\ell = 1$ modes, then if a series of quadrupole ($\ell = 2$) modes were present, we should find a spacing of periods of ∼9 s. This is not observed in our analysis (see Fig. 13). To determine the period spacing precisely, we performed a linear least-squares fit (plotted in the upper panel of Fig. 14) using only nine periods, those marked with an asterisk in Table 10 because the other potential $\ell = 1$ periods are much shorter or much longer and not well constrained, and we risk to assign them an incorrect identification. We obtain a period spacing $\Delta\Pi = 16.407 \pm 0.062$ s,

Table 10. Enlarged list of periods of HS 2324.

Π_i^O (s) SEA99	Π_i^O (s) TESS	Π_{fit} (s)	$\delta\Pi$ (s)	ℓ^O
1039.02				?
1047.10		1044.930	2.170	1
	1049.877			?
2005.78				?
	2027.520			?
	2029.350 (*)	2029.350	0.000	1
	2047.260 (*)	2045.757	1.503	1
2059.97 (*)		2062.164	−2.194	1
	2076.110			?
2078.59 (*)		2078.571	0.019	1
	2095.046 (*)	2094.978	0.068	1
2098.67				?
2109.53	2110.152 (*)	2111.385	−1.233	1
	2160.970 (*)	2160.606	0.364	1
2170.49				?
	2175.290 (*)	2177.013	−1.723	1
2194.12	2193.420 (*)	2193.420	0.000	1
	2202.990			?
2553.23		2554.374	−1.144	1
2568.86		2570.781	−1.921	1
	2682.050	2685.630	−3.580	1

Notes. Column 1 corresponds to a subset of 11 periods estimated by Silvotti et al. (1999) (SEA99) with small differences (see text), and Col. 2 corresponds to the 12 periods detected with TESS (Table 4). The periods with an asterisk are those used in the linear least-squares fit (Fig. 14).

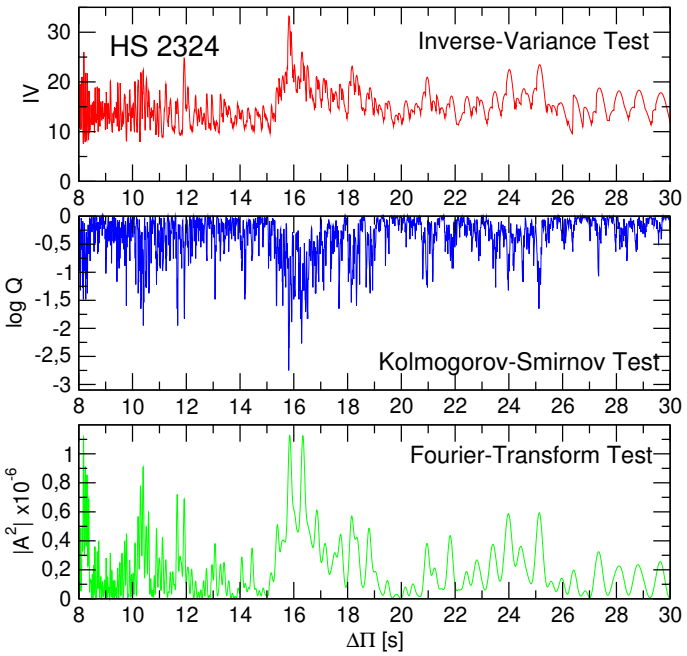

Fig. 13. I-V (*upper panel*), K-S (*middle panel*), and F-T (*bottom panel*) significance tests to search for a constant period spacing in HS 2324. The tests are applied to the 21 pulsation periods in Table 10. A clear signal of a constant period spacing at ∼16 s is evident. See text for details.

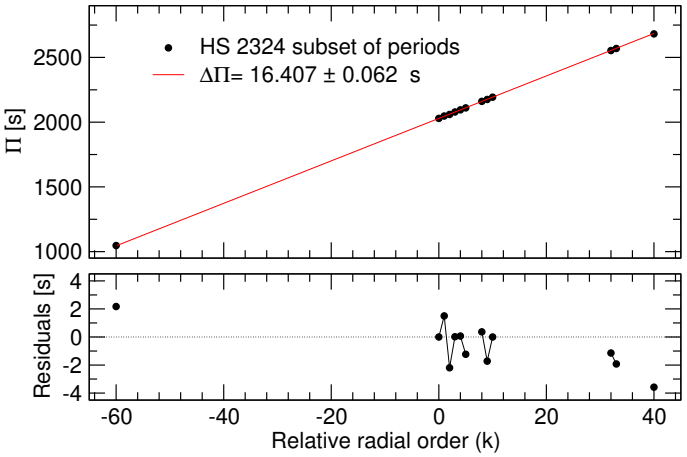

Fig. 14. *Upper panel*: linear least-squares fit to the nine periods of HS 2324 marked with an asterisk in Table 4. The derived dipole ($\ell = 1$) mean period spacing from this fit is $\Delta\Pi = 16.407 \pm 0.062$ s. *Lower panel*: residuals of the period distribution relative to the mean period spacing, showing observational evidence of mode trapping in the pulsation spectrum of HS 2324. Modes with consecutive radial order are connected with a thin black line.

and with this value we determine four more periods compatible with the $\ell = 1$ sequence, at about 1047, 2553, 2569, and 2682 s. When we include these four periods in the linear least-squares fit as well, we obtain $\Delta\Pi = 16.371$ s. We can conclude that Table 10 contains an incomplete sequence of 13 modes $\ell = 1$. The remaining periods, on the other hand, can be associated with modes with $\ell = 1$ or modes with $\ell = 2$ as well. In Sect. 7.2 we obtain an estimate of the stellar mass of HS 2324 on the basis of the period spacing. The lower panel of Fig. 14 displays the residuals between the observed periods and the periods derived from the mean period spacing. We note several minima in the distribution of residuals, similar to the case of RX J2117, which suggests mode trapping caused by gradients in the chemical composition.

As discussed in Sect. 3.2, a rotational splitting of ∼4.3 μHz cannot be completely discarded in the frequency spectrum of HS 2324. In this case, we should have to consider only one component of the two possible incomplete triplets constituted by the pairs (481.67, 477.316) μHz and (492.769, 488.458) μHz when we search for a constant period spacing. On the one hand, from the pair (481.67, 477.316) μHz we can adopt the frequency 477.316 μHz, which corresponds to the period 2095.046 s, and discard the period 2076.11 s from the analysis. This is precisely what we did in the analysis above. In relation to the other pair of frequencies, based on the arguments discussed in the Sect. 3.2, we can adopt the frequency 492.769 μHz, which corresponds to the period 2029.35 s. This implies discarding the period 2047.26 s (frequency 488.458 μHz) from our analysis, which makes sense because it has a much lower amplitude than the period 2029.35 s (492.769 μHz) (see Table 4 and Fig. 6). Repeating the calculation of the period spacing, but this time neglecting the period of 2047.26 s from the analysis (i.e., adopting a list of eight periods), we obtain $\Delta\Pi = 16.421 \pm 0.120$ s, virtually the same period spacing as obtained above ($\Delta\Pi = 16.407 \pm 0.062$ s). In summary, when we consider the possible existence of two incomplete rotational triplets, it does not alter the results in relation to the period spacing of HS 2324.

Because the epochs of the two data sets of HS 2324 differ by 22 years, we can test their temporal stability by comparing the values of the two periods found in both datasets. However, we know that the formal uncertainties given in Table 2 of Silvotti et al. (1999) are underestimated because the

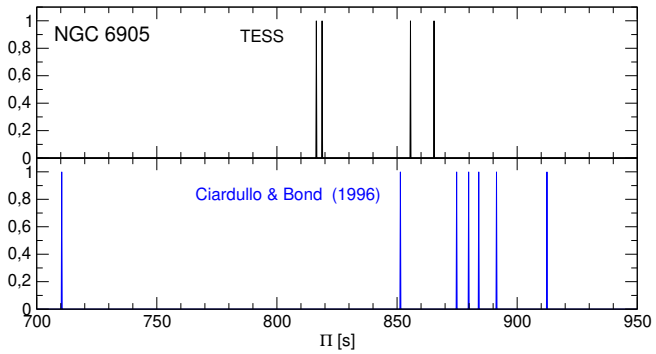

Fig. 15. Schematic distribution of the pulsation periods of NGC 6905 according to TESS (black lines, *upper panel*), and according to Ciardullo & Bond (1996) (blue lines, *lower panel*). The amplitudes have been arbitrarily set to one for clarity.

periods change slightly depending on which solution is adopted. By testing different solutions, we obtain 2109.53 ± 0.66 and 2194.12 ± 0.15 from the 1997 data with more realistic uncertainties. The much larger uncertainty on the first period is due to the close-by peaks that are not visible in the TESS run, which are probably the cause of the varying amplitude (~3.3 ppt in 1997, 6.0 ppt in 2019). In 2019 the periods are 2110.15 ± 0.04 s and 2193.42 ± 0.06 s (adopting the formal uncertainties of the fit). Only for the second one near 2193 s, which has a fairly stable amplitude (4.3 ppt in 1997 and 4.0 ppt in 2019, considering also the much redder sensitivity of TESS), the period change in time is significant ($4.7\,\sigma$), corresponding to $\dot{\Pi} = (-1.0 \pm 0.3) \times 10^{-9}$ s/s. Even though this value is close to theoretical predictions (see Sect. 7.2), the fact that we have only two measurements and that we know that the periods may have irregular variations on different timescales (as we have seen for RX J2117) suggests caution.

4.3. Period spectrum of NGC 6905

As in the case of RX J2117, we find pulsation spectra of NGC 6905 quite different from the results of ground-based observations. In Fig. 15 we schematically show the 4 periods detected with TESS (upper panel, black lines) and the 7 periods detected by Ciardullo & Bond (1996) (lower panel, blue lines), with arbitrary amplitudes set to one to facilitate visualization. In order to search for a period spacing in NGC 6905, we enlarged the list of periods by adding the seven periods measured by Ciardullo & Bond (1996) to the list of periods collected by TESS. The extended list of periods to be used in our analysis, which contains 11 periods, is presented in Table 11.

We applied the three statistical tests adopting the complete list of 11 periods of Table 11, and we obtained a clear indication of a constant period spacing of ~12 s, as shown in Fig. 16. A priori, we cannot know to which harmonic degree this apparent constant period spacing corresponds. Because it is so short, we are tempted to assume that it is a period spacing of $\ell = 2$ modes, but in this case, we should find a period spacing of about 21 s corresponding to $\ell = 1$ modes, which is absent. The absence of a period spacing at ~21 s is not, however, a strong reason to discard the possibility that the period spacing of ~12 s is associated with a sequence of $\ell = 2$ modes. It might be possible that the $\ell = 1$ modes (and the associated period spacing) are inhibited for some reason. For example, it might be that $\ell = 1$ modes are not excited at the effective temperature and gravity of NGC 6905, but $\ell = 2$ modes are unstable. In Sect. 7.3 we consider the possibilities that $\Delta\Pi \sim 12$ s is associated with $\ell = 1$ or $\ell = 2$ modes when the stellar mass of NGC 6905 is estimated.

Table 11. Enlarged list of periods of NGC 6905.

$\Pi_i^{\rm O}$ (s) CB96	$\Pi_i^{\rm O}$ (s) TESS	$\Pi_{\rm fit}$ (s)	$\delta\Pi$ (s)	$\ell^{\rm O}$
710.37 (*)		710.908	−0.538	1
	816.337			1
	818.887 (*)	818.632	0.255	1
851.38				?
	855.613 (*)	854.540	1.074	1
	865.490 (*)	866.509	−1.109	1
874.80				?
879.79 (*)		878.479	1.311	1
884.00				?
891.39 (*)		890.448	0.942	1
912.36 (*)		914.386	−2.026	1

Notes. Column 1 corresponds to the 7 periods measured by Ciardullo & Bond (1996) (CB96), and Col. 2 corresponds to the 4 periods detected by TESS. Columns 3–5 have the same meaning as in Table 9. The periods with an asterisk are those used in the linear least-squares fit (Fig. 17).

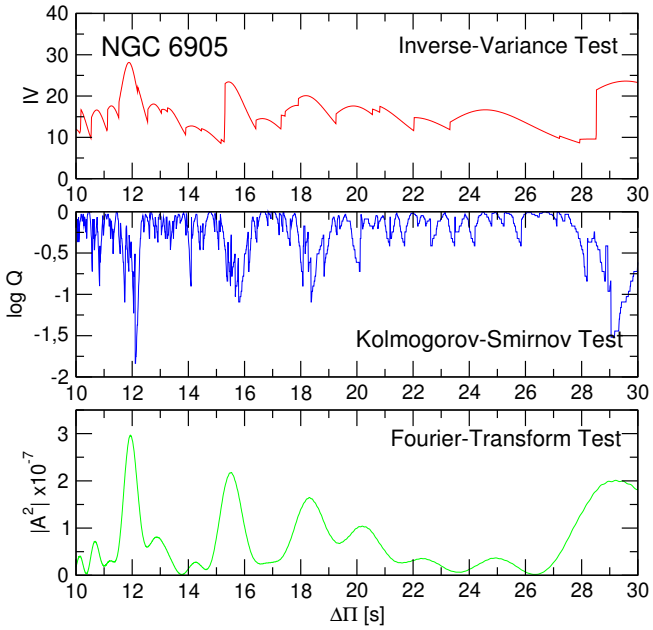

Fig. 16. I-V (*upper panel*), K-S (*middle panel*), and F-T (*bottom panel*) significance tests to search for a constant period spacing in NGC 6905. The tests are applied to the 11 pulsation periods of Table 11. A clear signal of a constant period spacing at ~12 s is evident. See text for details.

In order to refine this period-spacing value, we first performed a linear least-squares fit to the periods marked with an asterisk in Table 11, except for the period at 710.37 s, because it is far from the remaining periods, and this could affect the assignment of its relative radial order. We obtain a period spacing $\Delta\Pi = 11.7769 \pm 0.2247$ s. The average value of the residuals resulting from the difference between the periods observed and those calculated from the period spacing obtained is 1.395 s. We repeated the linear least-squares fit, but this time including the period at 710.37 s, and we obtained $\Delta\Pi = 11.9693 \pm 0.0988$ s. This period spacing is slightly longer than that derived when the

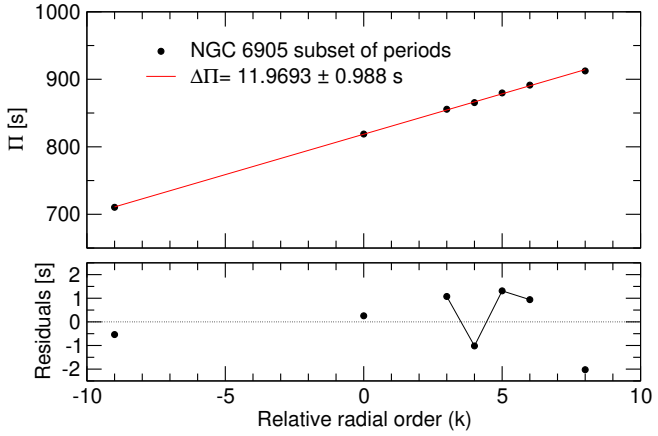

Fig. 17. *Upper panel*: linear least-squares fit to the 7 periods of NGC 6905 marked with an asterisk in Table 11. The derived period spacing from this fit is $\Delta\Pi = 11.9693 \pm 0.0988$ s. *Lower panel*: residuals of the period distribution relative to the dipole mean period spacing. Modes with consecutive radial order are connected with a thin black line.

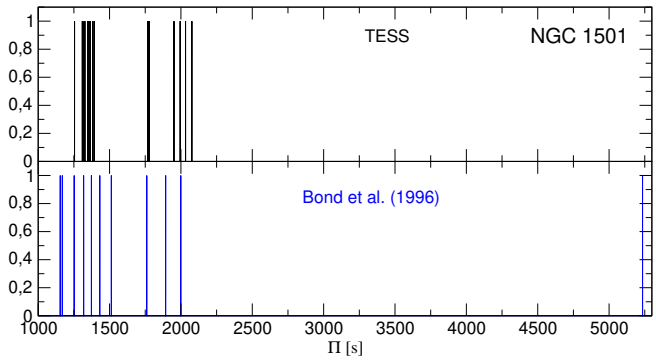

Fig. 18. Schematic distribution of the pulsation periods of NGC 1501 according to TESS (black lines, *upper panel*), and according to Table 4 of Bond et al. (1996) (blue lines, *lower panel*). The amplitudes have been arbitrarily set to one for clarity.

period at 710.37 s in the linear least-squares fit is neglected, but the uncertainty is more than two times smaller. In addition, the average of the residuals in this case is 1.023 s, so the fitted periods match the observed periods much better than before. For this reason, we adopt $\Delta\Pi = 11.9693 \pm 0.0988$ s as the period spacing for NGC 6905. We show the periods derived with the fit ($\Pi_{\rm fit}$) and the residuals ($\delta\Pi$) in Cols. 3 and 4, respectively, of Table 11. In the last column we show the possible identification of the fitted periods with $\ell = 1$ modes, although, as stated above, they might be all associated with $\ell = 2$ modes. In the upper panel of Fig. 17 we show the fit, whereas in the lower panel we depict the residuals.

4.4. Period spectrum of NGC1501

As for some of the targets (RX J2117 and NGC 6905) analyzed before, a comparison of the pulsation spectrum of NGC 1501 detected by TESS with that obtained through the ground-based monitoring by Bond et al. (1996) reveals that the pulsation spectra are markedly different. In Fig. 18 we schematically show the periods detected with TESS (upper panel, black lines) and the 11 periods detected by Bond et al. (1996) (lower panel, blue lines), specifically, those of their Table 4, with arbitrary amplitudes set to one to facilitate visualization. As before, we consider here the composed pulsation spectrum of NGC 1501, that is, the list of periods measured by TESS along with the periods determined by Bond et al. (1996). The extended list of periods to be used in our analysis is presented in Cols. 1 and 2 of Table 12.

In Fig. 19 we show the results of applying the statistical tests to the complete set of 26 periods of Table 12. The three tests support the existence of two period spacings of about 11.9 s and 20.1 s. The ratio between the two values is $20.1/11.9 = 1.689$, close to the expected value of $\sqrt{3} = 1.732$ when we assume that these are periods spacings associated with $\ell = 1$ ($\Delta\Pi_{\ell=1} \sim 20.1$ s) and $\ell = 2$ ($\Delta\Pi_{\ell=1} \sim 11.9$ s), according to Eq. (1). Period spacings due to $\ell = 1$ and $\ell = 2$ modes in the same object are rare in the context of GW Vir stars, the only known case so far is the prototypical variable star PG 1159−035 (see, e.g., Winget et al. 1991; Costa et al. 2008).

We alternatively considered in our analysis the 9 ($m = 0$) periods of the Table 7 of Bond et al. (1996), which consist of a composition of the data from that work plus archival period data on NGC 1501. However, by putting together those periods with the periods measured with TESS in this paper, we do not obtain any clear pattern of constant period spacing, and therefore we do not consider them here.

We performed a linear least-squares fit using the 14 periods marked with an asterisk in Table 12, which gives a period spacing $\Delta\Pi_{\ell=1} = 20.1262 \pm 0.0123$ s associated with $\ell = 1$ modes. We performed a second least-squares fit employing the 9 periods marked with two asterisks in the same table, which gives a period spacing $\Delta\Pi_{\ell=2} = 11.9593 \pm 0.0520$ s that is probably associated with $\ell = 2$ modes. With $\Delta\Pi_{\ell=2}$, we computed an additional period compatible with the $\ell = 2$ sequence, at about 1760.7 s. The ratio between the two period spacings is $20.1262/11.9593 = 1.683$. The fits are plotted in the upper panel of Fig. 20, and the residuals are depicted in the middle panel ($\ell = 1$) and in the lower panel ($\ell = 2$).

Two periods (1318.46 s and 1999.16 s) do not fit the $\ell = 1$ nor the $\ell = 2$ series of periods with constant period spacing. For these two periods, we cannot determine the harmonic degree. These periods either correspond both to $\ell = 1$ or $\ell = 2$ modes that are departed from the sequences of equally spaced periods due to mode trapping effects, or they can be alternatively interpreted as $m \neq 0$ components of incomplete rotational multiplets, but we have no indication of rotational multiples in this star. Alternatively, these two periods could correspond to $\ell = 3$ modes, although this is unlikely due to the low chance of being detected by the geometric cancellation effects (Dziembowski 1977).

In closing this section, we call the attention to a possible alternative interpretation of the period spacing derived for NGC 1501. Specifically, Fig. 19 shows a strong peak for $\Delta\Pi \sim 8-9$ s. This peak could be associated to the $\ell = 2$ period spacing of the star. If this were the case, then we should expect to find a peak corresponding to the $\ell = 1$ period spacing at $\Delta\Pi \sim 16$ s. However, no such peak is visible in any of the tests. For this reason, we rule this possibility out.

In Sect. 7.4 we obtain an estimate of the stellar mass of NGC 1501 on the basis of the period-spacing values derived in this section, $\Delta\Pi_{\ell=1} = 20.1262 \pm 0.0123$ s and $\Delta\Pi_{\ell=2} = 11.9593 \pm 0.0520$ s.

4.5. Period spectrum of NGC 2371

NGC 2371 was observed from the ground by Ciardullo & Bond (1996). An illustrative comparison between periods detected

Table 12. Enlarged list of periods of NGC 1501.

$\Pi^{\rm O}$ (s) BEA96	$\Pi^{\rm O}$ (s) TESS	$\Pi^{\ell=1}_{\rm fit}$ (s)	$\delta\Pi^{\ell=1}$ (s)	$\Pi^{\ell=2}_{\rm fit}$ (s)	$\delta\Pi^{\ell=2}$ (s)	$\ell^{\rm O}$
1154.36 (**)				1155.070	−0.710	2
1168.90 (*)		1168.730	0.170			1
1251.91 (*)		1249.235	2.675			1
	1254.632 (**)			1250.744	3.888	2
	1309.086 (**)			1310.541	−1.455	2
	1310.696 (*)	1309.613	1.083			1
1318.46						?
	1321.095 (**)			1322.500	−1.405	2
	1345.872 (**)			1346.419	−0.547	2
	1349.460 (*)	1349.866	−0.406			1
	1356.680 (**)			1358.042	−1.362	2
	1366.279 (*)	1369.992	−3.713			1
1372.94 (**)				1370.337	2.603	2
	1381.295 (**)			1382.297	−1.002	2
	1392.240 (*)	1390.118	2.122			1
1431.53 (*)		1430.371	1.159			1
1512.66 (*)		1510.875	1.785			1
1760.73				1764.994	−4.264	2
	1768.510 (*)	1772.516	−4.006			1
	1777.290 (**)			1776.954	0.336	2
1892.95 (*)		1893.273	−0.323			1
	1951.490 (*)	1953.652	−2.162			1
1999.16						?
	2032.640 (*)	2034.157	−1.547			1
	2077.000 (*)	2074.409	2.591			1
5234.81 (*)		5234.222	0.588			1

Notes. Column 1 corresponds to the 11 periods of Table 4 of Bond et al. (1996) (BEA96), and Col. 2 corresponds to the 15 periods detected by TESS (Table 6). Columns 3 and 4 (5 and 6) correspond to the fitted periods from the $\ell = 1$ ($\ell = 2$) period spacing, and Col. 7 gives the "observed" harmonic degree.

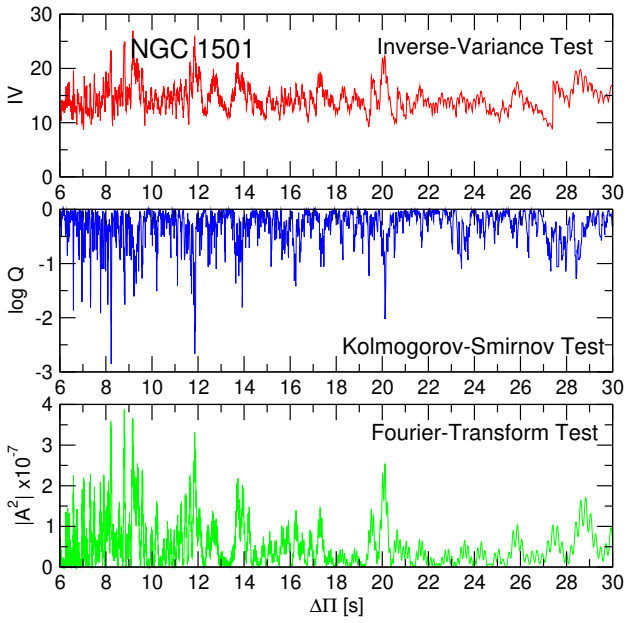

Fig. 19. I-V (*upper panel*), K-S (*middle panel*), and F-T (*bottom panel*) significance tests to search for a constant period spacing in NGC 1501. The tests are applied to the pulsation periods in Table 12 that are marked with an asterisk. The three tests indicate clear signals of two constant period spacings of ∼11.9 s and ∼20.1 s. See text for details.

from ground-based observations and those detected by TESS is shown in Fig. 21. An examination of this figure reveals that the two pulsation spectra are markedly different. In particular, Ciardullo & Bond (1996) reported several periods longer than the longest period detected with TESS (∼968 s). As before, we adopted an augmented pulsation spectrum of NGC 2371, composed of the periods measured by TESS along with the periods determined by Ciardullo & Bond (1996), specifically, those of their Table 4, which are considered as secure. The extended list of periods to be used in our analysis is presented in Table 13.

In Fig. 22 we show the results of applying the statistical tests to the set of periods of Table 13 marked with an asterisk. The three tests support the existence of a mean period spacing of about 14.5 s, which corresponds to our expectations for a dipole ($\ell = 1$) sequence. A linear least-squares fit using the eight periods marked with an asterisk in Table 13 gives a period spacing $\Delta\Pi = 14.5312 \pm 0.0226$ s. The fit is plotted in the upper panel of Fig. 23, and the residuals are depicted in the lower panel of the same figure. In Sect. 7.5 we obtain an estimate of the stellar mass of NGC 2371 on the basis of the period spacing.

4.6. Period spectrum of K 1−16

K 1−16 was observed from the ground by Grauer & Bond (1984), detecting a complex power spectrum with a dominant periodicity of ∼1700 s. After the delivery of TESS data from sectors 14 and 15, the star showed no variability. Finally, with the

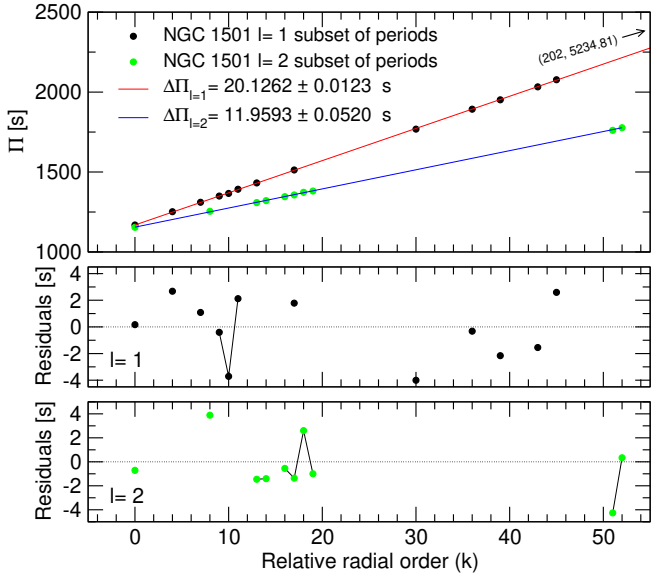

Fig. 20. *Upper panel*: linear least-squares fits to the 14 dipole periods of NGC 1501 marked with an asterisk and the 9 quadrupole periods marked with two asterisks in Table 6. The derived period spacings from these fits are $\Delta\Pi_{\ell=1} = 20.1262 \pm 0.0123$ s and $\Delta\Pi_{\ell=2} = 11.9593 \pm 0.0520$ s, respectively. *Middle panel*: residuals of the $\ell = 1$ period distribution relative to the dipole mean period spacing. *Lower panel*: residuals of the $\ell = 2$ period distribution relative to the quadrupole mean period spacing. Modes with consecutive radial order are connected with a thin black line.

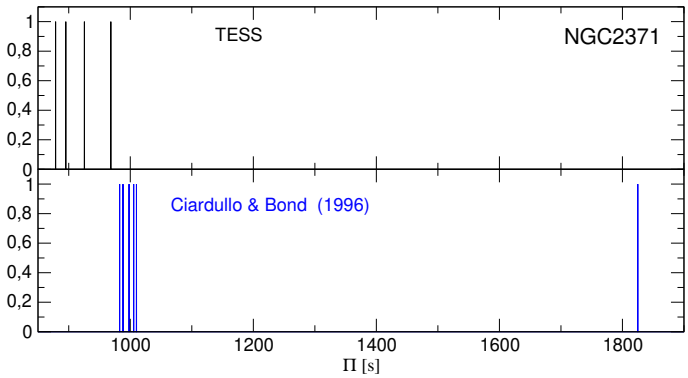

Fig. 21. Illustrative distribution of the pulsation periods of NGC 2371 according to TESS (black lines, *upper panel*), and according to Ciardullo & Bond (1996), their Table 4 (blue lines, *lower panel*). The amplitudes have been arbitrarily set to one for clarity.

release of observations from Sectors 16–17, 19–20, and 22–26, a total of six (or seven) periods were detected. However, the power spectrum is so complex and noisy that the values of the periods are hard to estimate (Table 8). The peak at the frequency 7752 μHz corresponds to a period of 129 s. This is a very short period to be excited in GW Vir stars by the $\kappa - \gamma$ mechanism. If this period is real, it might therefore correspond to a low-order mode excited by the ε mechanism acting at the He-burning shell (Córsico et al. 2009b). When observations from the ground and from space are considered together, the star exhibits a total of at least seven periods that vary in amplitude on weekly timescales. We did not find any clear regularity in the spacing of periods that can give us any clue to its stellar mass, as was the case with the other targets in this study. Because the spectrum of the K 1–16 periods is so complex and extremely variable and so few periods

Table 13. Enlarged list of periods of NGC 2371.

Π^{O} (s) CB96	Π^{O} (s) TESS	Π_{fit} (s)	$\delta\Pi$ (s)	ℓ^{O}
	878.523 (*)	880.598	−2.075	1
	895.111 (*)	895.129	−0.018	1
	925.465 (*)	924.192	1.273	1
	968.474 (*)	967.785	0.689	1
982.8 (*)		982.316	0.158	1
988.2				?
998.0 (*)		996.848	1.152	1
1005.6				?
1010.0 (*)		1011.379	−1.379	1
1825.0 (*)		1825.126	−0.126	1

Notes. Column 1 corresponds to the 6 secure periods of Table 4 of Ciardullo & Bond (1996) (CB96), and Col. 2 corresponds to the 4 periods detected by TESS (Table 7). The periods with an asterisk are those used in the linear least-squares fit (Fig. 23). Columns 3–5 have the same meaning as in Table 9.

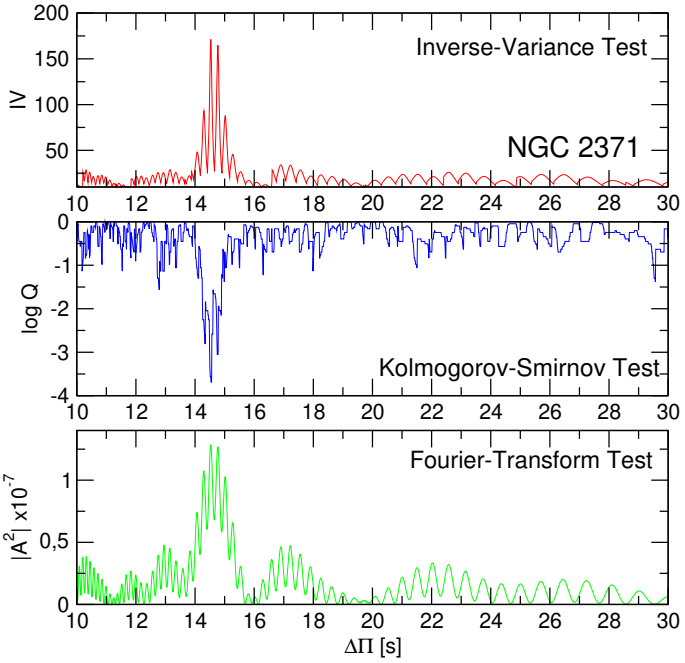

Fig. 22. I-V (*upper panel*), K-S (*middle panel*), and F-T (*bottom panel*) significance tests to search for a constant period spacing in NGC 2371. The tests are applied to the pulsation periods in Table 13 that are marked with an asterisk. The three tests indicate clear signals of a constant period spacing of ∼14.5 s. See text for details.

are available, we are prevented from carrying out an in-depth asteroseismological analysis of this star with either period spacing or individual periods.

5. Evolutionary models and numerical codes

The asteroseismological analysis presented in this work relies on a set of detailed stellar models that take the complete evolution of the PG 1159 progenitor stars into account. Specifically, the stellar models were extracted from the evolutionary calculations presented by Althaus et al. (2005) and Miller Bertolami & Althaus (2006), who computed the complete

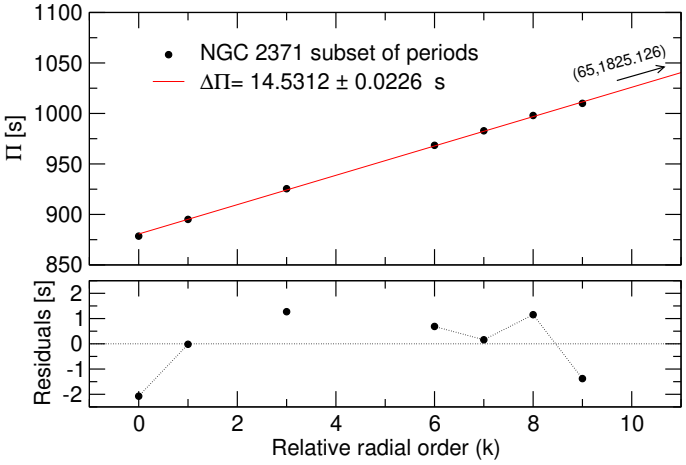

Fig. 23. *Upper panel*: linear least-squares fit to the eight periods of NGC 2371 marked with asterisk in Table 7. *Lower panel*: residuals between the observed and the fitted periods. The derived period spacing from this fit is $\Delta\Pi = 14.5312 \pm 0.0226$ s.

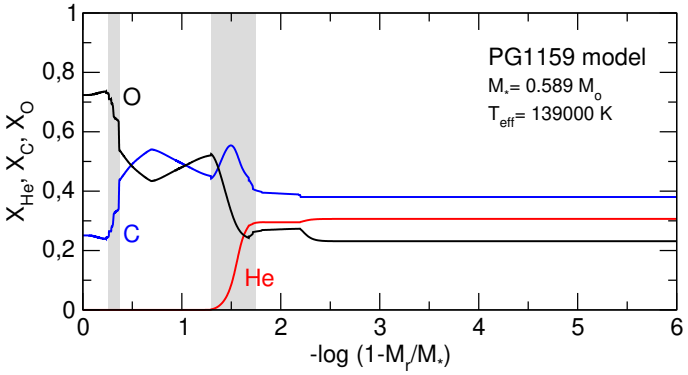

Fig. 24. Internal chemical profile of a template PG 1159 model ($M_\star = 0.589\,M_\odot$, $T_{\rm eff} = 139\,000$ K) in terms of the outer fractional mass. The locations of the O/C and O/C/He chemical interfaces are indicated with gray regions.

evolution of model star sequences with initial masses on the zeor-age main sequence (ZAMS) in the range $1-3.75\,M_\odot$ and assuming a metallicity of $Z = 0.02$. All of the post-AGB evolutionary sequences computed with the LPCODE evolutionary code (Althaus et al. 2005) were followed through the very late thermal pulse (VLTP) and the resulting born-again episode that give rise to the H-deficient, He-, C-, and O-rich composition characteristic of PG 1159 stars. The masses of the resulting remnants are 0.530, 0.542, 0.565, 0.589, 0.609, 0.664, and 0.741 $M_\odot$. In Fig. 1 the evolutionary tracks employed in this work are shown in the $\log T_{\rm eff}$ versus $\log g$ plane. For details about the input physics and evolutionary code and the numerical simulations performed to obtain the PG 1159 evolutionary sequences employed here, we refer to Althaus et al. (2005) and Miller Bertolami & Althaus (2006, 2007a,b). We briefly describe the chemical structure of our PG 1159 models. In Fig. 24 we show the fractional abundances of the main chemical species, ^{4}He, ^{12}C, and ^{16}O, corresponding to a model with $M_\star = 0.589\,M_\odot$ and $T_{\rm eff} = 139\,000$ K. The chemical transition regions of O/C and O/C/He are clearly visible. The location, thickness, and steepness of these chemical interfaces define the mode-trapping properties of the models. Generally, the mode-trapping features in the pulsation spectrum of these models for periods shorter than about 700 s are induced mostly by the chemical gradient at the O/C/He interface; the O/C chemical transition is much less relevant. For longer periods, however, the core chemical structure in the O/C interface mostly fixes the mode-trapping properties (see, e.g., Córsico & Althaus 2005, 2006, for details).

As mentioned, the star HS 2324 is a hybrid PG 1159 star, that is, it has H on its surface. The presence of H is not expected to substantially modify the evolutionary tracks (Löbling et al. 2019) or the pulsation properties of these stars compared with the standard case of PG 1159 stars, which lack H, because at these evolutionary stages, element diffusion is not operative, and thus vestiges of H left by prior evolution are uniformly distributed throughout the outer layers of the star, instead of forming a pure-H envelope. As a valid approximation, this star was therefore analyzed here using PG 1159 evolutionary models that do not have H in their surfaces.

We computed $\ell = 1, 2$ g-mode adiabatic pulsation periods in the range 80–6000 s with the adiabatic and nonadiabatic versions of the pulsation code LP-PUL (Córsico & Althaus 2006; Córsico et al. 2006) and the same methods we employed in the previous works of La Plata Stellar Evolution and Pulsation Research Group[4]. We analyzed about 4000 PG 1159 models covering a wide range of effective temperatures ($5.4 \gtrsim \log T_{\rm eff} \gtrsim 4.8$), luminosities ($0 \lesssim \log(L_*/L_\odot) \lesssim 4.2$), and stellar masses ($0.530 \leq M_\star/M_\odot \leq 0.741$).

6. Spectroscopic masses

On the basis of the evolutionary tracks presented in Fig. 1 and the published values of the spectroscopic surface gravity and temperature, we derived by interpolation a value of the spectroscopic mass of each of the six analyzed stars. In the case of RX J2117 we obtain a stellar mass of $M_\star = 0.716 \pm 0.150\,M_\odot$. For HS 2324, we obtain a stellar mass of $M_\star = 0.532 \pm 0.150\,M_\odot$, while for NGC 6905 and NGC 1501 we derive $M_\star = 0.590 \pm 0.150\,M_\odot$ and $M_\star = 0.565 \pm 0.150\,M_\odot$, respectively. We obtain $M_\star = 0.533 \pm 0.150\,M_\odot$ for NGC 2371. Finally, we derive $M_\star = 0.742 \pm 0.150\,M_\odot$ for K 1–16. The uncertainties in the stellar mass were estimated from the uncertainties in the $T_{\rm eff}$ and $\log g$ values adopting the extreme values of each parameter when interpolating between the evolutionary tracks of Fig. 1.

7. Asteroseismic modeling

The methods we used to extract information of the stellar mass and the internal structure of RX J2117, HS 2324, NGC 2371, NGC 6905, NGC 1501, NGC 2371, and K 1–16 are the same as we employed in our previous works (see Córsico et al. 2007a,b, 2008, 2009a; Kepler et al. 2014; Calcaferro et al. 2016). In brief, a way to derive an estimate of the stellar mass of GW Vir stars is to compare the observed period spacing of a target star ($\Delta\Pi$) with the asymptotic period spacing ($\Delta\Pi_\ell^{\rm a}$) computed with Eq. (1) at the effective temperature of the star (see the pioneer work of Kawaler 1988). Not all pulsation modes of GW Vir stars generally lie in the asymptotic regime, therefore the agreement between $\Delta\Pi$ and $\Delta\Pi_\ell^{\rm a}$ is usually imperfect. The derivation of the stellar mass using the asymptotic period spacing may therefore not be entirely reliable in pulsating PG 1159 stars that pulsate with modes characterized by low and intermediate radial orders, but it gives a good estimate of the stellar mass for stars pulsating with g modes of high radial order (see Althaus et al. 2008). A variation of this approach to infer the stellar mass of GW Vir

[4] http://fcaglp.fcaglp.unlp.edu.ar/evolgroup/

stars is to compare $\Delta\Pi$ with the average of the computed period spacings ($\overline{\Delta\Pi_k}$). The average of the computed period spacings is assessed as $\overline{\Delta\Pi_k} = (N-1)^{-1}\sum_k \Delta\Pi_k$, where the "forward" period spacing ($\Delta\Pi_k$) is defined as $\Delta\Pi_k = \Pi_{k+1} - \Pi_k$ (k being the radial order) and N is the number of computed periods that lie in the range of the observed periods. This method is more reliable for estimating the stellar mass of GW Vir stars than that described above using $\Delta\Pi^{\rm a}_\ell$ because provided that the average of the computed period spacings is evaluated at the appropriate range of periods, the approach is valid for the regimes of short, intermediate, and long periods as well. When the average of the computed period spacings is taken over a range of periods characterized by high k values, then the predictions of the present method become closer to those of the asymptotic period-spacing approach (Althaus et al. 2008). On the other hand, the present method requires of detailed period computations, at variance with the method described above, that do not involve pulsational calculations. Both methods for assessing the stellar mass rely on the spectroscopic effective temperature, and the results are unavoidably affected by its associated uncertainty.

Another asteroseismological tool for distinguishing the internal structure of GW Vir stars is to seek theoretical models that best match the individual pulsation periods of the target star. To measure the goodness of the match between the theoretical pulsation periods ($\Pi_{\ell,k}$) and the observed individual periods ($\Pi^{\rm o}_i$), we followed the same procedure as in our previous works,

$$\chi^2(M_\star, T_{\rm eff}) = \frac{1}{N}\sum_{i=1}^{N} \min[(\Pi_{\ell,k} - \Pi^{\rm o}_i)^2], \quad (3)$$

where N is the number of observed periods. The observed periods are shown in Tables 9–13. In order to find the stellar model that best replicates the observed periods exhibited by each target star, the "asteroseismological" model, we evaluated the function χ^2 for stellar masses $M_\star = 0.530, 0.542, 0.565, 0.589, 0.609, 0.664$, and $0.741\,M_\odot$. For the effective temperature we employed a much finer grid ($\Delta T_{\rm eff} = 10-30$ K). For each target star, the PG 1159 model that shows the lowest value of χ^2 was adopted as the best-fit asteroseismological model. Below we employ the tools described above to extract information of the GW Vir stars considered in this work.

7.1. RX J2117

For this star, we calculated the average of the computed period spacings for $\ell = 1$, $\overline{\Delta\Pi_k}$, in terms of the effective temperature for all the masses considered. The results are shown in Fig. 25, where we depict $\overline{\Delta\Pi_k}$ corresponding to evolutionary stages before the maximum possible effective temperature, $T_{\rm eff\,MAX}$ (that depends on the stellar mass) with dashed red lines, and the phases after that $T_{\rm eff\,MAX}$ (the WD stage itself) with solid black lines. The location of RX J2117 is indicated by a small red circle with error bars and corresponds to the effective temperature of the star according to Rauch & Werner (1997) and the period spacing derived in Sect. 3.1. The star has a period-spacing value between the values of the curves of $0.565\,M_\odot$ and $0.589\,M_\odot$ at the maximum temperature positions. We performed a linear interpolation between the maximum values of effective temperature for each sequence and obtain $M_\star = 0.569 \pm 0.015\,M_\odot$. This mass value agrees well with that inferred by Vauclair et al. (2002), $M_\star = 0.56^{+0.02}_{-0.04}\,M_\odot$, and Córsico et al. (2007a), $M_\star = 0.560^{+0.018}_{-0.013}\,M_\odot$, who also used the period spacing to infer the stellar mass. Finally, we note that our inferred stellar mass value

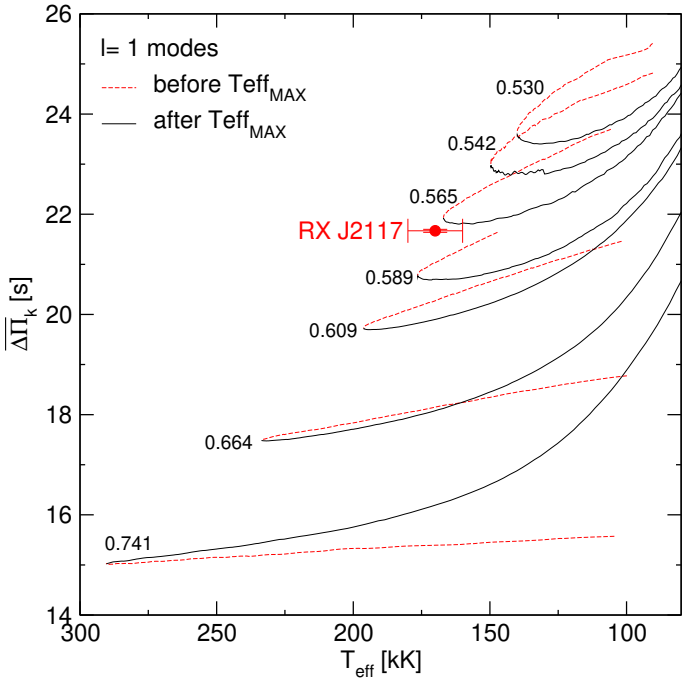

Fig. 25. Dipole ($\ell = 1$) average of the computed period spacings, $\overline{\Delta\Pi_k}$, assessed in a range of periods that includes the periods observed in RX J2117, shown as solid (dashed) curves corresponding to stages before (after) the maximum $T_{\rm eff}$ for different stellar masses. The location of RX J2117 when we use the effective temperature derived by Rauch & Werner (1997), $T_{\rm eff} = 170\,000 \pm 10\,000$ K, and the period spacing $\Delta\Pi = 21.669 \pm 0.030$ s derived in Sect. 4.1 is highlighted with a red circle. We include the error bars associated with the uncertainties in $\overline{\Delta\Pi_k}$ and $T_{\rm eff}$. The stellar mass derived by interpolation is $M_\star = 0.569 \pm 0.015\,M_\odot$.

of $M_\star = 0.569 \pm 0.015\,M_\odot$ strongly disagrees with the spectroscopic mass, $M_\star = 0.716 \pm 0.150\,M_\odot$ (see Sect. 5).

Next, we describe our period-to-period fit procedure. The merit function $\chi^2(M_\star, T_{\rm eff})$ (Eq. (3)) was evaluated for stellar masses $0.530, 0.542, 0.565, 0.589, 0.609, 0.664$, and $0.741\,M_\odot$, and for a very wide interval of the effective temperatures (depending on the stellar mass) with a very small step. In our analysis of period-to-period fits, we only considered the central component ($m = 0$) in the case of multiplets. Following the results obtained in Sect. 4.1, for RX J2117 we assumed that a subset of 21 periods are associated with $\ell = 1$ modes, that is, the 20 periods marked with an asterisk in Table 9 along with the period at ∼1557 s, and left the assignment as $\ell = 1$ or $\ell = 2$ free to the remaining three periods. Specifically, we set the value $\ell = 1$ for all the periods except for those at ∼902 s, ∼1351 s, and 1998 s. On the basis of the analysis made in Sects. 3.1 and 4.1, we consider modes with periods 817.375 s, 824.880 s, 966.785 s, 1031.978 s, 1044.041 s, 1131.200 s, and 1976.060 s as $m \neq 0$ components of rotational multiplets, and thus they were ignored in our period-to-period fits. We display our results in Fig. 26. We find only one minimum compatible with the effective temperature of RX J2117 and its uncertainties, corresponding to a PG 1159 model characterized by $M_\star = 0.565\,M_\odot$ and $T_{\rm eff} = 162\,992$ K (panel c). There are other minima for other stellar masses, but none of them has an effective temperature compatible with the $T_{\rm eff}$ of RX J2117, and they must be discarded.

We adopted the model characterized by $M_\star = 0.565\,M_\odot$, $T_{\rm eff} = 162\,992$ K, and $\log(L_\star/L_\odot) = 3.373$ as the

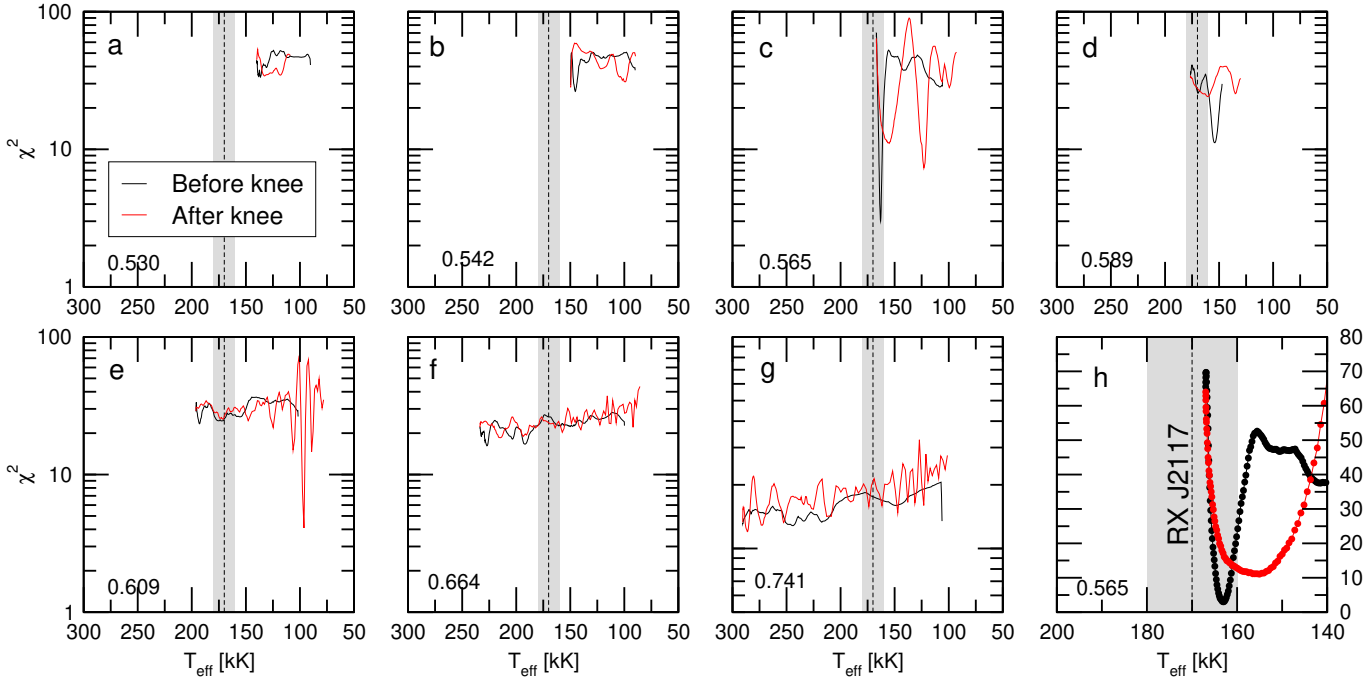

Fig. 26. Quality function of the period fit in terms of the effective temperature for the PG 1159 sequences with different stellar masses (in solar units), indicated at the left bottom corner of each panel. Black (red) lines correspond to stages before (after) the evolutionary knee (see Fig. 1). Only the periods with $m = 0$ (see Table 9) have been considered. The strong minimum in *panel c* corresponds to $M_\star = 0.565\,M_\odot$. *Panel h* is a zoom of the region with the strong minimum seen in *panel c*; the y-axis scale is linear in this case. The vertical dashed line is the spectroscopic $T_{\rm eff}$ of RX J2117 (170 kK), and the gray zone depicts its uncertainties (±10 kK).

asteroseismological model for RX J2117. This model corresponds to an evolutionary stage just before the star reaches its maximum effective temperature ($T_{\rm effMAX} = 167\,000$ K). Our results are almost identical to those obtained by the analysis of Córsico et al. (2007a) (asteroseismological model with $M_\star = 0.565\,M_\odot$ and $T_{\rm eff} = 163\,418$ K), which was based on the same PG 1159 stellar models as in the present analysis, but employing the set of periods measured with ground-based observations of Vauclair et al. (2002) alone. In this way, the incorporation of the new periods detected with TESS to the analysis seems to strengthen the validity of the results of Córsico et al. (2007a). In Table 14 we show a detailed comparison of the observed periods of RX J2117 and the theoretical $m = 0$ periods of the asteroseismological model. According to our asteroseismological model, all the $m = 0$ periods exhibited by RX J2117 correspond to $\ell = 1$ modes with high radial order k, except for two periods that are associated with $\ell = 2$ modes. In order to quantitatively assess the quality of our period fit, we computed the average of the absolute period differences, $\overline{\delta\Pi_i} = \left(\sum_{i=1}^{n} |\delta\Pi_i|\right)/n$, where $\delta\Pi_i = (\Pi_{\ell,k} - \Pi_i^{\rm o})$ and $n = 24$, and the root-mean-square residual, $\sigma = \sqrt{(\sum_{i=1}^{n} |\delta\Pi_i|^2)/n} = \sqrt{\chi^2}$. We obtain $\overline{\delta\Pi_i} = 1.26$ s and $\sigma = 1.73$ s. The quality of our fit for RX J2117 is slightly worst than that achieved by Córsico et al. (2007a) ($\overline{\delta\Pi_i} = 1.08$ s and $\sigma = 1.34$ s). In order to have a global indicator of the goodness of the period fit that takes the number of free parameters, the number of fitted periods, and the proximity between the theoretical and observed periods into account, we computed the Bayes information criterion (BIC; Koen & Laney 2000),

$$\mathrm{BIC} = n_{\rm p}\left(\frac{\log N}{N}\right) + \log\sigma^2, \qquad (4)$$

where $n_{\rm p}$ is the number of free parameters of the models, and N is the number of observed periods. The lower the value of BIC, the better the quality of the fit. In our case, $n_{\rm p} = 2$ (stellar mass and effective temperature), $N = 24$, and $\sigma = 1.73$ s. We obtain BIC = 0.59, which means that our period fit is excellent.

We also include in Table 14 the rates of period change ($\dot\Pi \equiv d\Pi/dt$) predicted for each g mode of RX J2117. All of them are negative ($\dot\Pi < 0$), implying that the periods become shorter over time. The rate of change of periods in WDs and pre-WDs is related to $\dot T$ (T being the temperature at the region of the period formation) and $\dot R_\star$ ($R_\star$ being the stellar radius) through the order-of-magnitude expression $(\dot\Pi/\Pi) \approx -a(\dot T/T) + b(\dot R_\star/R_\star)$ (Winget et al. 1983). According to our asteroseismological model, the star heats and contracts before it reaches its maximum temperature (evolutionary knee) and enters its cooling stage. As a consequence, $\dot T > 0$ and $\dot R_\star < 0$, and then, $\dot\Pi < 0$. As shown in Fig. 11 of Sect. 4.1, RX J2117 exhibits irregular variations of periods on different timescales. A comparison of our theoretical predictions with the observational trends is therefore not possible at this time.

Table 14 also gives information about the pulsational stability or instability nature of the modes associated with the periods fitted to the observed ones (ninth column). In particular, we examine the sign of the computed linear nonadiabatic growth rates (η_k). A positive value of η_k means that the mode is linearly unstable. Interestingly, the interval of periods corresponding to unstable modes of our asteroseismological model is almost coincident with the range of excited periods in RX J2117, except in the case of the shortest periods (692.267 s, 712.975 s, and 733.948 s) and the longest periods (1350.870 s, 1557.010 s, and 1997.760 s) exhibited by the star, which are not predicted to be unstable by our theoretical calculations ($\eta_k < 0$). The reason is that for $T_{\rm eff} = 163\,000$ K, the model sequence of $M_\star = 0.565\,M_\odot$ has unstable $\ell = 1$ ($\ell = 2$) periods in the range 777 s−1181 s (416 s−938 s) (Córsico et al. 2006).

Table 14. Observed and theoretical periods of the asteroseismological model for RX J2117 [$M_\star = 0.565\,M_\odot$, $T_{\rm eff} = 162\,992$ K, $\log(L_\star/L_\odot) = 3.373$].

$\Pi_i^{\rm O}$ (s)	$\ell^{\rm O}$	Π_k (s)	ℓ	k	m	$\delta\Pi_k$ (s)	$\dot{\Pi}_k$ (10^{-11} s/s)	Unstable
692.267	1	689.975	1	30	0	2.292	−2.561	No
712.975	1	712.003	1	31	0	0.972	−4.775	No
733.948	1	732.780	1	32	0	1.168	−5.217	No
757.354	1	754.864	1	33	0	2.490	−6.022	Yes
778.921	1	777.318	1	34	0	1.603	−4.702	Yes
799.495	1	798.832	1	35	0	0.663	−2.655.	Yes
817.375	1	...	1	36	−1	...	...	...
821.105	1	820.614	1	36	0	0.491	−2.508	Yes
824.880	1	...	1	36	+1	...	...	...
843.692	1	843.310	1	37	0	0.382	−5.222	Yes
885.736	1	887.005	1	39	0	−1.269	−7.721	Yes
902.761	?	902.523	2	70	0	0.238	−7.666	Yes
907.489	1	907.453	1	40	0	0.036	−7.849	Yes
951.750	1	953.041	1	42	0	−1.291	−4.485	Yes
966.785	1	...	1	43	−1	...	...	...
972.073	1	974.580	1	43	0	−2.507	−7.938	Yes
994.387	1	994.737	1	44	0	−0.350	−10.487	Yes
1016.467	1	1016.873	1	45	0	−0.406	−10.678	Yes
1031.978	1	...	1	46	−1	...	...	...
1038.120	1	1039.311	1	46	0	−1.191	−11.222	Yes
1044.041	1	...	1	46	+1	...	...	...
1058.026	1	1060.183	1	47	0	−2.157	−8.262	Yes
1103.292	1	1103.398	1	49	0	−0.106	−12.206	Yes
1124.156	1	1125.203	1	50	0	−1.047	−14.094	Yes
1131.200	1	...	1	51	+1	...	...	...
1146.346	1	1146.771	1	51	0	−0.425	−11.240	Yes
1189.956	1	1188.768	1	53	0	1.188	−8.643	Yes
1350.870	?	1345.193	2	105	0	5.677	−9.485	No
1557.010	1	1559.013	1	70	0	−2.003	−13.293	No
1976.060	?	...	1	90	−1	...	...	...
1997.760	?	1998.018	1	90	0	−0.258	−8.917	No

Notes. Periods are in seconds, and rates of period change (theoretical) are in units of 10^{-12} s/s. $\delta\Pi_i = \Pi_i^{\rm O} - \Pi_k$ represents the period differences, ℓ the harmonic degree, k the radial order, and m the azimuthal index. The last column gives information about the pulsational stability or instability nature of the modes.

In Table 15 we list the main characteristics of the asteroseismological model for RX J2117. The seismological stellar mass ($0.565\,M_\odot$) is in excellent agreement with the value derived from the period spacing ($0.569 M_\odot$). The average of the dipole ($\ell = 1$) period spacings of our asteroseismological model is $\overline{\Delta\Pi} = 22.153$ s and the asymptotic period spacing is $\Delta\Pi^{\rm a} = 22.064$ s, in excellent agreement with the $\ell = 1$ mean period spacing derived for RX J2117 in Sect. 4.1 ($\Delta\Pi = 21.669 \pm 0.030$ s). The luminosity of the asteroseismological model, $\log(L_\star/L_\odot) = 3.37$ is lower than the luminosity inferred by Motch et al. (1993), $\log(L_\star/L_\odot) = 3.95$, based on the evolutionary tracks of Wood & Faulkner (1986).

The asteroseismological distance can be computed as in Córsico et al. (2007a). On the basis of the luminosity of the asteroseismological model ($\log(L_\star/L_\odot) = 3.37 \pm 0.04$) and the bolometric correction given by a nonlocal thermal equilibrium (NLTE) model atmosphere with $T_{\rm eff} = 160$ kK and $\log g = 6.6$ computed with the Tübingen Model Atmosphere Package ($BC = -7.954$; see Werner et al. 2003; Córsico et al. 2007a, for details), the absolute magnitude can be assessed as $M_{\rm V} = M_{\rm B} - BC$, where $M_{\rm B} = M_{\rm B,\odot} - 2.5\log(L_\star/L_\odot)$. We employed the solar bolometric magnitude $M_{\rm B\odot} = 4.74$ (Cox 2000). The seismological distance d is derived from the relation $\log d = 15[m_{\rm V} - M_{\rm V} + 5 - A_{\rm V}(d)]$, where we employed the interstellar extinction law of Chen et al. (1998). The interstellar absorption $A_{\rm V}(d)$ is a nonlinear function of the distance and also depends on the Galactic latitude (b). For the equatorial coordinates of RX J2117 (Epoch B2000.00, $\alpha = 21^{\rm h}17^{\rm m}8.^{\rm s}2, \delta = +34^\circ 12' 27''.58$) the corresponding Galactic latitude is $b = -10^\circ 24' 32''.04$. We used the apparent visual magnitude $m_{\rm V} = 13.16 \pm 0.01$ (Motch et al. 1993), and obtained the seismological distance and parallax $d = 480 \pm 20$ pc and $\pi = 2.08 \pm 0.09$ mas, respectively, where the extinction coefficient $A_{\rm V} = 0.47 \pm 0.02$. The uncertainty in the seismological distance comes mainly from the uncertainty in the luminosity of the asteroseismological model, which is admittedly very small ($\Delta\log(L_\star/L_\odot) = 0.04$) because this it is solely attributed to internal errors, that is, uncertainties typical of the period-fit procedure. Realistic estimates of these errors (due to uncertainties in stellar modeling and the pulsation computations) are probably much higher. A very important verification of the validation of the asteroseismological model for RX J2117 is the comparison of the seismological distance with the distance derived from astrometry. We have the estimates from *Gaia*, $d_{\rm G} = 502 \pm 12$ pc and $\pi_{\rm G} = 1.991 \pm 0.05$ mas. They are in excellent agreement

Table 15. Main characteristics of the GW Vir star RX J2117.

Quantity	Spectroscopy astrometry	Asteroseismology (this work)
$T_{\rm eff}$ [kK]	170 ± 10 [(a)]	$163.0^{+2.5}_{-3.7}$
$M_\star$ [$M_\odot$]	0.716 ± 0.15	$0.565^{+0.024}_{-0.023}$
$\log g$ [cm s^{-2}]	$6.0^{+0.3}_{-0.2}$ [(a)]	$6.62^{+0.11}_{-0.07}$
$\log(L_\star/L_\odot)$	3.95 ± 0.5 [(b)]	3.37 ± 0.04
$\log(R_\star/R_\odot)$	...	$-1.21^{+0.046}_{-0.025}$
$M_{\rm env}$ [$M_\odot$]	...	0.02
$(X_{\rm He}, X_{\rm C}, X_{\rm O})_{\rm s}$	0.39, 0.55, 0.06 [(a)]	0.39, 0.32, 0.22
d [pc]	502.186 ± 12.554 [(c)]	480 ± 20
π [mas]	1.991 ± 0.050 [(c)]	2.08 ± 0.09

Notes. The second column corresponds to spectroscopic results, and the third column presents results from the asteroseismological model of this work.
References. [(a)]Werner & Herwig (2006); [(b)]Motch et al. (1993); [(c)]*Gaia*.

with the asteroseismological derivations in view of the uncertainties in both determinations.

We close this section by summarizing our findings for RX J2117. The seismological stellar mass derived from the period spacing is in excellent agreement with the stellar mass of the asteroseismological model, derived through a fit to the individual periods, and in line with what was found by Vauclair et al. (2002) and Córsico et al. (2007a). On the other hand, a seismological mass in the range 0.560–0.569 $M_\odot$ apparently disagrees with the spectroscopic mass, of $0.716 \pm 0.15\,M_\odot$, but nevertheless, they are still compatible each other, given the uncertainties in both determinations, particularly in the spectroscopic mass. On the other hand, the seismological distance derived from the astereoseismological model is in excellent agreement with the distance measured by *Gaia*.

7.2. HS 2324

In Fig. 27 we show $\ell = 1$ $\overline{\Delta\Pi_k}$ as a function of $T_{\rm eff}$ for all the masses considered. These curves are slightly different from those of Fig. 25, which correspond to RX J2117. This is because the averages of the computed period spacings are calculated considering different ranges of periods for different stars. The period spacing of HS 2324 is $\Delta\Pi = 16.407 \pm 0.062$ s, as derived in Sect. 3.2. In this case, we considered two possibilities: that the star is before or after the maximum effective temperature, that is, the "evolutionary knee" (see Fig. 1). This is because we do not know, in principle, the evolutionary stage of the star. We find $M_\star = 0.727 \pm 0.017\,M_\odot$ if the star is before the maximum $T_{\rm eff}$, and $M_\star = 0.758 \pm 0.018\,M_\odot$ if the star is after the maximum $T_{\rm eff}$. These values are much higher than the spectroscopic mass derived in Sect. 5, of $M_\star = 0.532 \pm 0.150\,M_\odot$.

Next, we describe our period-to-period fit analysis for HS 2324. Again, the merit function $\chi^2(M_\star, T_{\rm eff})$ (Eq. (3)) was evaluated for all the stellar masses and effective temperatures covered by our PG 1159 model sequences. We employed the 21 periods of Table 10. We adopted the same approach as for the case of RX J2117, that is, we assumed that there is a subset of 13 periods identified as $\ell = 1$ according to the period spacing derived in Sect. 4.2 (see Table 10), but the remaining 8

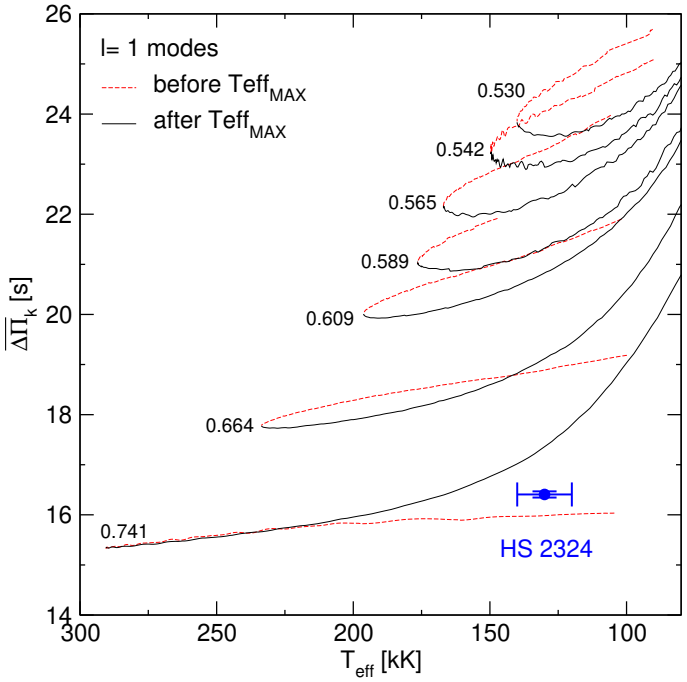

Fig. 27. Dipole ($\ell = 1$) average of the computed period spacings, $\overline{\Delta\Pi_k}$, assessed in a range of periods that includes the periods observed in HS 2324, shown as solid (dashed) curves corresponding to stages before (after) the maximum $T_{\rm eff}$ for different stellar masses. The location of HS 2324 when we use the effective temperature derived by Dreizler et al. (1996), $T_{\rm eff} = 130\,000 \pm 10\,000$ K, and the period spacing $\Delta\Pi = 16.407 \pm 0.062$ s derived in Sect. 3.2 is highlighted with a blue circle. The stellar mass derived from linear interpolation is $M_\star = 0.727 \pm 0.017\,M_\odot$ if the star is before the maximum $T_{\rm eff}$, and by linear extrapolation, it is $M_\star = 0.758 \pm 0.018\,M_\odot$ if the star is after the maximum $T_{\rm eff}$.

periods are allowed to be identified with modes with dipole or quadrupole modes.

Because there is no single global minimum in the quality function when evaluated for all the stellar masses and effective temperatures considered, we were forced to analyze what happens in the range of effective temperatures published for HS 2324, that is $120\,000 \lesssim T_{\rm eff} \lesssim 140\,000$ K. We display our results in Fig. 28. We note a clear minimum for a model with $M_\star = 0.664\,M_\odot$ and $T_{\rm eff} = 138\,572$ K. It is located at the stages previous to the maximum temperature for this mass. We adopted this model as the asteroseismological model for HS 2324. In Table 16 we show a detailed comparison of the observed periods of HS 2324 and the theoretical periods of the asteroseismological model. For this asteroseismological solution, we have $\overline{\delta\Pi_i} = 2.53$ s and $\sigma = 3.36$ s. The quality of our fit for HS 2324 is worse than that achieved for RX J2117 ($\overline{\delta\Pi_i} = 1.26$ s and $\sigma = 1.73$ s). We also computed the BIC. In this case, $N_{\rm p} = 2$ (stellar mass and effective temperature), $n = 21$, and $\sigma = 3.36$ s. We obtain BIC = 1.18, which means that our fit is not as good as for RX J2117 (BIC = 0.59), but still satisfactory.

According to our seismological model, the values of the rate of period change for the g modes of HS 2324 (Col. 7 of Table 16) are ∼10−100 times greater than for the asteroseismological model of RX J2117 (Table 14). This is because the asteroseismological model of HS 2324 ($M_\star = 0.664\,M_\odot$) is more massive than the asteroseismological model of RX J2117 ($M_\star = 0.565 M_\odot$), and the evolution through the PG 1159 stage proceeds considerably faster for massive stars

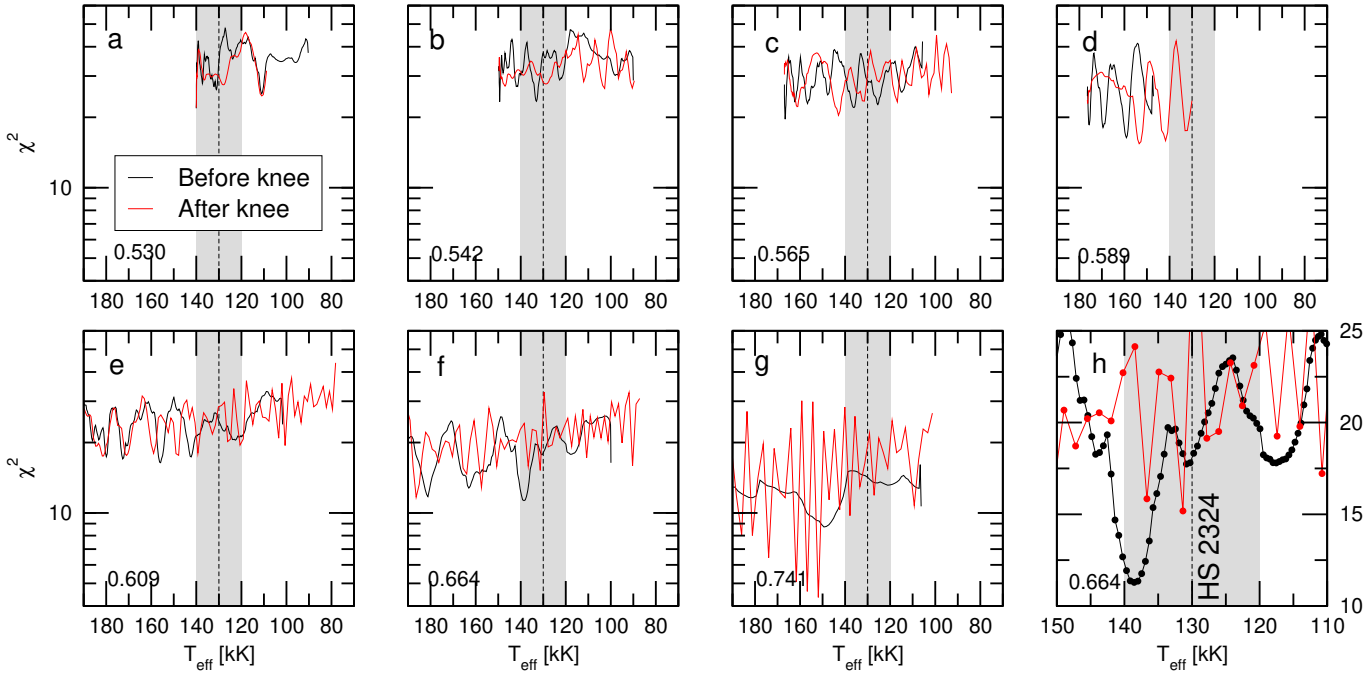

Fig. 28. Same as Fig. 26, but for HS 2324. Note the minimum in *panel f* before the evolutionary knee (black curve), corresponding to $M_\star = 0.664\,M_\odot$. *Panel h* is a zoom of the region with the strong minimum seen in *panel f*; the y-axis scale is linear in this case. The vertical dashed line is the spectroscopic $T_{\rm eff}$ of HS 2324 (130 kK), and the gray zone depicts its quoted uncertainty (±10 kK).

Table 16. Observed and theoretical periods of the asteroseismological model for HS 2324 [$M_\star = 0.664\,M_\odot$, $T_{\rm eff} = 138\,572$ K, $\log(L_\star/L_\odot) = 4.069$].

$\Pi_i^{\rm O}$ (s)	$\ell^{\rm O}$	Π_k (s)	ℓ	k	$\delta\Pi_k$ (s)	$\dot{\Pi}_k$ (10^{-11} s/s)	Unstable
1039.020	?	1038.518	2	101	0.502	−48.352	No
1047.100	1	1051.555	1	59	−4.455	21.631	No
1049.877	?	1048.216	2	102	1.661	−65.542	No
2005.780	?	2006.376	1	113	−0.596	−18.035	Yes
2027.520	?	2024.919	2	197	2.601	−43.713	Yes
2029.350	1	2022.871	1	114	6.479	−8.498	Yes
2047.260	1	2041.419	1	115	5.841	−15.661	Yes
2059.970	1	2060.657	1	116	−0.687	−47.391	Yes
2076.110	?	2078.013	2	202	−1.903	−84.734	Yes
2078.590	1	2078.239	1	117	0.351	−93.688	Yes
2095.046	1	2093.885	1	118	1.161	−132.285	Yes
2098.670	?	2098.804	2	204	−0.134	−73.882	Yes
2110.152	1	2110.330	1	119	−0.178	−137.956	Yes
2160.970	1	2164.402	1	122	−3.432	−19.931	Yes
2170.490	?	2172.624	2	211	−2.134	−88.824	Yes
2175.290	1	2181.536	1	123	−6.246	−20.287	Yes
2193.420	1	2199.885	1	124	−6.465	−52.300	Yes
2202.990	?	2203.977	2	214	−0.987	−55.166	Yes
2553.230	1	2553.519	1	144	−0.289	−128.112	Yes
2568.860	1	2571.257	1	145	−2.397	−78.122	Yes
2682.050	1	2677.444	1	151	4.606	−134.986	Yes

Notes. The columns have the same meaning as in Table 14.

(Miller Bertolami & Althaus 2006). In Sect. 4.2 we called attention to a possible physical change of the period at ∼2193 s from 1999 to 2020, with a negative derivative and a magnitude of $\sim 10^{-9}$ s/s. This value is compatible with the theoretical rate of change for this period, of -0.523×10^{-9} s/s (Table 16).

Column 8 of Table 16 shows that most of the periods of the asteroseismological model that fit the observed periods are predicted to be unstable ($\eta_k > 0$), except for the three periods shorter than ∼2000 s, for which our nonadiabatic computations indicate pulsational stability. For $T_{\rm eff} = 138\,600$ K, the model sequence of $M_\star = 0.664\,M_\odot$ has unstable dipole (quadrupole) periods in the range 2028 s−465 s (1215 s−3095 s) (Córsico et al. 2006). Note that the nonadiabatic pulsation calculations of Córsico et al. (2006) correspond to PG 1159 models

Table 17. Main characteristics of the GW Vir star HS 2324.

Quantity	Spectroscopy astrometry	Asteroseismology (this work)
$T_{\rm eff}$ [kK]	130 ± 10 [(a)]	$138.6^{+3.0}_{-2.8}$
$M_\star$ [$M_\odot$]	0.532 ± 0.150	$0.664^{+0.077}_{-0.055}$
$\log g$ [cm s^{-2}]	6.2 ± 0.2 [(a)]	$5.72^{+0.13}_{-0.10}$
$\log(L_\star/L_\odot)$	...	$4.07^{+0.18}_{-0.21}$
$\log(R_\star/R_\odot)$	...	$-0.73^{+0.06}_{-0.08}$
$M_{\rm env}$ [$M_\odot$]	...	0.02
($X_{\rm H}, X_{\rm He}, X_{\rm C}$,	0.17, 0.35, 0.42,	0.00, 0.47, 0.33,
$X_{\rm O})_{\rm s}$	0.06 [(a)]	0.13
d [pc]	1448.033 ± 105.266 [(b)]	4379^{+1009}_{-940}
π [mas]	0.691 ± 0.0502 [(b)]	$0.228^{+0.063}_{-0.042}$

Notes. The second column corresponds to spectroscopic results, and the third column presents results from the asteroseismological model of this work.
References. [(a)]Werner & Herwig (2006); [(b)]*Gaia* DR2.

without H in the envelopes, which is not strictly the case of a hybrid GW Vir star, which has some H on its surface. However, we do not expect the results of the pulsation analysis to be appreciably modified by the presence of a trace of H.

In Table 17 we list the main characteristics of the asteroseismological model for HS 2324. The stellar mass of the seismological model ($0.664\,M_\odot$) is ~10% smaller than, although still compatible with, the value derived from the period spacing (~$0.73\,M_\odot$), assuming that the star is before the evolutionary knee. This mass discrepancy is reflected in the fact that the dipole ($\ell = 1$) mean period spacing of our asteroseismological model ($\overline{\Delta\Pi} = 18.81$ s) is ~14% longer than the $\ell = 1$ mean period spacing derived for HS 2324 in Sect. 4.2 ($\Delta\Pi = 16.407 \pm 0.062$ s). Given the error ranges of the spectroscopic mass ($0.532 \pm 0.150\,M_\odot$, Sect. 5) and the asteroseismic mass determinations, they are compatible with each other.

We can compute the asteroseismological distance of HS 2324, as we did for RX J2117. We employed the luminosity of the asteroseismological model of HS 2324, $\log(L_\star/L_\odot) = 4.07^{+0.18}_{-0.21}$, a bolometric correction of $BC = -7.24$ (extrapolated from the value corresponding to PG 1159−035 as given by Kawaler & Bradley 1994), and the interstellar extinction law of Chen et al. (1998). For the equatorial coordinates of HS 2324 (Epoch B2000.00, $\alpha = 23^{\rm h}27^{\rm m}15.^{\rm s}95$, $\delta = +40°01'23.''63$) the corresponding Galactic latitude is $b = -20°3'0.''86$. We adopted $m_{\rm V} = 15.41$ (Faedi et al. 2011) and obtained a seismological distance, a parallax, and an extinction coefficient of $d = 4379^{+1009}_{-940}$ pc, $\pi = 0.228^{+0.063}_{-0.042}$ mas, and $A_{\rm V} = 0.398$, respectively. On the other hand, the values measured by *Gaia* are $d_{\rm G} = 1448 \pm 105$ pc and $\pi_{\rm G} = 0.691 \pm 0.050$ mas, in line with the distance inferred by Dreizler et al. (1996) (1500 pc). At variance with the case of RX J2117, there is a serious disagreement between our asteroseismological distance and the distance obtained with *Gaia* for HS 2324. This discrepancy must be largely attributed to the high luminosity of our seismological model. In this sense, the uncertainty of the luminosity of the seismological model ($\Delta\log(L_\star/L_\odot) \sim 0.2$) is just formal and it is probably underestimated because it reflects only internal errors of the period-fit processes. Thus, a compatibility between the seismological distance and the astrometric distance from *Gaia* would be achieved if we were able to employ a more realistic estimate of the uncertainties in the luminosity of the asteroseismological model.

We end this section by summarizing our results for HS 2324. The stellar mass inferred from the period separation (~$0.73\,M_\odot$) is in line with the mass of the seismological model (~$0.66\,M_\odot$), and still compatible with the spectroscopic mass, of $0.532 \pm 0.15\,M_\odot$, given the large uncertainties in the parameters with which the spectroscopic mass is determined, in particular the $\log g$ value.

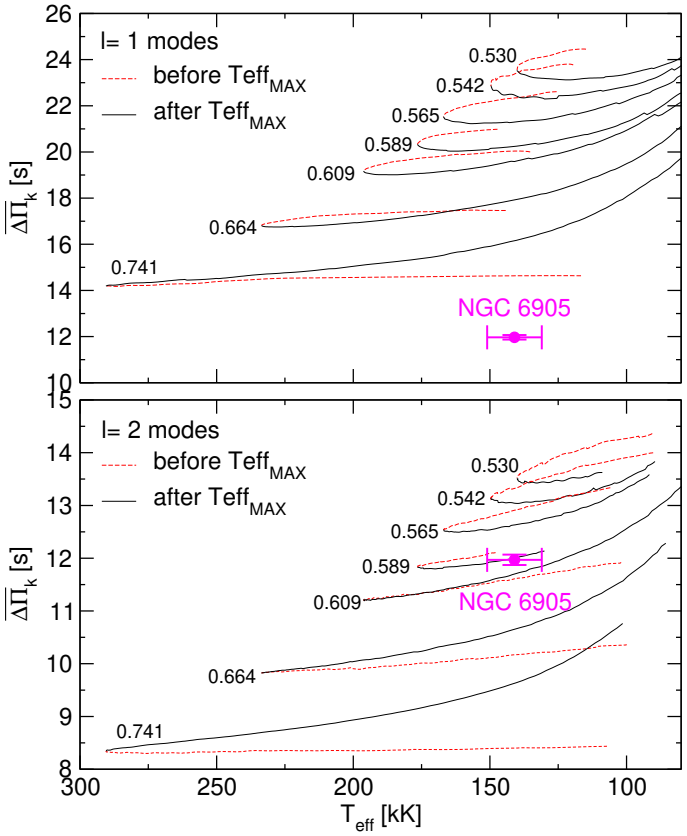

Fig. 29. *Upper panel*: dipole ($\ell = 1$) average of the computed period spacings, $\overline{\Delta\Pi_k}$, assessed in a range of periods that includes the periods observed in NGC 6905, shown as solid (dashed) curves corresponding to stages before (after) the maximum $T_{\rm eff}$ for different stellar masses. The location of NGC 6905 when we use the effective temperature derived by Ciardullo & Bond (1996), $T_{\rm eff} = 141\,000 \pm 10\,000$ K, and the period spacing $\Delta\Pi = 11.9693 \pm 0.0988$ s derived in Sect. 3.3 and assumed to be associated with $\ell = 1$ modes, is highlighted with a magenta circle. The stellar mass derived from linear extrapolation is $M_\star \sim 0.818\,M_\odot$ if the star is before the maximum $T_{\rm eff}$, and it is $M_\star \sim 0.861\,M_\odot$ if the star is after the maximum $T_{\rm eff}$. *Lower panel*: same as in upper panel, but for the case in which the period spacing is assumed to be associated with $\ell = 2$ modes ($\Delta\Pi = 11.9693 \pm 0.0988$ s). In this case, the stellar mass is $M_\star = 0.596 \pm 0.09\,M_\odot$ and $M_\star = 0.590 \pm 0.007\,M_\odot$ if the star is before or after the evolutionary knee, respectively.

7.3. NGC 6905

In the upper panel of Fig. 29 we display the run of the dipole $\overline{\Delta\Pi_k}$ in terms of $T_{\rm eff}$ for all the masses considered for the case of NGC 6905. We assumed the period spacing $\Delta\Pi = 11.9693 \pm 0.0988$ s to be associated with $\ell = 1$ modes. This period spacing results from considering the periods of modes detected with TESS, in addition to the periods from Ciardullo & Bond (1996) (Table 11 of Sect. 4.3). As in the case of HS 2324, for NGC 6905

we considered two possibilities: the star is before or after the evolutionary knee. We find $M_\star \sim 0.818$ if the star is before the maximum $T_{\rm eff}$, and $M_\star \sim 0.811 M_\odot$ if the star is after the maximum $T_{\rm eff}$. These values are obtained by extrapolation because the period spacing of the star, being only about 12 s, is well below the average of the computed spacing curves of our models, even the most massive one ($M_\star = 0.741\,M_\odot$). Therefore, our stellar mass values are just estimates. The stellar mass of NGC 6905 according to these estimates is much higher than the spectroscopic mass of this star, of $M_\star = 0.590 \pm 0.150\,M_\odot$, as derived in Sect. 5.

We also explored the possible situation in which the period spacing of $\Delta\Pi = 11.9693 \pm 0.0988$ s correspond to $\ell = 2$ modes. We then compared this period spacing with the quadrupole $\overline{\Delta\Pi_k}$ in terms of $T_{\rm eff}$ for all the masses considered, as shown in the lower panel of Fig. 29. In this case, the mass value is $M_\star = 0.596 \pm 0.09\,M_\odot$ and $M_\star = 0.590 \pm 0.007\,M_\odot$ if the star is before or after the evolutionary knee, respectively. These values are in excellent agreement with the spectroscopic mass value ($M_\star = 0.59 M_\odot$).

We attempted a period-to-period fit for NGC 6905 using the individual periods of Table 11. We adopted the same approach as for the case of RX J2117 and HS 2324, that is, we assumed that there is a subset of periods identified as $\ell = 1$ according to the period spacing derived in Sect. 4.3 (see Table 11), but the remaining periods are allowed to be associated with dipole or quadrupole modes as well. There are two possibilities with respect to the period ~816 s. Although unlikely, one possibility would be to consider that it is a component $\ell = 1$, $m = \pm 1$ of a rotational triplet, in which case we can ignore this period in our period-fit process and there are 10 observed periods available. The other possibility would be to consider it as a $\ell = 2$, $m = 0$ mode and therefore incorporate it into the analysis. In this case, the period-to-period fit is carried out on a set of 11 periods. The results of our procedure with 10 and with 11 periods are very similar and do not indicate a very clear asteroseismological model regarding the uniqueness of the solutions. Specifically, there are several possible solutions in terms of period match within the effective-temperature range of interest (131 000−151 000 K) for NGC 6905. However, most of the possible solutions (minima in the quality function) correspond to stages after the evolutionary knee. When we accept that NGC 6905 is evolving toward the blue before it reaches its maximum effective temperature, as indicated by its position in the $\log T_{\rm eff} - \log g$ diagram, see Fig. 1, then we do not find any clear minima in the quality function. This makes it virtually impossible to isolate a clear and unambiguous seismological solution. We might still pick out a possible seismological solution consisting of a pre-WD model with a stellar mass $M_\star = 0.664\,M_\odot$ and an effective temperature $T_{\rm eff} = 145\,400$ K. However, the match between the theoretical and observed periods is very poor, with differences of up to ~10 s, which is reflected by the high value of the local minimum in the quality function for that model ($\chi^2 = 16.05\,{\rm s}^2$). Thus, for NGC 6905 we are unable to find an asteroseismological model. The harmonic degree of the mode with period ~816 s remains undetermined, although according to our calculations, the period fits slightly improve when we consider that this corresponds to $\ell = 2$.

We also considered the possibility that the period spacing derived in Sect. 4.3 corresponds to modes $\ell = 2$. In this case, in Table 11 the modes identified as $\ell = 1$ are now identified as $\ell = 2$. In total, we have seven quadrupole modes and four modes that can be alternatively dipole or quadrupole. We assume that the mode with period ~816 s can correspond to a $\ell = 1$ mode or a $\ell = 2$ mode as well. We repeated the period-fit procedure with this identification of modes, but unfortunately did not find a satisfactory seismological solution. In particular, it is very difficult to fit the observed periods at 816.3 s, 851.4 s, 874.8 s, 884 s with $\ell = 1$ or $\ell = 2$ theoretical periods when we assume that the remaining observed periods correspond to $\ell = 2$ modes.

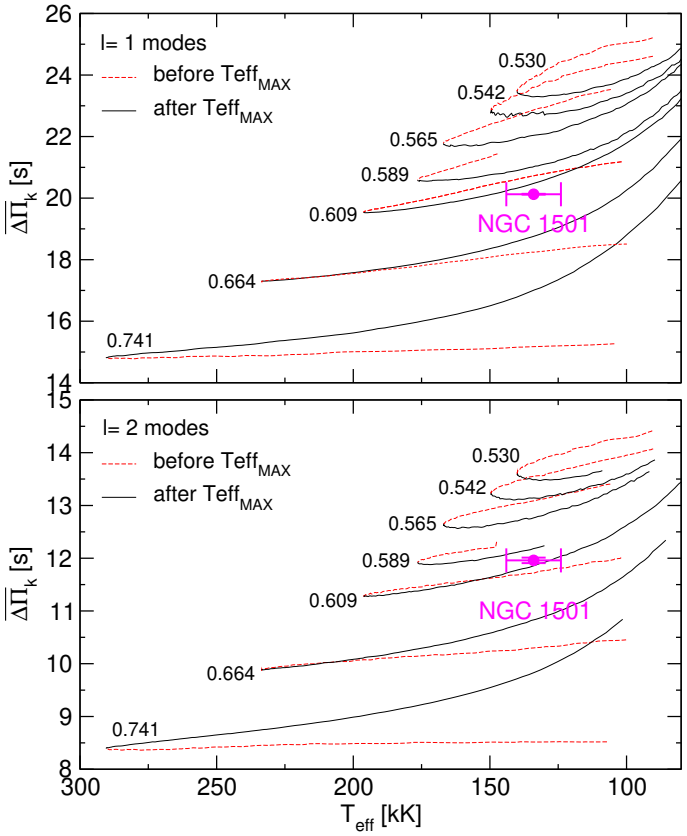

Fig. 30. *Upper panel*: dipole ($\ell = 1$) average of the computed period spacings, $\overline{\Delta\Pi_k}$, assessed in a range of periods that includes the periods observed in NGC 1501, shown as solid (dashed) curves corresponding to stages before (after) the maximum $T_{\rm eff}$ for different stellar masses. The location of NGC 1501 when we use the effective temperature derived by Werner & Herwig (2006), $T_{\rm eff} = 134\,000 \pm 10\,000$ K, and the dipole period spacing, $\Delta\Pi_{\ell=1} = 20.1262 \pm 0.0123$ s (derived in Sect. 3.4), is highlighted with a magenta circle. The stellar mass derived from linear interpolation is $M_\star = 0.621 \pm 0.015\,M_\odot$ if the star is before the maximum $T_{\rm eff}$, and it is $M_\star = 0.624 \pm 0.015\,M_\odot$ if the star is after the maximum $T_{\rm eff}$. *Lower panel*: same as upper panel, but for the case of $\ell = 2$ modes ($\Delta\Pi_{\ell=2} = 11.9593 \pm 0.0520$ s). In this case, the stellar mass is $M_\star = 0.601 \pm 0.015\,M_\odot$ and $M_\star = 0.606 \pm 0.015\,M_\odot$, according to whether the star is before or after the maximum $T_{\rm eff}$.

7.4. NGC 1501

We calculated the $\ell = 1$ and $\ell = 2$ averages of the computed period spacings for the case of NGC 1501. The curves of $\overline{\Delta\Pi_k}$ in terms of $T_{\rm eff}$ for all the masses considered are shown in the upper ($\ell = 1$) and lower ($\ell = 2$) panels of Fig. 30. According to the analysis of Sect. 4.4, the dipole period spacing of NGC 1501 is $\Delta\Pi_{\ell=1} = 20.1262 \pm 0.0123$ s, and the quadrupole period spacing is $\Delta\Pi_{\ell=2} = 11.9593 \pm 0.0520$ s. As in the case of HS 2324 and NGC 6905, for NGC 1501 we considered the two possibilities that the object is before or after the evolutionary knee. From the $\ell = 1$ periods, we find $M_\star = 0.621 \pm 0.015\,M_\odot$ if the star is

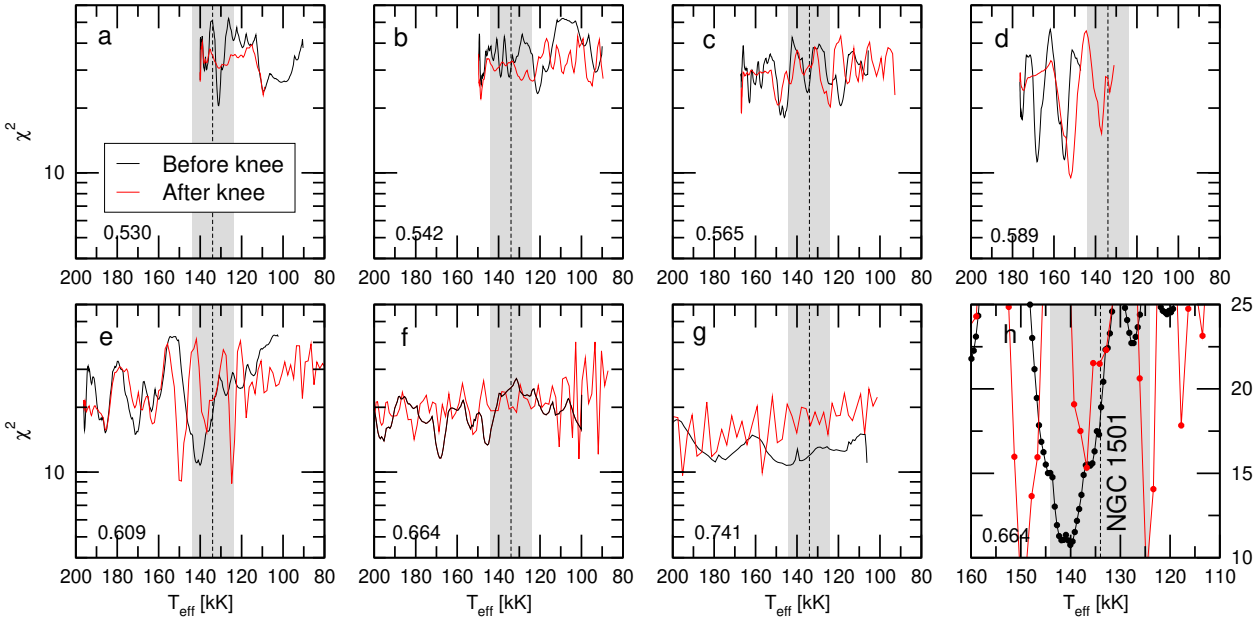

Fig. 31. Same as Fig. 26, but for NGC 1501. The minimum in *panel e* before the evolutionary knee (black curve) corresponds to $M_\star = 0.609\,M_\odot$. *Panel h* is a zoom of the region with the strong minimum seen in *panel e*; the y-axis scale is linear in this case. The vertical dashed line is the spectroscopic $T_{\rm eff}$ of NGC 1501 (134 kK), and the gray zone depicts its uncertainties (±10 kK).

Table 18. Observed and theoretical periods of the asteroseismological model for NGC 1501 [$M_\star = 0.609\,M_\odot$, $T_{\rm eff} = 140\,051$ K, and $\log(L_\star/L_\odot) = 3.853$].

$\Pi_i^{\rm O}$ (s)	$\ell^{\rm O}$	Π_k (s)	ℓ	k	$\delta\Pi_k$ (s)	$\dot{\Pi}_k$ (10^{-11} s/s)	Unstable
1154.360	2	1154.379	2	98	−0.019	−15.441	Yes
1168.900	1	1167.137	1	57	1.713	−10.788	No
1251.910	1	1248.916	1	61	2.994	−21.429	No
1254.632	2	1257.656	2	107	−3.024	−15.823	Yes
1309.086	2	1304.233	2	111	4.853	−42.157	Yes
1310.696	1	1307.716	1	64	2.980	−26.766	No
1321.095	2	1315.744	2	112	5.351	−47.478	Yes
1345.872	2	1350.158	2	115	−4.286	−22.660	Yes
1349.460	1	1348.889	1	66	0.571	−16.437	No
1356.680	2	1362.511	2	116	−5.831	−18.491	Yes
1366.279	1	1367.932	1	67	−1.653	−15.860	No
1372.940	2	1375.144	2	117	−2.204	−18.814	Yes
1381.295	2	1386.419	2	118	−5.124	−22.368	Yes
1392.240	1	1388.738	1	68	3.502	−14.155	No
1431.530	1	1431.050	1	70	0.480	−13.742	No
1512.660	1	1511.332	1	74	1.328	−35.180	No
1760.730	2	1759.810	2	150	0.920	−47.015	Yes
1768.510	1	1772.096	1	87	−3.586	−25.077	No
1777.290	2	1771.373	2	151	5.917	−41.060	Yes
1892.950	1	1895.295	1	93	−2.345	−55.804	Yes
1951.490	1	1953.783	1	96	−2.293	−38.265	Yes
2032.640	1	2035.792	1	100	−3.152	−40.133	Yes
2077.000	1	2075.030	1	102	1.970	−64.074	Yes
5234.810	1	5236.174	1	255	−1.364	−156.804	No

Notes. The columns have the same meaning as in Table 14.

before the evolutionary knee, and $M_\star = 0.624 \pm 0.015 M_\odot$ if the star is after the evolutionary knee. On the other hand, from the $\ell = 2$ periods we derive $M_\star = 0.601 \pm 0.015\,M_\odot$ and $M_\star = 0.606 \pm 0.015\,M_\odot$ depending on the star being before or after the evolutionary knee. These mass values of NGC 1501, which are in the range ∼0.60–0.62 $M_\odot$, are ∼5–10% higher than but still compatible with the spectroscopic mass of this star ($M_\star = 0.565 \pm 0.150\,M_\odot$; see Sect. 5).

As for the other target stars analyzed in this study, we performed a period-to-period fit for NGC 1501. We employed

Table 19. Main characteristics of the GW Vir star NGC 1501.

Quantity	Spectroscopy astrometry	Asteroseismology (this work)
$T_{\rm eff}$ [kK]	134 ± 10 [(a)]	140 ± 6.5
$M_\star$ [$M_\odot$]	0.565 ± 0.150	$0.609^{+0.055}_{-0.020}$
$\log g$ [cm s^{-2}]	6.0 ± 0.2 [(a)]	$5.90^{+0.14}_{-0.11}$
$\log(L_\star/L_\odot)$	3.70 [(b)]	3.85 ± 0.02
$\log(R_\star/R_\odot)$	...	-0.84 ± 0.05
$M_{\rm env}$ [$M_\odot$]	...	0.01
$(X_{\rm H}, X_{\rm He}, X_{\rm C})_{\rm s}$	0.50, 0.35, 0.15 [(a)]	0.50, 0.35, 0.10
d [pc]	1762.801 ± 78.566 [(c)]	824 ± 15
π [mas]	0.567 ± 0.025 [(c)]	$1.22^{+0.02}_{-0.03}$

Notes. The second column corresponds to spectroscopic results, and the third column presents results from the asteroseismological model of this work.
References. [(a)]Koesterke & Hamann (1997), Werner & Herwig (2006); [(b)]Ercolano et al. (2004); [(c)]*Gaia*.

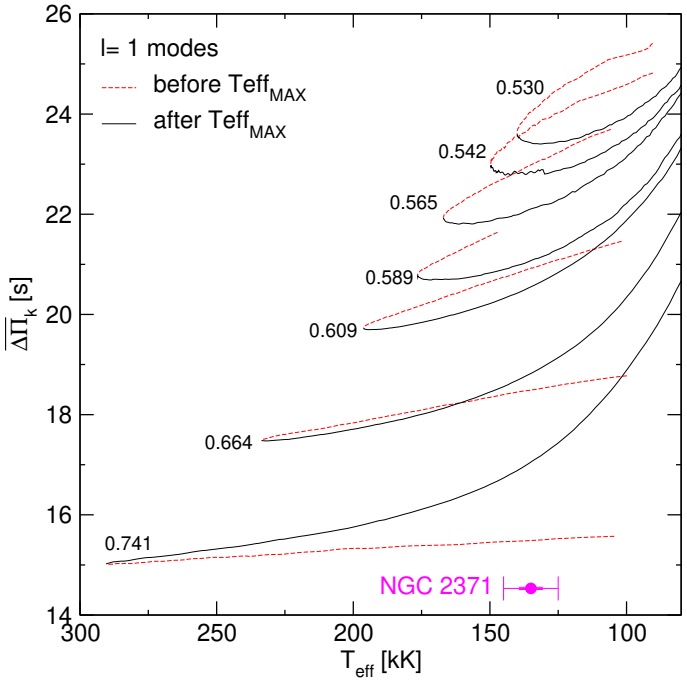

Fig. 32. Dipole ($\ell = 1$) average of the computed period spacings, $\overline{\Delta\Pi_k}$, assessed in a range of periods that includes the periods observed in NGC 2371, shown as solid (dashed) curves corresponding to stages before (after) the maximum $T_{\rm eff}$ for different stellar masses. The location of NGC 2371 when we use the effective temperature derived by Ciardullo & Bond (1996), $T_{\rm eff} = 135\,000 \pm 10\,000$ K, and the period spacing $\Delta\Pi = 14.5312 \pm 0.0226$ s derived in Sect. 3.5, is highlighted with a magenta circle. The stellar mass derived from linear extrapolation is $M_\star \sim 0.760\,M_\odot$ if the star is before the maximum $T_{\rm eff}$, and it is $M_\star \sim 0.856\,M_\odot$ if the star is after the maximum $T_{\rm eff}$.

the periods of Table 12, except for the periods 1318.46 s and 1999.16 s, which do not fit the $\ell = 1$ nor the $\ell = 2$ series of periods with constant period spacings. We assumed that there is a subset of 14 periods corresponding to $\ell = 1$ modes, and 10 periods identified with $\ell = 2$ modes, according to the period spacings derived in Sect. 4.4 (see Table 12). We display our results for this analysis in Fig. 31. We note the existence of a clear minimum for the model with $M_\star = 0.609 M_\odot$ and $T_{\rm eff} = 140\,051$ K. It is located at the stages before the maximum temperature for this mass. The value of the quality function for this solution is $\chi^2 = 10.76\,{\rm s}^2$. We adopt this model as the asteroseismological model for NGC 1501. In Table 18 we show a detailed comparison of the observed periods of NGC 1501 and the theoretical periods of the asteroseismological model. For this asteroseismological solution, we have $\overline{\delta\Pi_i} = 2.81$ s and $\sigma = 3.28$ s. The quality of our fit for NGC 1501 is worse than that achieved for RX J2117 ($\overline{\delta\Pi_i} = 1.26$ s and $\sigma = 1.73$ s), but comparable to that obtained for HS 2324 ($\overline{\delta\Pi_i} = 2.53$ s and $\sigma = 3.36$ s). We also computed the BIC. In this case, $N_{\rm p} = 2$ (stellar mass and effective temperature), $n = 24$, and $\sigma = 3.28$ s. We obtain BIC = 1.15, which means that our fit is not as good as for RX J2117 (BIC = 0.59), but very similar to that of HS 2324 (BIC = 1.18), and still satisfactory. We repeated the analysis by fixing the harmonic degree of the 14 periods labeled $\ell = 1$ at the outset, but allowing the other 10 periods to be associated with $\ell = 1$ or $\ell = 2$ modes. We also repeated the above analysis by incorporating the two periods excluded into the period fit (1318.46 s and 1999.16 s), allowing them to be associated with $\ell = 1$ or $\ell = 2$ modes. In both realizations, we obtained the same asteroseismological solution as before ($M_\star = 0.609\,M_\odot$ and $T_{\rm eff} = 140\,051$ K), and with similar values of the quality function. The fact that we arrive at the same seismological solution for NGC 1501 implies that the period-fit process automatically assigns the observed periods that we had originally assumed to be associated with quadrupole modes (following the strong constraint imposed by the period spacing; see Table 12) to theoretical modes with $\ell = 2$. This adds robustness to the identification of the harmonic degree of modes made in Sect. 4.4.

The secular rates of period change for NGC 1501, as predicted by our seismological model, are shown in Col. 7 of Table 18. All the values are negative, reflecting the fact that the star would evolve toward high temperatures and would rapidly contract, which shortens the periods of g modes with time. The rates of period change are in the range $(10-160) \times 10^{-11}$ s/s, being similar to those of the asteroseismological model of HS 2324 (Table 16), and two orders of magnitude higher than those of the asteroseismological model of RX J2117 (Table 14).

We include in Col. 8 of Table 18 the information about the stability or instability of the modes of the asteroseismological model. Strikingly, all quadrupole modes are predicted to be unstable ($\eta_k > 0$), while most dipole modes are predicted to be stable ($\eta_k < 0$). This is because the model sequence of $M_\star = 0.609\,M_\odot$ has unstable dipole (quadrupole) periods in the range 1817 s–4228 s (1077 s–3041 s) (Córsico et al. 2006). Unlike the previous targets, the stability calculations of the modes with $\ell = 1$ therefore do not favor the validity of the seismological model for NGC 1501. However, we mention that stability properties of the g modes in these stars strongly depend on the envelope composition (Quirion et al. 2007), which is affected by the treatment of convective boundary mixing during the born-again episode. Thus, with a readjustment of the abundances of O, C, and He we do not rule out that an agreement could be found between the observed $\ell = 1$ periods and the range of unstable $\ell = 1$ periods of our models, thus alleviating this discrepancy. However, a fine-tuning of the surface chemical composition of our models to fit the range of observed periods is beyond the scope of this paper. This kind of nonadiabatic asteroseismology of GW Vir stars has been attempted by Quirion et al. (2009).

We show the main characteristics of the asteroseismological model for NGC 1501 in Table 19. The stellar mass of the

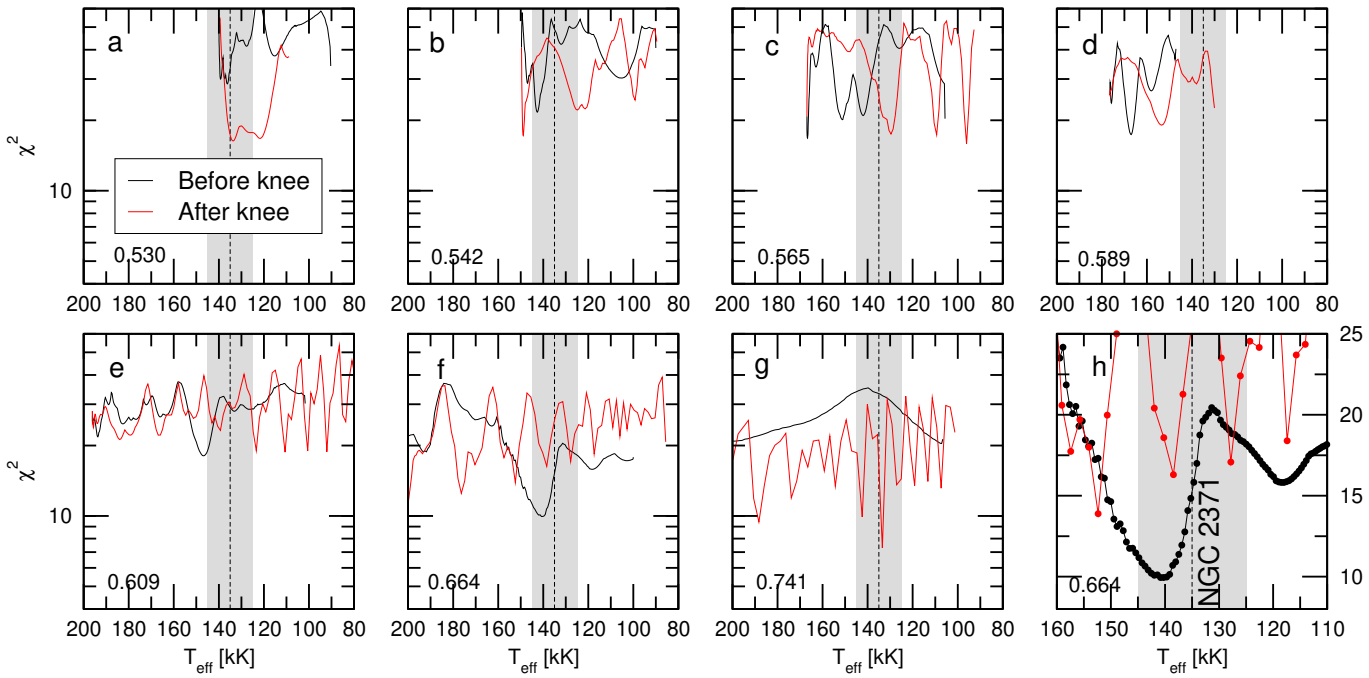

Fig. 33. Same as Fig. 26, but for NGC 2371. The minimum in *panel f* before the evolutionary knee (black curve) corresponds to $M_\star = 0.664\,M_\odot$. *Panel h* is a zoom of the region with the strong minimum seen in *panel f*; the y-axis scale is linear in this case. The vertical dashed line is the spectroscopic $T_{\rm eff}$ of NGC 2371 (135 kK), and the gray zone depicts its uncertainties (±10 kK).

Table 20. Observed and theoretical periods of the asteroseismological model for NGC 2371 [$M_\star = 0.664\,M_\odot$, $T_{\rm eff} = 140\,265$ K, and $\log(L_\star/L_\odot) = 4.066$].

$\Pi_i^{\rm O}$ (s)	$\ell^{\rm O}$	Π_k (s)	ℓ	k	$\delta\Pi_k$ (s)	$\dot{\Pi}_k$ (10^{-11} s/s)	Unstable
878.523	1	875.320	1	49	3.203	1.981	No
895.111	1	893.367	1	50	1.744	6.166	No
925.465	1	929.693	1	52	−4.228	−5.008	No
968.474	1	964.815	1	54	3.659	−47.723	No
982.800	1	980.871	1	55	1.929	−52.214	No
988.200	?	986.704	2	96	1.496	−1.264	No
998.000	1	997.767	1	56	0.233	−52.153	No
1005.600	?	1007.777	2	98	−2.177	−10.730	No
1010.000	1	1015.513	1	57	−5.513	−19.545	No
1825.000	1	1828.713	1	103	−3.713	−37.306	No

Notes. The columns have the same meaning as in Table 14.

seismological model ($0.609\,M_\odot$) is in excellent agreement with the mass derived from the period spacing (∼0.60–0.62 $M_\odot$), assuming that the star is before the evolutionary knee. This agreement in stellar mass is reflected in the fact that dipole and quadrupole mean period spacings of our asteroseismological model, $\overline{\Delta\Pi}_{\ell=1} = 20.610$ s and $\overline{\Delta\Pi}_{\ell=2} = 11.683$ s, are in excellent agreement with the $\ell = 1$ and $\ell = 2$ mean period spacings derived for NGC 1501 in Sect. 4.4, $\Delta\Pi_{\ell=1} = 20.1262 \pm 0.0123$ s and $\Delta\Pi_{\ell=2} = 11.9593 \pm 0.0520$ s, respectively. Both the stellar mass of the seismological model and the mass value derived from the period spacings are somewhat higher than the spectroscopic mass, $0.565 \pm 0.150\,M_\odot$ (Sect. 5). The luminosity of the asteroseismological model, $\log(L_\star/L_\odot) = 3.85$, is somewhat higher than that derived by Ercolano et al. (2004) [$\log(L_\star/L_\odot) = 3.70$] in order to provide an ionizing spectrum that could reproduce the ionization structure implied by the observed nebular spectrum.

We derived the asteroseismological distance for NGC 1501 as we did for RX J2117 and HS 2324. We employed the luminosity of the asteroseismological model of NGC 1501, $\log(L_\star/L_\odot) = 3.85 \pm 0.02$, a bolometric correction of $BC = -7.46$ (extrapolated from the value corresponding to PG 1159−035 as given by Kawaler & Bradley 1994), and the interstellar extinction law of Chen et al. (1998). For the equatorial coordinates of NGC 1501 (epoch B2000.00, $\alpha = 4^{\rm h}6^{\rm m}59.^{\rm s}40, \delta = +60°55'14.''20$) the corresponding Galactic latitude is $b = 6°33'4.''06$. When we adopt $m_{\rm V} = 13.0$ (Montreal White Dwarf Database; Dufour et al. 2017), we obtain a seismological distance, a parallax, and an extinction coefficient of $d = 824 \pm 15$ pc, $\pi = 1.22^{+0.02}_{-0.03}$ mas, and $A_{\rm V} = 0.85$. On the other hand, the values from *Gaia* are $d_{\rm G} = 1763 \pm 79$ pc and $\pi_{\rm G} = 0.567 \pm 0.025$ mas. The seismological distance is ∼50% shorter than that measured by *Gaia*. The origin of this discrepancy may reside in the uncertainties related to our seismological model. Again, as in the case

of HS 2314, a better estimate of the uncertainties of the luminosity of the asteroseismological model might contribute to bringing the asteroseismological distance and parallax values closer to those derived by *Gaia*.

We bring this section to a close by summarizing our results for NGC 1501. The stellar mass inferred from the period separations (∼0.60−62 $M_\odot$) is in line with the mass of the seismological model (∼0.61 $M_\odot$). These values are somewhat higher than but still in agreement with the spectroscopic mass of ∼0.57 $M_\odot$.

7.5. NGC 2371

In Fig. 32 we display the curves of $\overline{\Delta\Pi_k}$ as function of $T_{\rm eff}$ for all the masses considered. The period spacing of NGC 2371 is $\Delta\Pi = 14.5312 \pm 0.0226$, as derived in the analysis of Sect. 4.5. As in the case of HS 2324, NGC 6905, and NGC 1501, for NGC 2371 we considered the possibility that the object is before or after the evolutionary knee. We find $M_\star = 0.760\,M_\odot$ if the star is before the evolutionary knee, and $M_\star = 0.856\,M_\odot$ if the star is after the evolutionary knee. As in the case of NGC 6905, these values are assessed by extrapolation because the period spacing of the star, being only about 14.5 s, is well below the average of the $\ell = 1$ computed period-spacing curves of our models, even the most massive one. Therefore our stellar mass values are just estimates. These estimates for the stellar mass of NGC 2371 are much larger (∼60%) than the spectroscopic mass of this star, of $M_\star = 0.533 \pm 0.150\,M_\odot$ (Sect. 5).

Below we describe our period-to-period fit analysis for NGC 2371. Again, the merit function $\chi^2(M_\star, T_{\rm eff})$ (Eq. (3)) was evaluated for all the stellar masses and effective temperatures covered by our PG 1159 model sequences. We employed the ten periods of Table 13. We adopted the same approach as for the case of the previous target stars, that is, we assumed that there is a subset of eight periods identified as $\ell = 1$ according to the period spacing derived in Sect. 4.5 (see Table 13), but the remaining two periods are allowed to be identified with modes with $\ell = 1$ or $\ell = 2$ modes.

As in the previous cases, given the absence of a single global minimum in the quality function, we focused on the range of effective temperatures compatible with NGC 2371, that is, $125\,000 \lesssim T_{\rm eff} \lesssim 135\,000$ K. We display our results in Fig. 33. A clear minimum exists for a model with $M_\star = 0.664\,M_\odot$ and $T_{\rm eff} = 140\,265$ K. It is located at the stages before the maximum temperature for this mass. We adopt this model as the asteroseismological model for NGC 2371. In Table 20 we show a detailed comparison of the observed periods of NGC 2371 and the theoretical periods of the asteroseismological model. For this asteroseismological solution, we have $\overline{\delta\Pi_i} = 2.79$ s and $\sigma = 3.15$ s. The quality of our fit for NGC 2371 is poorer than that achieved for RX J2117 ($\overline{\delta\Pi_i} = 1.26$ s and $\sigma = 1.73$ s), although it is comparable to those of HS 2324 ($\overline{\delta\Pi_i} = 2.53$ s and $\sigma = 3.36$ s) and NGC 1501 ($\overline{\delta\Pi_i} = 2.81$ s and $\sigma = 3.28$ s). We also computed the BIC. In this case, $N_{\rm p} = 2$ (stellar mass and effective temperature), $n = 10$, and $\sigma = 3.15$ s. We obtain BIC = 1.20, which means that our fit is not as good as for RX J2117 (BIC = 0.59), although it is comparable with those of HS 2324 (BIC = 1.18) and NGC 1501 (BIC = 1.15).

Most of the period change rates for NGC 2371 (Col. 7 of Table 20) are negative, in concordance with the fact that the asteroseismological model for this star evolves toward higher effective temperatures and contracts. The magnitudes of $\dot{\Pi}$ are on average comparable to those of HS 2324 and NGC 1501. Regarding the pulsational stability or instability nature of the modes with periods that fit the periods observed in NGC 2371 (Col. 9 of Table 20), the nonadiabatic calculations predict that all the periods (dipole and quadrupole) are stable because at $T_{\rm eff} = 138\,600$ K, the model sequence of $M_\star = 0.664\,M_\odot$ has unstable $\ell = 1$ ($\ell = 2$) periods in the range 1962 s−4480 s (1190 s−3045 s) (Córsico et al. 2006). Then, our nonadiabatic pulsation results contradict the observational evidence, similar to the case of NGC 1501. Again, we mention that the intervals of unstable periods are highly dependent on the chemical composition of the outer part of the PG 1159 stars, which is affected by uncertainties in the treatment of convective boundary mixing during the born-again episode.

Table 21. Main characteristics of the GW Vir star NGC 2371.

Quantity	Spectroscopy astrometry	Asteroseismology (this work)
$T_{\rm eff}$ [kK]	135 ± 10 [(a)]	$140.3^{+10.6}_{-5.3}$
$M_\star$ [$M_\odot$]	0.533 ± 0.150	$0.664^{+0.077}_{-0.055}$
$\log g$ [cm s^{-2}]	6.3 ± 0.2 [(a)]	$5.74^{+0.19}_{-0.12}$
$\log(L_\star/L_\odot)$	3.45 [(b)]	$4.07^{+0.01}_{-0.02}$
$\log(R_\star/R_\odot)$	−0.98 [(b)]	$-0.74^{+0.04}_{-0.07}$
$M_{\rm env}$ [$M_\odot$]	...	0.02
$(X_{\rm He}, X_{\rm C}, X_{\rm O})_{\rm s}$	0.54, 0.37, 0.08 [(a)]	0.47, 0.33, 0.13
d [pc]	1879.138 ± 232.467 [(c)]	1816^{+11}_{-51}
π [mas]	0.532 ± 0.066 [(c)]	$0.554^{+0.013}_{-0.007}$

Notes. The second column corresponds to spectroscopic results, and the third column presents results from the asteroseismological model of this work.
References. [(a)]Herald & Bianchi (2004); [(b)]Gómez-González et al. (2020); [(c)]*Gaia*.

In Table 21 we list the main characteristics of the asteroseismological model for NGC 2371. The luminosity and radius of the asteroseismological model ($\log(L_\star/L_\odot) = 4.07$, $\log(R_\star/R_\odot) = -0.74$) are substantially larger than the values derived by Gómez-González et al. (2020) ($\log(L_\star/L_\odot) = 3.45$, $\log(R_\star/R_\odot) = -0.98$) from stellar atmosphere models. The stellar mass of the seismological model (0.664 $M_\odot$) is ∼14% lower than the mass inferred from the period spacing (∼0.76 $M_\odot$), assuming that the star is before the evolutionary knee. This mass discrepancy is reflected in the fact that the dipole ($\ell = 1$) mean period spacing of our asteroseismological model ($\overline{\Delta\Pi} = 18.45$ s) is markedly longer than the $\ell = 1$ mean period spacing for NGC 2371 derived in Sect. 4.5 ($\Delta\Pi = 14.5312 \pm 0.0226$ s). Both the stellar mass of the seismological model and the value derived from the period spacing disagree with the spectroscopic mass, $0.533 \pm 0.150\,M_\odot$ (Sect. 5). This discrepancy between the spectroscopic mass (based on measured $T_{\rm eff}$ and $\log g$ values) and seismological masses (based on period spacing and individual periods compared to theoretical expectations) is similar to that found for HS 2324.

We employed the luminosity of the asteroseismological model of NGC 2371, $\log(L_\star/L_\odot) = 4.066^{+0.01}_{-0.02}$, a bolometric correction of $BC = -7.24$ (the same value as we used to assess the distance to HS 2314) and the interstellar extinction law of Chen et al. (1998) to estimate the asteroseismological distance. For the equatorial coordinates of NGC 2371 (Epoch B2000.00, $\alpha = 7^{\rm h}25^{\rm m}34\overset{\rm s}{.}69$, $\delta = +29°29'26\overset{''}{.}32$) the corresponding Galactic latitude is $b = 19°50'35\overset{''}{.}52$. By adopting an apparent magnitude of $m_{\rm V} = 13.50$ (Montreal White Dwarf Database; Dufour et al. 2017), we derive $d = 1816^{+11}_{-51}$ pc, $\pi = 0.554^{+0.013}_{-0.007}$ mas, and

$A_V = 0.402$. On the other hand, the values from *Gaia* are $d_G = 1879 \pm 232$ pc and $\pi_G = 0.532 \pm 0.066$ mas. The seismological distance and parallax and their counterparts measured by *Gaia* agree well, given the uncertainties in both sets of magnitudes.

We end this section with a summary of our results for NGC 2371. The stellar mass inferred from the period separation is higher than the mass of the seismological model, but they still agree. However, these values are at variance with the spectroscopic mass, which is markedly lower. The seismological distance, on the other hand, is in good concordance with that measured by *Gaia*. This suggests that the parameters of the seismological model are correct, and that the discrepancy in mass between the seismological inference and the spectroscopic derivation can come from very uncertain values in the spectroscopic $T_{\rm eff}$ and $\log g$.

8. Summary and conclusions

We have performed a detailed asteroseismological analysis of the known GW Vir stars RX J2117, HS 2324, NGC 6905, NGC 1501, NGC 2371, and K 1−16 on the basis of the new TESS observations of these stars. The primary mission of TESS is to search for exoplanets around bright targets, although the high-precision photometry capabilities of the mission also allow us to study low-amplitude stellar variability, including WD pulsations (Bell et al. 2019; Bognár et al. 2020). We studied the pulsation spectrum of these stars, and in one case (RX J2117), we estimated the rotation period on the basis of frequency-splitting multiplets. We also determined their stellar mass and other structural and evolutionary properties on the basis of the detailed PG 1159 evolutionary models of Althaus et al. (2005) and Miller Bertolami & Althaus (2006). We considered adiabatic and nonadiabatic g-mode pulsation periods on PG 1159 evolutionary models with stellar masses ranging from 0.530 to 0.741 $M_\odot$. These models take the complete evolution of progenitor stars through the thermally pulsing AGB phase and born-again episode into account.

We estimated a mean period spacing for five of the six studied stars. To do this, we considered an augmented period spectrum for each star, combining the periods detected in previous works with ground-based observations with the more precise periods detected with TESS. In this way, we expanded the number of observed periods when possible, which allowed us to arrive at a regime where asteroseismological methods start to be robust. The benefit of deriving an underlying period spacing in the observed period spectrum of GW Vir stars is twofold. On the one hand, it allows placing strong constraints on the stellar mass. On the other hand, it allows assigning the harmonic degree ℓ to a large number of observed periods, which simplifies and constrains the subsequent process of fitting the individual periods and the derivation of asteroseismological models. For five of the objects studied, we constrained the stellar mass by comparing the observed period spacing with the average of the computed period spacings. We considered the cases where the star is before or after the maximum possible effective temperature, although the $\log g$ and $T_{\rm eff}$ spectroscopic values and their comparison with evolutionary tracks of PG 1159 stars strongly suggests that all the target stars are evolving before the evolutionary knee in the $T_{\rm eff} - \log g$ diagram (Fig. 1). When possible, we also employed the individual observed periods to search for a representative seismological model for each star. Finally, we derived seismological distances whenever this was possible, and compared these estimates with the robust astrometric distances measured by *Gaia*. We present the main results for each analyzed star below.

RX J2117. We found 15 secure periods with the TESS observations for this star (see Table 3). From two complete rotational triplets and three triplets with one lacking component in the TESS frequency spectrum of this star, we derived a rotation period of $P_{\rm rot} \sim 1.04$ days, in agreement with previous works (Vauclair et al. 2002; Córsico et al. 2007a). On the basis of a subset of 20 periods of the extended period spectrum (ground-based plus TESS observations; Table 9), we inferred an $\ell = 1$ constant period spacing of $\Delta\Pi = 21.669 \pm 0.030$ s. This allowed a safe identification of 27 periods as dipole modes, with the remainder 4 periods without a secure assignation of the value of ℓ. The comparison of this period spacing with the average of the theoretical period spacings allowed us to derive a stellar mass of $M_\star = 0.569 \pm 0.015\ M_\odot$, in perfect agreement with the estimates from Vauclair et al. (2002) ($M_\star = 0.56\ M_\odot$), and Córsico et al. (2007a) ($M_\star = 0.560\ M_\odot$) also using the period spacing to derive the stellar mass. We next derived an asteroseismological model for this star by means of a period-to-period fit procedure. The magnitude of the rates of period change for the asteroseismological model ranges from $\sim 2.5 \times 10^{-11}$ to $\sim 14.1 \times 10^{-11}$ s/s and all the values are negative, in concordance with the fact that the model fast evolves toward high effective temperatures ($\dot{T}_{\rm eff} > 0$) and contracts ($\dot{R}_\star < 0$), a little before the maximum possible temperature is reached. Most of the g modes of the asteroseismological model are predicted to be linearly unstable, in concordance with the observations. Two of the periods that could not be identified with $\ell = 1$ modes using the constant period spacing are identified with $\ell = 2$ modes and the remaining two periods with $\ell = 1$ modes, according to the asteroseismological model (Table 14). The stellar mass of the asteroseismological model ($M_\star = 0.565 \pm 0.024\ M_\odot$) is in excellent agreement with the mass derived from the period spacing. Finally, we derived a seismological distance ($d = 480$ pc) in complete consensus with the *Gaia* distance ($d_G = 502$ pc), giving robustness to the asteroseismological model. On the other hand, the asteroseismological masses apparently disagree with the spectroscopic mass ($M_\star = 0.716\ M_\odot$), but given the large uncertainties of this last estimate, we conclude that the asteroseismological and spectroscopic determinations agree with each other.

HS 2324. We detected 12 periods from the TESS data for this star (Table 4). At variance with Silvotti et al. (1999), we found no rotational multiplets with a much better frequency resolution of 0.35 μHz. This prevented us from deriving a rotational period. Using a subset of 9 periods of the augmented period spectrum (ground-based and TESS data; see Table 10), we inferred an $\ell = 1$ constant period spacing of $\Delta\Pi = 16.407 \pm 0.062$ s, which enabled a robust identification of 13 periods as $\ell = 1$ modes. The periods from ground-based observations we used in this paper are slightly different from those in Table 2 of Silvotti et al. (1999). By comparing the derived dipole period spacing with the average of the theoretical period spacings, we estimated a stellar mass of $M_\star = 0.727 \pm 0.017\ M_\odot$ if the star is before the evolutionary knee. We obtained an asteroseismological model for HS 2324 by comparing the individual observed and theoretical periods. Most of the rates of period change for the asteroseismological model are negative, and their magnitudes are in the interval $(\sim 8.5 - 138.0) \times 10^{-11}$ s/s, which implies that this star must evolve much faster than RX J2117. Our stability analysis predicts most of the modes of the asteroseismological model to be unstable, in line with observations. Most of the observed periods that could not be identified with $\ell = 1$

modes on the basis of the constant period spacing are identified with modes $\ell = 2$ according to the asteroseismological model (Table 16). The stellar mass of the asteroseismological model, $M_\star = 0.664^{+0.077}_{-0.055}\,M_\odot$, is ∼10% lower than the mass estimated from the period spacing, but still compatible with it. Finally, the seismological distance ($d = 4379 \pm 1000$ pc) is three times larger than the *Gaia* distance ($d_G = 1448$ pc), but if we were to take realistic uncertainties that affect seismological distance into account, probably the disagreement would probably be not as great. The asteroseismological masses, on the other hand, are higher than the spectroscopic mass ($M_\star = 0.532\,M_\odot$). However, because of the large uncertainties in the spectroscopic mass, both spectroscopic and asteroseismological determinations are compatible with each other. Additional future observations of HS 2324 will be of great importance in detecting new periods and investigating possible signals of stellar rotation through frequency multiples.

NGC 6905. TESS photometry indicates only four periods in the pulsation spectrum of this star, as shown in Table 5. We employed a subset of seven periods of the enlarged list of periods (see Table 11) to uncover a constant period spacing of $\Delta\Pi = 11.9693 \pm 0.0988$ s, which we can in principle attribute to $\ell = 1$ modes. This period spacing enabled us to securely identify seven periods as dipole modes. By comparing the inferred $\ell = 1$ period spacing with the average of the theoretical period spacings, we obtained a stellar mass estimate of $M_\star \sim 0.818\,M_\odot$ if the star is before the maximum $T_{\rm eff}$. This estimate of the stellar mass strongly disagrees with the spectroscopic mass of this star, $M_\star = 0.590\,M_\odot$. We also explored the possible situation in which the period spacing of $\Delta\Pi = 11.9693 \pm 0.0988$ s corresponds to $\ell = 2$ modes. In this case, the mass of the star would be $M_\star = 0.596 \pm 0.009\,M_\odot$ and $M_\star = 0.590 \pm 0.007\,M_\odot$ if the star is before or after the evolutionary knee, respectively, in very good agreement with the spectroscopic mass value. On the other hand, the results of our period-to-period fit procedure do not indicate a clear and unique asteroseismological solution, regardless of whether the period spacing corresponds to $\ell = 1$ or $\ell = 2$. We are therefore unable to find an asteroseismological model for NGC 6905, which deprives us of the possibility of estimating the seismic distance for this star.

NGC 1501. We measured 16 periods for this star on the basis of TESS observations (Table 6). We considered a subset of 23 periods of the enlarged list of periods (i.e., from ground-based plus TESS observations; see Table 12), and we found a $\ell = 1$ constant period spacing of $\Delta\Pi = 20.1262 \pm 0.0123$ s and a $\ell = 2$ constant period spacing of $\Delta\Pi = 11.9593 \pm 0.0520$ s. This enabled us to identify 14 periods as $\ell = 1$ modes and 10 periods as $\ell = 2$ modes, with the remaining 2 periods without a secure assignation of the ℓ value. The comparison of these observed period spacings with the average of the theoretical period spacings for $\ell = 1$ and $\ell = 2$ allowed us to infer a stellar mass of $M_\star = 0.621 \pm 0.015\,M_\odot$ and $M_\star = 0.601 \pm 0.015\,M_\odot$, respectively, if the star is before the maximum $T_{\rm eff}$. These values are in close agreement each other. We derived an asteroseismological model for this star on the basis of our usual period-to-period fit procedure (Table 14). The magnitude of the rates of period change for the asteroseismological model ranges from $\sim 10 \times 10^{-11}$ to $\sim 160 \times 10^{-11}$ s/s and all the values are negative, as expected on the grounds that the model heats up and contracts quickly. Noticeably, all the $\ell = 2$ modes are predicted to be unstable by our nonadiabatic calculations, while most $\ell = 1$ modes are predicted to be stable. The stellar mass of the asteroseismological model ($M_\star = 0.609^{+0.06}_{-0.02}\,M_\odot$) is in perfect concordance with the mass inferred from the period separations, and in agreement with the spectroscopic mass, given its uncertainty. Finally, we derived a seismological distance ($d = 824$ pc) which is ∼50% shorter than the *Gaia* distance ($d_G = 1763$ pc). The agreement between these sets of values could improve if we could employ more realistic values for the uncertainties in the luminosity of the asteroseismological model.

NGC 2371. We detected five periods from the TESS data for this star (Table 7). Considering a subset of eight periods of the enlarged period set (i.e., those from ground-based observations along with TESS data; see Table 13), we found a $\ell = 1$ constant period spacing of $\Delta\Pi = 14.5312 \pm 0.0226$ s, allowing us to safely identify eight periods with $\ell = 1$ modes, leaving the remaining two periods unidentified. The comparison of the derived dipole period spacing with the average of the model period spacings results in an estimate of the stellar mass of $M_\star \sim 0.760\,M_\odot$ if the star is before the evolutionary knee. We obtained an asteroseismological model for NGC 2371 from a period-to-period fit, with most of the rates of period change being negative, and with magnitudes in the range $(\sim 2-52) \times 10^{-11}$ s/s. Our stability analysis predicts all of the modes of the asteroseismological model to be stable, which contradicts observations. The two observed periods that could not be identified with $\ell = 1$ modes on the basis of the constant period spacing are identified with $\ell = 2$ modes according to the asteroseismological model (Table 20). The stellar mass of the asteroseismological model, $M_\star = 0.664^{+0.077}_{-0.055}\,M_\odot$, is ∼14% lower than the mass inferred from the period spacing, assuming that the star is before the evolutionary knee. The asteroseismological distance is $d = 1816$ pc, in very good agreement with the distance measured with *Gaia*, of $d_G = 1880 \pm 232$ pc. This agreement reinforces the validity of the asteroseismological model. Both the stellar mass of the seismological model and the mass value derived from the period spacing are in disagreement with the spectroscopic mass, of $M_\star = 0.533 \pm 0.150\,M_\odot$. This mass discrepancy is probably due to the large uncertainty in the spectroscopic $\log g$ value. We conclude that in a similar way as for RX J2117 and HS 2324, these spectroscopic parameters need to be redetermined for NGC 2371.

K 1–16. For this star, we were able to detect only five (or six) periods (Table 8). The amplitudes and frequencies change significantly in such a way that when we consider the sectors of TESS individually, some modes have zero amplitudes, but have finite amplitudes in other sectors. Due to the complexity and changing nature of the period spectrum of this star, along with the high noise level of its power spectrum, we were forced to crudely estimate the period values, and then added a single period detected from the ground. Considering a composite list of periods, we only have six periods available, in which we found no evidence of any pattern of constant period spacing. Due to all these reasons, our asteroseismological analysis was limited, but it revealed the dramatic changes that the pulsations experience in this star, as depicted in Fig. 7.

The results of this paper demonstrate that the high-quality observations of TESS, considered in conjunction with ground-based observations (which are usually more uncertain), are able to provide very important input to the asteroseismology of GW Vir stars, in line with recent reports for other classes of pulsating WDs, such as the case of a DBV star (Bell et al. 2019), pre-ELMV stars (Wang et al. 2020), warm DA WDs (Althaus et al. 2020), and DAV stars (Bognár et al. 2020). The TESS space mission demonstrates that it can greatly contribute to the asteroseismology of WDs and pre-WDs, becoming a

worthy successor of the *Kepler* mission, which has had an excellent performance at studying pulsating WDs (Córsico 2020). The TESS mission, in conjunction with other ongoing space missions such as Cheops (Moya et al. 2018) and future space missions such as PLATO (Piotto 2018), along with new surveys and telescopes such as the Legacy Survey for Space and Time (LSST Science Collaboration 2009), which will be operational in the coming years (Fantin et al. 2020), will probably make much progress in WD asteroseismolgy.

Acknowledgements. We wish to acknowledge the suggestions and comments of an anonymous referee that strongly improved the original version of this work. This paper includes data collected with the TESS mission, obtained from the MAST data archive at the Space Telescope Science Institute (STScI). Funding for the TESS mission is provided by the NASA Explorer Program. STScI is operated by the Association of Universities for Research in Astronomy, Inc., under NASA con-tract NAS 5–26555. Part of this work was supported by AGENCIA through the Programa de Modernización Tecnológica BID 1728/OC-AR, and by the PIP 112-200801-00940 Grant from CONICET. M. U. acknowledges financial support from CONICYT Doctorado Nacional in the form of grant number No: 21190886. SOK is supported by CNPq-Brazil, CAPES-Brazil and FAPERGS-Brazil. KJB is supported by the National Science Foundation under Award No. AST-1903828. This research has made use of NASA's Astrophysics Data System. Financial support from the National Science Centre under projects No. UMO-2017/26/E/ST9/00703 and UMO-2017/25/B/ST9/02218 is appreciated.

References

Althaus, L. G., Serenelli, A. M., Panei, J. A., et al. 2005, A&A, 435, 631
Althaus, L. G., Córsico, A. H., Kepler, S. O., & Miller Bertolami, M. M. 2008, A&A, 478, 175
Althaus, L. G., Córsico, A. H., Isern, J., & García-Berro, E. 2010, A&ARv, 18, 471
Althaus, L. G., Córsico, A. H., Uzundag, M., et al. 2020, A&A, 633, A20
Baran, A. S., Telting, J. H., Németh, P., Bachulski, S., & Krzesiński, J. 2015, A&A, 573, A52
Bell, K. J. 2017, PhD Thesis, University of Texas, USA
Bell, K. J., Hermes, J. J., Vanderbosch, Z., et al. 2017, ApJ, 851, 24
Bell, K. J., Córsico, A. H., Bischoff-Kim, A., et al. 2019, A&A, 632, A42
Blöcker, T. 2001, Ap&SS, 275, 1
Bognar, Z., & Sodor, A. 2016, IBVS, 6184
Bognár, Z., Kawaler, S. D., Bell, K. J., et al. 2020, A&A, 638, A82
Bond, H. E., Kawaler, S. D., Ciardullo, R., et al. 1996, AJ, 112, 2699
Borucki, W. J., Koch, D., Basri, G., et al. 2010, Science, 327, 977
Bradley, P. A., Winget, D. E., & Wood, M. A. 1993, ApJ, 406, 661
Brassard, P., Fontaine, G., Wesemael, F., & Hansen, C. J. 1992, ApJS, 80, 369
Calcaferro, L. M., Córsico, A. H., & Althaus, L. G. 2016, A&A, 589, A40
Chang, H. K., Shih, I. C., Liu, C. Y., et al. 2013, A&A, 558, A63
Chen, B., Vergely, J. L., Valette, B., & Carraro, G. 1998, A&A, 336, 137
Ciardullo, R., & Bond, H. E. 1996, AJ, 111, 2332
Córsico, A. H. 2020, Front. Astron. Space Sci., 7, 47
Córsico, A. H., & Althaus, L. G. 2005, A&A, 439, L31
Córsico, A. H., & Althaus, L. G. 2006, A&A, 454, 863
Córsico, A. H., Althaus, L. G., Benvenuto, O. G., & Serenelli, A. M. 2002, A&A, 387, 531
Córsico, A. H., Althaus, L. G., & Miller Bertolami, M. M. 2006, A&A, 458, 259
Córsico, A. H., Althaus, L. G., Miller Bertolami, M. M., & Werner, K. 2007a, A&A, 461, 1095
Córsico, A. H., Miller Bertolami, M. M., Althaus, L. G., Vauclair, G., & Werner, K. 2007b, A&A, 475, 619
Córsico, A. H., Althaus, L. G., Kepler, S. O., Costa, J. E. S., & Miller Bertolami, M. M. 2008, A&A, 478, 869
Córsico, A. H., Althaus, L. G., Miller Bertolami, M. M., & García-Berro, E. 2009a, A&A, 499, 257
Córsico, A. H., Althaus, L. G., Miller Bertolami, M. M., González Pérez, J. M., & Kepler, S. O. 2009b, ApJ, 701, 1008
Córsico, A. H., Althaus, L. G., Miller Bertolami, M. M., & Kepler, S. O. 2019, A&ARv, 27, 7
Costa, J. E. S., Kepler, S. O., Winget, D. E., et al. 2008, A&A, 477, 627
Cox, A. N. 2000, Allen's Astrophysical Quantities (New York: AIP Press)
Dreizler, S., Werner, K., Heber, U., & Engels, D. 1996, A&A, 309, 820
Dufour, P., Blouin, S., Coutu, S., et al. 2017, ASP Conf. Ser., 509, 3
Dziembowski, W. 1977, Acta Astron., 27, 203
Eastman, J., Siverd, R., & Gaudi, B. S. 2010, PASP, 122, 935
Ercolano, B., Wesson, R., Zhang, Y., et al. 2004, MNRAS, 354, 558
Faedi, F., West, R. G., Burleigh, M. R., Goad, M. R., & Hebb, L. 2011, MNRAS, 410, 899
Fantin, N. J., Côté, P., & McConnachie, A. W. 2020, ApJ, 900, 139
Feibelman, W. A., Kaler, J. B., Bond, H. E., & Grauer, A. D. 1995, PASP, 107, 914
Fontaine, G., & Brassard, P. 2008, PASP, 120, 1043
Gautschy, A., Althaus, L. G., & Saio, H. 2005, A&A, 438, 1013
Gómez-González, V. M. A., Toalá, J. A., Guerrero, M. A., et al. 2020, MNRAS, 496, 959
Grauer, A. D., & Bond, H. E. 1984, ApJ, 277, 211
Handler, G., Kanaan, A., & Montgomery, M. H. 1997a, A&A, 326, 692
Handler, G., Pikall, H., O'Donoghue, D., et al. 1997b, MNRAS, 286, 303
Herald, J. E., & Bianchi, L. 2004, ApJ, 609, 378
Hermes, J. J., Gänsicke, B. T., Kawaler, S. D., et al. 2017a, ApJS, 232, 23
Hermes, J. J., Kawaler, S. D., Bischoff-Kim, A., et al. 2017b, ApJ, 835, 277
Herwig, F. 2001, ApJ, 554, L71
Howell, S. B., Sobeck, C., Haas, M., et al. 2014, PASP, 126, 398
Jenkins, J. M., Twicken, J. D., McCauliff, S., et al. 2016, Proc SPIE, 9913, 99133E
Kawaler, S. D. 1988, IAU Symp., 123, 329
Kawaler, S. D., & Bradley, P. A. 1994, ApJ, 427, 415
Kepler, S. O. 1993, Baltic Astron., 2, 515
Kepler, S. O., Fraga, L., Winget, D. E., et al. 2014, MNRAS, 442, 2278
Koen, C., & Laney, D. 2000, MNRAS, 311, 636
Koesterke, L. 2001, Ap&SS, 275, 41
Koesterke, L., & Hamann, W. R. 1997, IAU Symp., 180, 114
Ledoux, P., & Walraven, T. 1958, Handbuch der Physik, 51, 353
Löbling, L., Rauch, T., Miller Bertolami, M. M., et al. 2019, MNRAS, 489, 1054
LSST Science Collaboration (Abell, P. A., et al.) 2009, ArXiv e-prints [arXiv:0912.0201]
Miller Bertolami, M. M., & Althaus, L. G. 2006, A&A, 454, 845
Miller Bertolami, M. M., & Althaus, L. G. 2007a, A&A, 470, 675
Miller Bertolami, M. M., & Althaus, L. G. 2007b, MNRAS, 380, 763
Miller Bertolami, M. M., Althaus, L. G., Serenelli, A. M., & Panei, J. A. 2006, A&A, 449, 313
Motch, C., Werner, K., & Pakull, M. W. 1993, A&A, 268, 561
Moya, A., Barceló Forteza, S., Bonfanti, A., et al. 2018, A&A, 620, A203
Murphy, S. J. 2015, MNRAS, 453, 2569
Napiwotzki, R., & Schoenberner, D. 1991, A&A, 249, L16
Nather, R. E., Winget, D. E., Clemens, J. C., Hansen, C. J., & Hine, B. P. 1990, ApJ, 361, 309
O'Donoghue, D. 1994, MNRAS, 270, 222
Østensen, R. H., Bloemen, S., Vučković, M., et al. 2011, ApJ, 736, L39
Piotto, G. 2018, European Planetary Science Congress, EPSC2018-969
Provencal, J. L., Montgomery, M. H., Kanaan, A., et al. 2009, ApJ, 693, 564
Quirion, P. O., Fontaine, G., & Brassard, P. 2007, ApJS, 171, 219
Quirion, P. O., Fontaine, G., & Brassard, P. 2009, J. Phys. Conf. Ser., 172, 012077
Rauch, T., & Werner, K. 1997, in The Third Conference on Faint Blue Stars, eds. A. G. D. Philip, J. Liebert, R. Saffer, & D. S. Hayes, 217
Ricker, G. R., Winn, J. N., Vanderspek, R., et al. 2014, Proc. SPIE, 9143, 914320
Ricker, G. R., Winn, J. N., Vanderspek, R., et al. 2015, J. Astron. Telesc. Instrum. Syst., 1, 014003
Silvotti, R. 1996, A&A, 309, L23
Silvotti, R., Dreizler, S., Handler, G., & Jiang, X. J. 1999, A&A, 342, 745
Stanghellini, L., Cox, A. N., & Starrfield, S. 1991, ApJ, 383, 766
Starrfield, S. G., Cox, A. N., Hodson, S. W., & Pesnell, W. D. 1983, ApJ, 268, L27
Starrfield, S., Cox, A. N., Kidman, R. B., & Pesnell, W. D. 1984, ApJ, 281, 800
Tassoul, M., Fontaine, G., & Winget, D. E. 1990, ApJs, 72, 335
Vauclair, G., Belmonte, J. A., Pfeiffer, B., et al. 1993, A&A, 267, L35
Vauclair, G., Moskalik, P., Pfeiffer, B., et al. 2002, A&A, 381, 122
Wang, K., Zhang, X., & Dai, M. 2020, ApJ, 888, 49
Watson, T. K., & Werner, K. 1992, IAU Circ., 5603, 1
Werner, K., & Herwig, F. 2006, PASP, 118, 183
Werner, K., Deetjen, J. L., Dreizler, S., et al. 2003, ASP Conf. Ser., 288, 31
Werner, K., Rauch, T., & Kruk, J. W. 2007, A&A, 474, 591
Werner, K., Rauch, T., & Kruk, J. W. 2010, ApJ, 719, L32
Winget, D. E., & Kepler, S. O. 2008, ARA&A, 46, 157
Winget, D. E., Hansen, C. J., & van Horn, H. M. 1983, Nature, 303, 781
Winget, D. E., Nather, R. E., Clemens, J. C., et al. 1991, ApJ, 378, 326
Wood, P. R., & Faulkner, D. J. 1986, ApJ, 307, 659
York, D. G., Adelman, J., Anderson, J. E., Jr, et al. 2000, AJ, 120, 1579
Zong, W., Charpinet, S., Fu, J.-N., et al. 2018, ApJ, 853, 98